Summer 2015

Constrained Discrete Phase Control of a Heaving Wave Energy Converter in Irregular Seas Using Reinforcement Learning

Praveen D. Malali
Old Dominion University

CONSTRAINED DISCRETE PHASE CONTROL OF A HEAVING WAVE ENERGY CONVERTER IN IRREGULAR SEAS USING REINFORCEMENT LEARNING

by

Praveen D. Malali
B.E. July 2006, Visvesvaraya Technological University, India
M.S. December 2010, Old Dominion University

A Dissertation Submitted to the Faculty of
Old Dominion University in Partial Fulfillment of the
Requirements for the Degree of

DOCTOR OF PHILOSOPHY

MECHANICAL ENGINEERING

OLD DOMINION UNIVERSITY
August 2015

Approved by:

_____
Miltiadis Kotinis (Director)

_____
Sushil K. Chaturvedi (Member)

_____
Gene Hou (Member)

_____
Jin Wang (Member)

ABSTRACT

CONSTRAINED DISCRETE PHASE CONTROL OF A HEAVING WAVE ENERGY CONVERTER IN IRREGULAR SEAS USING REINFORCEMENT LEARNING

Praveen D. Malali
Old Dominion University, 2015
Director: Miltiadis Kotinis

Designed for offshore deployment in irregular seas, the point absorber wave energy conversion (WEC) system is promisingly attractive amongst the currently available WEC technologies. The effectiveness of phase control when applied to a heaving point absorber through a hydraulic power take-off (PTO) system is systematically investigated in both regular and irregular waves. For this purpose, two phase control accumulators are utilized in the hydraulic PTO system. Simulations are performed in MATLAB® using the Cummins equation to model the dynamics of the heaving point absorber in the time domain.

For a given sea state, the opening instant of the control valves of the phase control accumulators relative to the wave excitation peak and the volumetric displacement of the hydraulic motor are utilized as parameters in a number of simulation runs. In regular waves, the parametric investigation demonstrates that in most cases there is a trade-off between maximizing the mean generated power and minimizing the maximum motion amplitude. In fully developed irregular seas, a parametric investigation of different sea states in the North Atlantic demonstrates that by utilizing phase control a significant increase in the power absorption efficiency can be obtained compared to the WEC system operation without phase control.

The problem of providing an effective phase-control strategy that maximizes the mean generated power of the WEC system subject to motion amplitude constraints is formulated and solved using a Reinforcement Learning (RL) approach based on the Q-learning algorithm. The RL-based controller chooses actions that determine the opening instant of the phase control accumulator

valves and the volumetric displacement of the hydraulic motor. As demonstrated in both regular and irregular waves, the RL-based controller is successful in finding the optimal phase-control strategy. Finally, the prediction of the wave excitation force is performed using a Radial Basis Function (RBF) network ensemble in order to evaluate the impact of the prediction accuracy on the RL-controller's performance. The results show that the computed mean generated power and maximum motion amplitude values using the RBF network ensemble predictions compare very well with the corresponding values computed assuming perfect knowledge of the future wave excitation.

ACKNOWLEDGEMENTS

I wish to express my sincere thanks to Dr. Miltiadis Kotinis for his guidance and support during the entire course of this study. Thanks are also due to Drs. Sushil Chaturvedi, Gene Hou, and Jin Wang for serving as members of my dissertation committee.

I would like to thank my parents, Dattatry and Padma Malali, for making the necessary sacrifices that allowed me to pursue my doctoral studies. Thanks are also due to my beloved wife, Deepthi Malali, for her support and sacrifice during my doctoral studies. I wish to thank Prashanth and Soumya Malali for their support. Also, many thanks to my brother and his wife, Pramod Malali and Chaithra Malali, for their continued support during my study.

I would like to thank Anne Iott and Christina Birdsong for their unwavering encouragement and support throughout my graduate school work.

TABLE OF CONTENTS

Page

LIST OF TABLES

Table Page

Table Page

LIST OF FIGURES

CHAPTER I

INTRODUCTION

1.1 Global Energy Demand and Renewable Energy Resources

According to a recent estimate by Mora et al. [1], planet Earth is home to roughly 8.7 million species. All living organisms need energy in order to survive. The primary source of energy on our planet is the Sun: Earth receives approximately $5.7 \cdot 10^{24}$ Joules of solar energy on an annual basis [2]. Living organisms harness this energy either directly or indirectly, e.g., plants harness energy from the Sun directly during photosynthesis whereas humans acquire energy by consuming plants [3]. Research shows that plants capture about $2 \cdot 10^{23}$ Joules of energy per year from solar radiation (sunlight) for photosynthesis [4]. During photosynthesis, plants use sunlight, water, and carbon dioxide to synthesize sugars and organic compounds [4].

Human beings occupy the apex position in the ecological food chain [5] and, as such, they have devised complex survival techniques like agriculture and animal-rearing. Energy from various entities such as sunlight, firewood, and certain forms of dehydrated biomass are used by humans for comfort, safety, warmth, and heat [6]. This broad range of natural entities that are utilized by humans for survival and comfort are commonly referred to as natural resources of energy.

Human beings rarely live in isolation [7]. Their tendency to congregate gave rise to communal living and settlements. Later, these settlements evolved and developed into rural villages, towns and cities [8]. In 2014, out of a total human population of 7.25 billion people, nearly 3.8 billion people live in urban areas (towns and cities) [9]. According to a recent report released by the United Nations, the urban population is expected to grow and comprise nearly 60 percent of the total human population by 2030 [9]. This development in the pattern of human settlement has led to increased energy consumption. Urban areas such as towns, cities, and mega-cities are responsible for 75 percent of the world's energy consumption [10]. The demand for energy has

fuelled the efforts to find natural resources of energy which can provide cheap and reliable energy for human consumption.

Firewood or wood fuel is one of the oldest natural resource of energy known to humans [11]. Consisting mainly of carbon, the burning of wood releases significant amount of heat and light. With a specific energy of 14.9 MJ/kg [12], firewood has been used to supply energy for cooking, heating in colder climates, and protection against wild animals. Fossil fuels – mainly coal, natural gas, and petroleum - have profoundly impacted human societies since the era of the Industrial Revolution. Coal, which has a specific energy of 30.2 MJ/kg [12], facilitated the beginning of the Industrial Revolution in Western Europe in the early 17th century. Petroleum and its derivatives are currently used as the primary source of energy in transportation, e.g., automobiles, aircraft, ships, and trains. Coal and natural gas are also used for electricity generation in thermal power plants. About 67 % of the total electricity generated in the United States in 2013 was from fossil fuels (coal, natural gas, and petroleum) [13].

In the early 20th century, it was discovered that radioactive isotopes of uranium, plutonium, and thorium, commonly referred to as "nuclear fuels", can be made to undergo controlled nuclear fission [14]. In the process of nuclear fission, a significant amount of energy in the form of heat and radiation is released. Since the early 1960's, nuclear fuels have been used for the purposes of steam generation in electricity generation plants, submarines, and naval aircraft carriers [15]. With a specific energy of $3.9 \cdot 10^6$ MJ/kg (for uranium enriched to 3.5% in light water reactor) [16], nuclear fuels are the densest, usable energy resource. About 19% of the total electricity generated in the United States in 2013 was from nuclear fuels [13].

Although fossil and nuclear fuels are energy-rich, their usage could have detrimental impact on human societies and the earth's ecosystem [17]. The combustion of fossil fuels results in the emission of greenhouse gases such as carbon dioxide, carbon monoxide, and methane [18].

Various studies have shown that increased greenhouse gas emissions eventually lead to the occurrence of the greenhouse effect [19]. This effect causes the earth's surface temperature to increase due to the radiation-absorbing properties of the emitted greenhouse gases. Melting of the polar ice caps followed by a sea-level rise has also been attributed to increased greenhouse gas emissions [19].

Even though nuclear fuels have higher energy densities than fossil fuels, the nuclear-reactor related accidents at Three Mile Island [20], Chernobyl [21], and Fukushima Daiichi [22] have demonstrated the disastrous effects that the release of highly radioactive substances could have on the earth's ecosystem.

Considering the shortcomings and risks of utilizing nuclear and fossil fuels, several attempts have been made in recent years to explore cost-efficient ways of utilizing alternative resources of energy, such as solar, wind, and ocean-wave energy [23]. Collectively referred to as renewable resources of energy, they are readily available to harness and utilize through processes that are fairly unintrusive to the earth's ecosystem.

1.2 History and Current Status of Wave Energy Harnessing

Even to an untrained eye, the energy transported by ocean waves is hard to go unnoticed. The total wave energy available on a world scale is approximately 2 TW [24]. This is the same order of magnitude as the world's electricity consumption [24]. Therefore, wave energy could be a potentially significant contributor to the overall energy demand. The earliest known effort to harness energy from waves was made by Pire et al. in 1799 [25]. In recent years, the number of patented wave energy conversion techniques across Japan, North America, and Europe has seen a substantial increase [26]. Based on these techniques, many devices were built and tested in the late 20th century by companies and research universities. Devices that have shown great potential

in terms of energy conversion efficiency have been deployed off the coast of Scotland, Portugal, Western Australia, and the United States [27].

Wave energy extraction can be carried out in devices operating on-shore, near-shore, and off-shore depending on the operating principle of the corresponding wave energy converter (WEC) [28]. The latter is commonly utilized in order to classify these devices; according to [29], there are four categories of WECs:

1) Oscillating Water Column (OWC): These devices have a chamber that is partially submerged below the mean sea level. The chamber is partially filled with water and, thus, a free surface is formed between the water column and the air column trapped in the chamber. Due to the variation in the incoming wave elevation, the height of the water column changes in time and, thus, compresses and decompresses the trapped air column. The air flow is channeled through a double-acting turbine which is connected to a generator. Examples of OWCs are the Land Installed Marine Power Energy Transmitter (LIMPET) deployed on-shore near the Scottish island of Islay and the Oceanlinx Port MacDonnell project deployed in South Australia [29].

2) Overtopping WEC: The working principle of these devices involves capturing the water that forms the wave crest in an incoming wave front. The captured water is stored in a reservoir which is at a higher level than the average free-surface of the surrounding body of water. The stored water is then released into the sea through a series of low-head turbines. This process converts the potential energy of the stored water into electrical energy. Examples of overtopping devices are the Tapered Channel Wave Power Device (TAPCHAN) developed in Norway [28] and the Wave Dragon Project in Denmark [29].

3) Attenuator and Terminator: These devices have multiple floating segments that are hinged at specific points. They typically have one dominant horizontal dimension, which corresponds to the length of the device [30]. When deployed in a wave field, the incoming waves cause the device to

flex and move because of the hinged joints. This mechanical movement is then used to generate electricity. Devices placed perpendicularly to the wave crest are referred to as Attenuators. The device is called a Terminator when it is placed parallel to the wave crest. An example of such a device is the Pelamis WEC, which is currently deployed off-shore in Agucadoura, Portugal and in Orkney, Scotland [29].

4) Point absorber: This WEC is axisymmetric about its vertical axis and has much smaller physical dimensions relative to the incident waves. Furthermore, a typical point absorber is much smaller compared to most other types of WECs. Nonetheless, point absorbers are capable of providing high efficiency regarding their energy absorption capabilities [30]. On the other hand, the magnitude of the absorbed power from a single point absorber is relatively small and, thus, an array of point absorbers (wave farm) is typically deployed to increase the overall power absorption. An example of a point absorber WEC is the Power Buoy developed by Ocean Power Technologies, which has been deployed off the coast of Reedsport, Oregon [31].

Despite the fact that numerous WEC designs have been proposed over the last few years, wave energy technology as a whole is yet to become a viable method for production of electricity. This is due to factors such as low efficiency of wave energy devices, high installation cost, and high maintenance costs. Current estimates suggest that the cost per MWh of wave energy production is higher than 1.5 times that of wind energy and approximately three times that of coal-based energy [29]. Compared to some of the existing renewable energy conversion technologies, WEC technology is still in the early phases of development [29]. More research needs to be conducted in the field of wave energy conversion with an overall aim of eliminating barriers such as high operating costs and low conversion efficiencies of wave energy converters. Studies show that accurate prediction of ocean wave characteristics improves the efficiency of wave energy

converters [28]. Also, the earth's ecosystem will benefit from WECs, given the non-polluting nature of wave energy devices.

1.3 Summary and Objectives of the Proposed Research

The main objective of this dissertation is to develop a novel strategy for constrained discrete phase control of a WEC system of the heaving-point-absorber kind in irregular seas. The hydrodynamic modeling of the wave field around the point absorber and the modeling of the hydraulic system for the power take-off and storage is done using MATLAB®, where a code capable of performing numerical simulations of the WEC system has been developed; this part of the research is described in Chapter III. A controller based on reinforcement learning (RL) - a computational intelligence tool - is developed and utilized to obtain an optimal policy to control the point absorber WEC. The theoretical background of RL, included a case study, is provided in Chapter IV. A prediction algorithm based on radial basis function networks is also developed in order to obtain the future wave excitation that is required as input to the control algorithm in a real implementation of the proposed WEC system. The prediction algorithm is validated in benchmark problems, including time-series forecasting. Its development and validation are presented in Chapter V. An extensive parametric investigation is performed in order to provide insight into the WEC system control requirements in both regular and irregular waves. The case studies and the corresponding results for regular and irregular waves are provided in Chapters VI and VII, respectively. In order to demonstrate the effectiveness of the RL-based controller in increasing the efficiency of the WEC system while satisfying the heaving motion amplitude constraint, numerical simulations in regular and irregular waves are performed and the results are provided and discussed in Chapter VIII along with the impact of the prediction algorithm accuracy on the performance of the proposed RL-based WEC controller.

CHAPTER II

LITERATURE SURVEY

A scholarly article on the topic of utilization of wave power was published as early as 1892 by Stahl [32]. However, with the discovery of energy resources such as petroleum and nuclear fuels, the interest in ocean waves as a resource of energy gradually diminished. Nevertheless, a few researchers/inventors continued to design and develop wave energy extraction devices. Noteworthy among them is the Japanese inventor Yoshio Masuda, who developed a navigation buoy powered by wave energy [28]. In the US and Europe, the impetus for research in the design and development of wave energy extraction devices increased after the Middle-Eastern oil crisis in 1973. Pioneering research in wave energy extraction was performed by Kjell Budal and Stephen Salter in Europe [33], while in the USA, research in wave energy extraction was pioneered by Michael E. McCormick [33]. The 1974 publication of a paper in *Nature* by Stephen Salter from the University of Edinburgh on the power of waves increased awareness about the potential usage of wave energy for human needs and purposes [28]. More recently, the signing of the Kyoto protocols to reduce CO_2 emissions into the atmosphere have also helped renew the interest in wave energy extraction [33].

Since then, several wave energy extraction concepts have been proposed and studied [28]. Falnes [34] showed that a heaving point absorber is a viable concept for wave energy conversion (WEC) [34]. Point absorbers are devices that are axisymmetric about their vertical axis and have small physical dimensions (in the horizontal plane) compared to the wave length of the incident waves. As a result, they can achieve a high ratio between converted energy and structural volume. Point absorbers typically have a simple design and, thus, present less challenges from a mathematical modeling point of view [34]. For instance, due to their small physical dimensions, the scattering of the incident waves and the scattered wave field can be neglected [35] and, thus, only the

incident wave forces need to be considered. Of significant advantage is the capability of the point absorber to absorb energy many times its key horizontal dimension. Also, the point absorber-wave interaction is independent of the incident wave direction. Point absorbers can be used to harness wave energy from powerful wave regimes available in deep water (> 40 m depth) [36].

A point absorber WEC typically uses a hydraulic PTO system [36] to transform the absorbed wave energy, first, into mechanical energy and, subsequently, into electricity. Maximum energy from the ocean waves is absorbed by the point absorber WEC when it operates at resonance conditions [37]. Analytical expressions for optimal conditions of motion amplitude and phase angle for maximum power absorption have been derived for a heaving point absorber in regular waves by Falnes [35]. For a point absorber WEC, the converted energy per unit volume can be high if there are no constraints on the oscillation amplitude. However, a high oscillation amplitude can be potentially damaging to the WEC system [38]. Therefore, imposing a constraint on the heaving WEC motion amplitude is necessary. Furthermore, uncontrolled floating point absorbers will, more frequently than not, operate in off-resonance conditions resulting in lower energy absorption efficiency [37]. Clearly, protecting the WEC system while maximizing its power absorption efficiency can only be achieved by proper control of the oscillatory motion of the point absorber.

Various studies [37, 39, and 41] have shown that high power absorption efficiency can be achieved by controlling the phase of the point absorber oscillation. In this type of control, the objective is to alter the natural response of the point absorber in such a way that the point absorber's velocity and the wave excitation force reach their peak value almost at the same time [41]. This leads to resonance or near-resonance operating conditions for the WEC system, which increases the power absorption efficiency. One way of controlling the phase of the point absorber oscillation is via a power take-off (PTO) mechanism [39, 40]. A hydraulic PTO mechanism or system, usually

consists of a hydraulic cylinder, a variable or fixed displacement hydraulic motor, and several high pressure accumulators [40-42].

Falnes [40] and Eidsmoen [42] showed that high pressure accumulators can be used, as part of the hydraulic PTO system, to achieve phase control. These phase control accumulators are opened and closed in order the point absorber velocity to attain a peak value in correspondence with the instance at which the wave excitation force attains a peak value [41]. In regular waves, the phase control accumulator is opened at an instant which is approximately a quarter of the point absorber's natural period prior to the occurrence of the wave excitation force peak value [43]. A requirement for phase control is the knowledge of the future incident wave elevation [35] and, thus, an accurate prediction of the ocean wave elevation is required for effective phase control. A comprehensive survey of wave prediction algorithms can be found in [44].

The mathematical modeling and simulation of a point absorber WEC system is a key aspect of wave energy research. Early theories describing the hydrodynamics of point absorbers made various assumptions including energy extraction from regular sinusoidal waves, oscillation in a single mode (one degree of freedom), and a linear PTO [45]. Based on these assumptions, the governing equations can be linearized and solved in the frequency domain. Hulme [46] was able to determine analytically the wave forces acting on a floating hemisphere undergoing periodic oscillations. Important theoretical results such as conditions for maximum absorbed power were derived independently by Falnes [47], Mei [48], Evans [49], and Newman [50].

Nevertheless, a solution in the frequency domain cannot be obtained for irregular seas, which constitute realistic seas, and PTO mechanisms with non-linear dynamics [28]. Taking these key details into account, a time-domain theory for oscillating-body converter in irregular waves was developed by Jefferys in [51]. The theory is closely based on the Cummins equation derived for ship hydrodynamics [52]. Many studies involving active control of the point-absorber WEC in

irregular seas use a time-domain model [36-37, 41-42]. Also, theoretical studies of the hydrodynamic interactions between WECs in an array formation have been performed by Budal [53], Falnes and Budal [40], and Evans [54].

Along with the mathematical modeling of the point absorber WEC system, an accurate model of the free surface of the ocean is also required. The ocean surface is assumed to be stochastic. The sea surface is assumed to be a stationary random process and statistical estimates such as wave energy spectral density (wave spectrum) are used to describe the ocean surface elevation. Linear wave theory is used to simulate irregular waves through the linear superposition of discrete components of regular waves at various frequencies and amplitudes [55]. Wave energy spectral density can be estimated from wave-amplitude measurements obtained from buoy networks, e.g. the NOAA-NDBC buoy network around the US coastline [56]. Alternatively, wave spectral formulations, such as the modified Pierson-Moskowitz spectrum, can be utilized to model long-crested, fully developed irregular seas [57]. In the case of developing seas, the JONSWAP (Joint North Sea Wave Project) wave spectrum can be used, instead [57]. Average values of the wave spectrum parameters for different sea states in the North Atlantic can be obtained from various sources, e.g., from Lee et al. [58].

As already mentioned, the control of the WEC system will be performed by obtaining an optimal strategy using reinforcement learning, which is a computational intelligence tool. According to Kaelbling et al. [59] – 'Reinforcement learning (RL) is the problem faced by an agent that learns behavior through trial and error interactions with a dynamic environment.' According to Sutton and Barto [60] – 'Reinforcement learning is a computational approach to understanding and automating goal-directed learning and decision making.' Since its inception in 1979, RL has been used in the fields of machine learning, artificial intelligence, cybernetics, and robotics [59].

CHAPTER III

THE POINT ABSORBER WAVE ENERGY CONVERTER SYSTEM

3.1 Introduction

A point absorber WEC system is used to convert wave energy to useful electrical energy. In order to compute the motion response of the point absorber to the incident ocean waves of varying frequencies, a mathematical model for the point absorber wave energy converter (WEC) system is developed. This numerical model is used to calculate the power generated by the WEC system at different sea states and, thus, quantify its energy conversion efficiency.

A freely-floating object on the free surface of water is a familiar sight to all of us. When the free surface is calm, the object is in mechanical equilibrium with the hydrostatic forces. However, in a wavy free surface, the floating object experiences forces due to the incident waves. These forces produce motion of the object in each of the six degrees of freedom, i.e., along and/or about one or more axes shown in Figure 3.1 (for a Cartesian coordinate system).

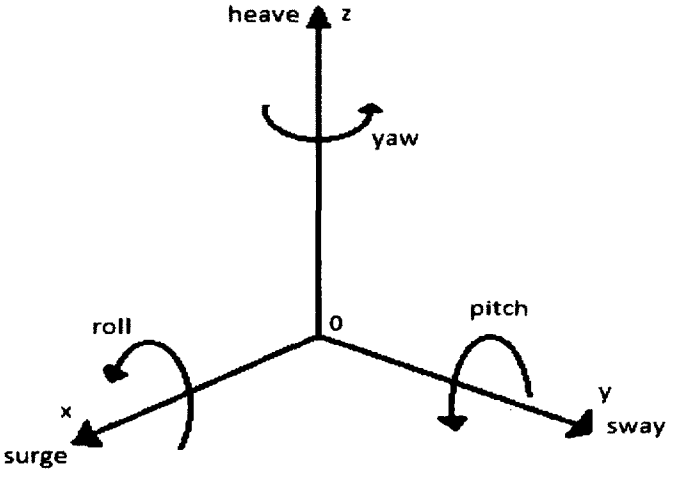

Figure 3.1. Degrees of freedom of a freely-floating object.

Using terminology commonly utilized in marine hydrodynamics, the three translational motions along the *x*, *y*, and *z* axis are termed surge, sway, and heave respectively. The three rotational motions about the *x*, *y*, and *z* axis are termed roll, pitch, and yaw, respectively. The motion of the freely-floating object due to the incident waves generates waves which propagate away from it. These outgoing, or radiating, waves exert on the object the radiation force [45] and need to be included in a mathematical model that solves the equation of motion of a WEC system.

3.2 Description of the Point Absorber Wave Energy Conversion System

In a typical point absorber WEC system, the point absorber is axisymmetric, has either a spherical or a cylindrical shape, and its motion is constrained in most degrees of freedom. The point absorber is connected to a power take-off (PTO) system and kept in place via mooring cables. The PTO system converts wave energy to electrical energy using either mechanical or electro-mechanical mechanisms. Springs and end-stop devices are included within the PTO system to mitigate the effects of shocks or jerks caused due to the motion of the point absorber. Different phase control techniques are applied to the point absorber through the PTO system.

For the purpose of this dissertation, the point absorber WEC system consists of a spherical point absorber (that is half submerged in water and is only allowed to heave) and a hydraulic PTO system. The schematic of the WEC system is displayed in Figure 3.2.

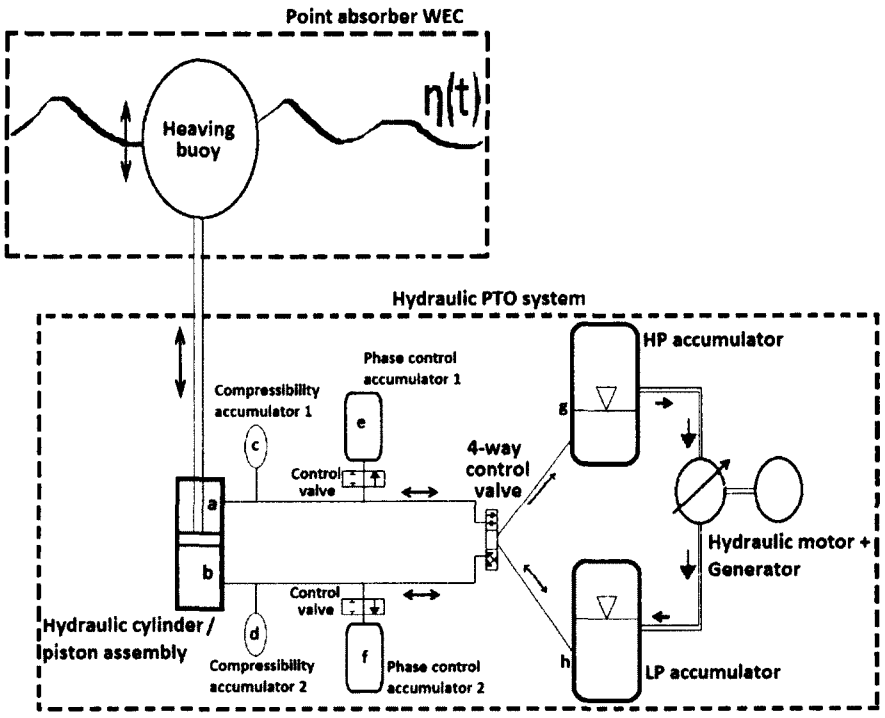

Figure 3.2. Schematic of a point absorber WEC with a hydraulic PTO system [41].

When the point absorber interacts with the wavy ocean surface, it undergoes heaving motion. The energy of the heaving point absorber is then transformed into electrical energy by the hydraulic PTO system, which consists of a piston-cylinder assembly, two compressibility accumulators (*c* & *d*), two phase control accumulators (*e* & *f*), two two-way control valves, one four-way control valve, a high pressure (HP) accumulator (*g*), a low pressure (LP) accumulator (*h*), a variable-displacement fixed-speed hydraulic motor, and an electric generator.

3.3 Operational Details of the Hydraulic Power Take-Off (PTO) System

The piston rod of the bi-directional piston in the hydraulic piston-cylinder assembly is connected to the heaving point absorber. The hydraulic cylinder contains oil with a sufficiently large bulk modulus, which is pushed out of the hydraulic cylinder by the piston due to the heaving motion of the point absorber. During operation of the system, the oil pressure on either side of the piston, i.e., *a* and *b*, is considerably higher than the atmospheric pressure. At any given instant during the

operation of the hydraulic PTO system, the pressure difference between *a* and *b* provides the power take-off force, F_{PTO}, that is applied to the point absorber. The wave excitation force must overcome the power take-off force for the point absorber to undergo motion. The oil inside the hydraulic cylinder may be subjected to pressures high enough to lead to its compression. This effect is mitigated by the introduction of two compressibility accumulators, *c* and *d* [41], which both contain gas whose pressure is approximately equal to the pressure of the oil in *a* and *b*. The compressibility accumulators also reduce any pressure peaks which might occur during operation. The oil contained in the hydraulic PTO system flows through a hydraulic circuit which connects the compressibility, the phase control, and the HP and LP accumulators.

The two phase control accumulators, *e* and *f*, are used to alter the phase of the heaving point absorber velocity. When the point absorber is not subjected to phase control, oil in the hydraulic cylinder flows either to the HP or to the LP accumulator depending on the relative magnitude of the pressure in portions *a* and *b* of the hydraulic cylinder. The direction of oil flow is controlled using a four-way control valve.

When the point absorber moves upward, the pressure in part *a* of the hydraulic cylinder becomes greater than the pressure in the HP accumulator and oil flows from *a* to the HP accumulator. When the point absorber moves downward, the pressure in portion *b* of the hydraulic cylinder becomes greater than the pressure in the HP accumulator and oil flows from *b* to the HP accumulator.

Once the operation of the WEC system begins, the pressure in the HP accumulator attains a higher value relative to the pressure in the LP accumulator and oil flows from the HP accumulator to the LP accumulator through the variable-displacement fixed-speed hydraulic motor, which is connected to the electrical generator. When the pressure in either portion *a* or portion *b* falls below the LP accumulator pressure, oil flows from the LP accumulator to either portion *a* or

portion *b* through the four-way control valve [61], and replenishes the oil of the hydraulic cylinder. The four-way control valve prevents oil from flowing from the HP accumulator into either part *a* or part *b* of the hydraulic cylinder.

As mentioned in Chapter II, when the velocity of the point absorber and the wave excitation force are in phase, the energy absorbed by the WEC is optimized [35]. Various research investigations, e.g. [35, 42], show that the usage of the phase control accumulators during the operation of the WEC system could match the phase of the point absorber velocity with the phase of the wave excitation force. Initially, the fluid in the phase control accumulators is gas [42] whose pressure varies through the course of the WEC system operation. The initial pressure in the two phase control accumulators is equal to the oil pressure in *a* and *b*. The two phase control accumulators are activated via the two two-way control valves shown in Figure 3.2. Oil either enters or leaves the phase control accumulators through these control valves. The desired alignment in the phases of the velocity and the excitation force is achieved by increasing the acceleration of the point absorber at a specific instant so that the point absorber's velocity attains a maximum value at the same instant when the wave excitation force attains its maximum value [41].

Several heuristic approaches to determine the appropriate opening instant of the control valve for the phase control accumulators have been proposed [42, 62, and 63]. A typical heuristic rule corresponds to the optimal policy in regular waves, i.e., open the control valve to the phase control accumulator at an instant equal to a quarter of the heave natural period of the point absorber before the instant at which the wave excitation force attains a peak (maximum) value. For effective use of the phase control accumulators, it is obvious that knowledge of the future wave excitation force is required [64].

Let us assume that the wave excitation force is predicted to attain positive values in the immediate future and the nearest maximum is determined. As the point absorber starts to move

upwards, the phase control accumulator (*e*) is opened a quarter of the resonance period of the point absorber before the instant at which the wave excitation force is predicted to attain the maximum positive value. Due to the relatively low pressure in the phase control accumulator (*e*), the point absorber accelerates, oil is pumped into phase control accumulator (*e*) and, thereby, the gas pressure in (*e*) increases. After a period of acceleration, the point absorber comes to rest. At this moment, the control valve of the phase control accumulator (*e*) is closed. The pressurized phase control accumulator (*e*) is discharged into part *a* of the hydraulic cylinder when the point absorber starts to move downwards [41].

On the other hand, when the wave excitation force is predicted to attain negative values in the immediate future, the aforementioned sequence of events is repeated, but now, given that the direction of motion of the point absorber is downward, phase control accumulator (*f*) is used to achieve phase alignment. As a result of phase control, the power take-off mechanism of the hydraulic PTO system is strongly non-linear [41, 61]. In the following sections of this chapter, the mathematical model of a heaving point absorber connected to a non-linear hydraulic PTO system is provided. A MATLAB® code has been developed based on this mathematical model (see Appendices A, B, and C).

3.4 Mathematical Modeling of a Heaving Point Absorber with a Hydraulic PTO System

The mathematical model for the heaving point absorber WEC with a hydraulic PTO system must collectively represent the wavy ocean surface, the point absorber's heaving motion, and the flow in the hydraulic PTO system.

Ocean waves are modeled using linear wave theory. The fluid flow is assumed to be inviscid, irrotational, and incompressible [65]. A velocity potential for the fluid flow domain can then be defined. Additionally, the wave height is assumed to be small when compared to the wavelength and the water depth. Therefore the ocean surface boundary conditions can be linearized. Due to

the small wave amplitude or height assumption, the Keulegan-Carpenter number is less than three. Therefore, there is insufficient time for vortices to develop at the wave-body interface [66] and, thus, the fluid flow around the point absorber can be modeled using potential flow theory. The linearization allows for the fluid forces on the point absorber to be decomposed into three components: the incident wave force, the radiation force, and the hydrostatic force. The linear combination of the incident wave force and the radiation force is the total hydrodynamic force acting on the point absorber. The incident wave force is decomposed into the excitation force and the diffraction force. The radiation force consists of added mass and radiation damping terms [65]. Using the Froude-Krylov approximation, the diffraction forces are assumed to be small and, therefore, can be neglected.

The motion response of the heaving point absorber is assumed to be small compared to the body dimensions of the point absorber. More importantly, the point absorber's motion response is assumed to be proportional to the fluid forces that are exerted on it. The point absorber's heaving motion response to the incident ocean waves can be mathematically modeled in either the frequency domain or the time domain [66]. Modeling in the frequency domain assumes that the wavy ocean surface comprises only monochromatic or regular waves and, thus, the heaving point absorber executes steady harmonic oscillations. Non-linearities are introduced to the point absorber's motion when the point absorber is subjected to either phase control or motion constraints by the hydraulic PTO system. Due to these key details, a non-linear mathematical model for the heaving point absorber developed in the time domain is used.

As shown in Figure 3.2, the hydraulic PTO system consists of several key components. In this investigation, two fluids – oil and gas, are used in the hydraulic circuit. Oil with a large bulk modulus is chosen as the working fluid in the hydraulic cylinder. The power take-off force F_{PTO} is applied to the point absorber by the hydraulic PTO system. The direction and magnitude of this

force are determined by the magnitude of pressure in the compressibility accumulators of the hydraulic PTO system [67]. The buoyancy force on the point absorber is balanced by the weight of the buoy and the pre-tension force in the mooring cables. The fluid flow inside the hydraulic circuit is assumed to be one-dimensional and frictional losses in the pipes are neglected.

During operation, the compression and expansion of the gas inside the compressibility, the phase control, and the HP and LP accumulators is assumed to be an isentropic process [68]. This assumption implies that no heat is allowed to enter or leave the accumulators and the frictional effects are assumed to be zero. The assumption of an isentropic process is reasonable given the short time scales over which the expansion and compression of the gas occurs in comparison to the temperature changes in the surrounding water. The walls of the accumulators and the ducts of the hydraulic circuitry are assumed to be rigid. The fluid pressure losses due to fluid flow within the hydraulic circuit are assumed to be negligible. The total volume of gas inside the hydraulic PTO system is kept constant.

3.5 Time-Domain Hydrodynamic Model of a Heaving Point Absorber

The motion of a heaving point absorber due to incident ocean waves is analyzed in the time domain using the mathematical model developed by Cummins [52]. Even though the Cummins model was originally used to analyze ship motion in rough seas, it was later modified and applied to wave energy converters by Jefferys [69]. This model can be used to analyze the dynamics of point absorber WEC systems that have non-linear PTO systems. According to [45], the equation describing the body dynamics of a point absorber WEC system in the time domain for a single degree of freedom (heave) is:

$$(m_b + m_a)\,\ddot{\zeta}(t) + \int_0^t [\dot{\zeta}\,(t-\tau)\,K\,(t)]\,d\tau + F_{PTO} + (k_{hs})\zeta\,(t) = w_{exc}(t) \tag{3.1}$$

where:

$m_b = \rho\left(\frac{2}{3}\right)\pi r^3$ is the mass of the point absorber,

ρ is the density of water,

r is the radius of the spherical point absorber,

m_a is the added mass of the point absorber,

$K(t)$ is the radiation force kernel for radiation damping of the point absorber,

F_{PTO} is the externally applied power take-off (PTO) force from the hydraulic PTO system,

$k_{hs} = \rho g \pi r^2$ is the hydrostatic stiffness,

$w_{exc}(t)$ is the excitation force from either regular waves or irregular seas,

$\ddot{\zeta}(t)$ is the acceleration of the point absorber at time *t*,

$\dot{\zeta}(t)$ is the velocity of the point absorber at time *t*,

and $\zeta\ (t)$ is the displacement of the point absorber at time *t*.

In order to solve this integro-differential equation, a code has been developed in MATLAB® (see Appendix A), which is used to compute the response (displacement and velocity) of the point absorber WEC system to either regular waves or irregular seas. In Eq. (3.1), the radiation force is represented by a convolution integral whose integrand is commonly referred to as the radiation force kernel. It has the form of an impulse response function. The radiation kernel, $K(t)$, depends only on the body shape and is independent of the body dynamics [66].

3.5.1 Computation of the excitation force due to regular waves

In regular waves (monochromatic seas), the wave excitation force is assumed to be sinusoidal. It is calculated for a particular wave frequency using the formula shown below.

$$w_{exc}(t) = f_{amp} * sin\left(\left(\frac{2\pi}{T}\right) * t_m\right) \tag{3.2}$$

where $w_{exc}(t)$ is the wave excitation force, f_{amp} is the wave excitation force amplitude, T is the wave period, and t_m is the discretized time instant. The wave force amplitude, f_{amp}, is calculated for a given wave amplitude using the following formula [55], which is derived from the Haskind relation [65],

$$f_{amp} = w_{amp}\sqrt{\frac{2\rho g^3 B(\omega)}{(2\pi/T)^3}} \tag{3.3}$$

where w_{amp} is the wave amplitude, ρ is the density of water, g is the acceleration due to gravity, and $B(\omega)$ is the radiation damping of the spherical point absorber.

The radiation damping $B(\omega)$ at a particular frequency is estimated by using the radiation damping coefficients derived by Hulme [46] for a spherical point absorber undergoing forced periodic oscillations. These are listed in Appendix D as a function of non-dimensionalized wave frequency. A piecewise cubic Hermite polynomial is fitted to the set of radiation damping coefficients, so that the radiation damping of the spherical point absorber can be estimated at any wave frequency during the numerical simulations.

In regular waves, the added mass m_a of a heaving spherical point absorber at a certain wave frequency is calculated in a similar manner as the radiation damping coefficient. Specifically, the added mass coefficients calculated by Hulme [46] for specific wave frequencies (see Appendix E) are interpolated using a piecewise cubic Hermite polynomial. In irregular seas, the added mass of a heaving spherical point absorber is computed at infinite frequency m_∞ [66] and has a value equal to 50% of the point absorber structural mass.

3.5.2 Computation of the wave excitation force in irregular seas

For the case of irregular waves (polychromatic seas), the ocean surface is modeled as a stationary random process using the modified Pierson-Moskowitz spectrum for a given sea state,

$$S(\omega) = (((1.25/4)\cdot {\omega_m}^4 \cdot \left(H_{\frac{1}{3}}\right)^2)/\omega^5)\cdot exp(-1.25\cdot(\omega_m/\omega)^4) \tag{3.4}$$

where $S(\omega)$ is the wave energy spectral density, ω is a frequency value obtained from a specific frequency range, ω_m is the modal (peak) frequency, and $H_{1/3}$ is the significant wave height, which is the mean of one-third of the highest waves. The statistics of different sea states in the North Atlantic [55] (also listed in Appendix F) are utilized in order to obtain values for ω_m and $H_{1/3}$.

In order to calculate the wave excitation force, the spectral density of the wave excitation force $S_{fe}(\omega)$ is computed through the spectral density of the wave spectrum [70],

$$S_{fe}(\omega) = |f_e(\omega)|^2 \cdot S(\omega) \tag{3.5}$$

where $f_e(\omega)$ is the excitation force per unit incident wave amplitude at wave frequency ω. The formula for the wave excitation force amplitude is obtained using the Haskind relations [65],

$$|f_e(\omega)|^2 = \left|\frac{2\rho m_b g^3 B(\omega)}{\omega^2}\right| \tag{3.6}$$

The random process that models the ocean surface is assumed to follow a Gaussian distribution [71]. Therefore, based on the theory of Gaussian processes [72], two independent random variables a_n and b_n are chosen from a common Gaussian distribution with variance $\Delta\omega \cdot S_{fe}$. Here the variable $\Delta\omega$ is the frequency interval used to discretize the wave spectrum. The expressions for a_n and b_n are:

$$a_n = \sqrt{\Delta\omega \cdot * S_{fe}(\omega))} \cdot N(0,1) \tag{3.7}$$

$$b_n = \sqrt{\Delta\omega \cdot * S_{fe}(\omega))} \cdot N(0,1) \tag{3.8}$$

In the above equations, $N(0,1)$ is a normally distributed pseudorandom number with zero mean and variance equal to 1, and n is the number of points in the time series of the numerical simulation. Therefore, the independent random variables a_n and b_n correspond to the coefficients of a discrete Fourier series in the frequency domain. The values of these variables are computed with the assumption that the wave excitation force is in phase with the wave elevation,

i.e., the point absorber contours the waves. In order to compute the wave excitation force in the time domain an inverse fast Fourier transform is performed.

3.5.3 Computation of the power take-off (PTO) force of the hydraulic system

The power take-off force, F_{PTO}, is calculated in both regular and irregular seas using the following expression [68]:

$$F_{PTO} = S_p(P_c - P_d) \tag{3.9}$$

In Eq. (3.9), S_p is the cross-sectional area of the piston, P_c is the pressure of gas in the compressibility accumulator *c*, and P_d is the pressure of gas in the compressibility accumulator *d*. As the gas in the compressibility accumulators is assumed to undergo an isentropic process, the gas pressures, P_c and P_d, are computed using the following equations [73]:

$$P_c(i+1) = P_c(i)\left(\frac{V_c(i)}{V_c(i+1)}\right)^{\gamma} \tag{3.10}$$

$$P_d(i+1) = P_d(i)\left(\frac{V_d(i)}{V_d(i+1)}\right)^{\gamma} \tag{3.11}$$

where V_c and V_d are the volume of gas in compressibility accumulators *c* and *d*, respectively, γ is the ratio of specific heat for the gas used in the accumulators, and i is the discretized time index. Assuming isentropic process in the other accumulators, as well, similar expressions for the gas pressure and volume can be derived:

$$P_e(i+1) = P_e(i)\left(\frac{V_e(i)}{V_e(i+1)}\right)^{\gamma} \tag{3.12}$$

$$P_f(i+1) = P_f(i)\left(\frac{V_f(i)}{V_f(i+1)}\right)^{\gamma} \tag{3.13}$$

$$P_g(i+1) = P_g(i)\left(\frac{V_g(i)}{V_g(i+1)}\right)^{\gamma} \tag{3.14}$$

$$P_h(i+1) = P_h(i)\left(\frac{V_h(i)}{V_h(i+1)}\right)^{\gamma} \tag{3.15}$$

As shown in Figure 3.2, the hydraulic cylinder, the compressibility accumulators, the phase control accumulators, and the HP and LP accumulators are inter-connected through ducts which form the hydraulic circuit of the PTO system. When the piston moves due to the motion of the point absorber and displaces fluid within the hydraulic circuit, the magnitude of pressure and volume in every accumulator changes. Therefore, a set of expressions that relates the hydraulic fluid flow rate from either part of the hydraulic cylinder to the pressure and volume in each accumulator is required. The set of expressions is as follows [41]:

For the compressibility accumulators:

$$-m_c\frac{dv_c}{dt} = S_p\zeta(\dot{t}) - u_l C_v A_v\sqrt{\frac{2}{\rho_{oil}}max\left((P_c - P_g),0\right)} + u_l C_v A_v\sqrt{\frac{2}{\rho_{oil}}max\left((P_h - P_c),0\right)}$$

$$+ (u_l - 1)C_c A_c\sqrt{\frac{2}{\rho_{oil}}|P_c - P_e|}\cdot sign(P_c - P_e) \tag{3.16}$$

$$-m_d\frac{dv_d}{dt} = -S_p\zeta(\dot{t}) - u_l C_v A_v\sqrt{\frac{2}{\rho_{oil}}max\left((P_d - P_g),0\right)} + u_l C_v A_v\sqrt{\frac{2}{\rho_{oil}}max\left((P_h - P_d),0\right)}$$

$$+ (u_l - 1)C_c A_c\sqrt{\frac{2}{\rho_{oil}}|P_d - P_f|} * sign(P_d - P_f) \tag{3.17}$$

For the phase control accumulators:

$$-m_e\frac{dv_e}{dt} = -(u_l - 1)C_c A_c\sqrt{\frac{2}{\rho_{oil}}|P_c - P_e|} * sign\,(P_c - P_e) \tag{3.18}$$

$$-m_f\frac{dv_f}{dt} = -(u_l - 1)C_c A_c\sqrt{\frac{2}{\rho_{oil}}|P_d - P_f|} * sign\,(P_d - P_f) \tag{3.19}$$

For the HP and LP accumulators:

$$-m_g \frac{dv_g}{dt} = u_l C_v A_v \sqrt{\frac{2}{\rho_{oil}} \max\left((P_c - P_g), 0\right)} + u_l C_v A_v \sqrt{\frac{2}{\rho_{oil}} \max\left((P_d - P_g), 0\right)} - q_m \tag{3.20}$$

$$-m_h \frac{dv_h}{dt} = -u_l C_v A_v \sqrt{\frac{2}{\rho_{oil}} \max\left((P_h - P_c), 0\right)} - u_l C_v A_v \sqrt{\frac{2}{\rho_{oil}} \max\left((P_h - P_d), 0\right)} + q_m \tag{3.21}$$

where:

m, v, and P are the mass, specific volume, and pressure of gas, respectively, in the corresponding accumulator (refer to Figure 3.2),

C_v is the discharge coefficient of the control valve to the compressibility accumulators *c* & *d*,

C_c is the discharge coefficient of the control valve to the phase control accumulators *e* & *f*,

ρ_{oil} is the density of the oil used in the hydraulic circuit,

A_v is the cross-sectional area of the control valve to the HP & LP accumulators,

A_c is the cross-sectional area of the control valve to the phase control accumulators,

S_p is the cross-sectional area of the piston in the hydraulic cylinder,

u_l is the phase control activation parameter, and

q_m is the volumetric flow rate through the hydraulic motor.

The differential term on the left hand side of Eqs. (3.16-3.21) represents the rate of change of specific volume of gas in each accumulator. The value of the volume of the gas in each accumulator at step i is computed using a forward differencing scheme:

$$m_\alpha \frac{dv_\alpha}{dt} = \left[\frac{V_\alpha(i+1) - V_\alpha(i)}{\Delta t}\right] \tag{3.22}$$

where α is any one of the accumulators (*c, d, e, f, g & h*) in the hydraulic PTO system and Δt is the time interval. The phase control activation parameter u_l is a binary parameter used to activate the phase control accumulators (*e & f*) of the hydraulic PTO system:

$$u_l = \begin{cases} 0, & Phase\ control\ activated \\ 1, & No\ phase\ control \end{cases} \tag{3.23}$$

The pressure difference between the HP and the LP accumulators is used to operate a variable-displacement, fixed-speed hydraulic motor. The fixed rotational speed of the hydraulic motor S_{hm} is set at 3,000 revolutions per minute; the corresponding angular speed is $\omega_{hm} = 2\pi S_{hm}/60$. The volumetric flow rate through the hydraulic motor q_m is computed using the following expression [74]:

$$q_m = \frac{f_{dc} D_{max} \omega_{hm}}{2\pi} \tag{3.24}$$

where D_{max} is the maximum volumetric displacement of the motor and f_{dc} is the utilized fraction of D_{max}. The torque of the generator matches the torque of the hydraulic motor during the operation of the WEC system. The hydraulic motor torque T_m is computed using the following expression:

$$T_m = \frac{f_{dc} D_{max} (P_g - P_h)}{2\pi} \tag{3.25}$$

The generated electrical power P_{gw} is calculated using the following expression:

$$P_{gw} = T_m \cdot \omega_{hm} \tag{3.26}$$

3.5.4 Computation of the phase control accumulator opening instance

The phase control accumulator opening instant, t_{pco}, is defined as the instant at which the control valve to the phase control accumulator is opened. For the purpose of this investigation, the opening instant t_{pco} is computed using the following expression:

$$t_{pco} = t_{fpeak} - \frac{T_0}{C_{coe}} \tag{3.27}$$

where t_{fpeak} is the instant at which the wave excitation force attains a local-peak value, T_0 is the heave natural resonance period, and C_{coe} is the control coefficient. The latter is utilized as a parameter in order to study its effect on the power absorption efficiency of the WEC system. Along with phase control, the case of having no phase control on the point absorber is also considered.

3.5.5 Computation of the radiation force (convolution integral) of the point absorber

The radiation force is represented in Eq. (3.1) by a convolution integral. The computation of the convolution integral is performed using the trapezoidal rule. In this way, the value of the convolution integral at time t_N is computed as follows:

$$\int_0^{t_N} \dot{\zeta}\,(t-\tau)\,K\,(t)\,d\tau \approx \frac{1}{2}\Delta t K(t_N)\dot{\zeta}(0) + \frac{1}{2}\Delta t\,K(0)\dot{\zeta}(t_N) + \sum_{i=2}^{N} \Delta t\;K(t_N - t_{i-1})\,\dot{\zeta}(t_{i-1}) \quad (3.28)$$

The radiation damping kernel is a causal impulse response function which depends only on the body geometry [66]. The analytical formula for the radiation damping kernel is the following:

$$K(t) = m_b\,\frac{2}{\pi}\int_0^{\infty} B(\omega)\cos(\omega t)\,d\omega \quad (3.29)$$

The numerical code used to compute the convolution integral is provided in Appendix C.

3.6 Solving the Integro-Differential Equation for the Heaving Point Absorber

The time-domain equation of the heaving motion of a point absorber given in Eq. (3.1) is solved numerically using a non-adaptive version of the fourth order Runge-Kutta method (R-K4). The solver is listed in Appendix B. The solver computes the displacement and velocity of the heaving point absorber at each discrete time *t*. These values are subsequently utilized to compute the average power absorbed by the heaving point absorber for the specified simulation time.

CHAPTER IV

REINFORCEMENT LEARNING

4.1 Introduction

Reinforcement learning (RL) is an unsupervised learning technique where an agent learns a certain behavior by interacting with the surrounding environment. Reinforcement learning has evolved from fields like cybernetics, neuroscience, psychology, statistics, and computer science [59]. A distinctive feature of reinforcement learning is that the agent learns a certain behavior by interacting with the environment, whereas, in supervised learning the agent learns a certain behavior from the instructions it receives from a supervisor [60].

Every action taken by the agent is evaluated using a reward function. Based on the accumulated reward, the agent learns the appropriate behavior for a given environmental setting. The environment can either be static or dynamic in nature. RL has been utilized to control complex technical systems like flight control, avionics, and automated manufacturing systems [76].

4.2 Reinforcement Learning Model

The reinforcement learning model (Figure 4.1) consists of an agent B, the agent's surrounding environment S, and the interaction between the agent and its surrounding environment at every discrete time t. Everything external to the agent constitutes the surrounding environment and is characterized by its state s at time t [60]. The interaction entails the agent taking an action a on the surrounding environment at each time t. Every action the agent takes is evaluated by the environment and a reward r is computed. The information about the reward and the state s of the environment is passed on to the agent for further usage in action selection.

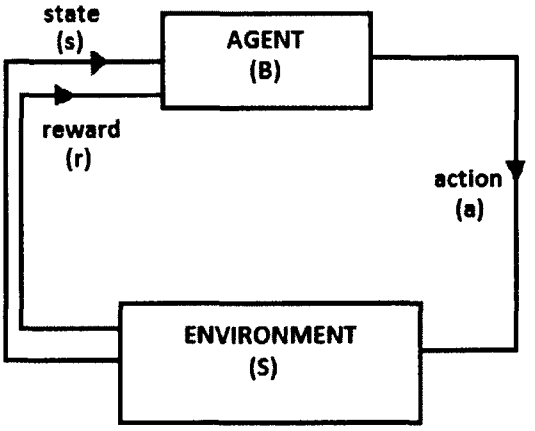

Figure 4.1. Interactions between the agent and the environment in reinforcement learning.

Initially, the agent implements a policy denoted by π at each discrete time t. This policy associates every state s and action a to the probability $(\pi(s, a))$ of taking the action a when the environment is in state s. The policy is repeatedly modified by the agent depending on the experience learned through their interaction with the surrounding environment. In the reinforcement learning problem, the agent is tasked with searching for an optimal value function which maps states to actions and maximizes the long-term accumulated reward [60]. The optimal policy for the problem is obtained from the optimal value function.

The environment in the RL model is external to the agent. The agent uses the information about the environment's current state to formulate and execute a response. This information is conveyed to the agent through a signal called the state signal. The state signal is expected to have all the relevant information about the environment's current state. A state signal which successfully retains all the relevant information is said to have the Markov property; the corresponding state is called a Markov state [60].

The concepts of Markov signal and Markov state can be illustrated with an example of a chess game. At any given time t during a chess game, the positions of the chess pieces provide the relevant information necessary to decide on the future course of action. Information about the

history of the path that have been followed by each chess piece is irrelevant. A signal about the state of the chess game has the Markov property and, therefore, the state of the chess game is a Markov state. In general, if a reinforcement learning task satisfies the Markov property, it can be modelled as a Markov decision process (MDP). Furthermore, if the reinforcement learning task has a finite number of states and action values, it is termed a finite MDP.

In a finite MDP, for a given state *s* and action *a*, the probability of occurrence of a possible next state *s'* is called the transition probability, which is calculated as:

$$P_{ss'}^{a} = Pr\{s_{t+1} = s' | s_t = s, a_t = a\} \tag{4.1}$$

A collection of transition probability values is called the transition probability set. A well-defined finite MDP has a transition probability set. The expected reward *r* of an action *a* taken in state *s* thereby leading to the transition to the next state s' is calculated as follows,

$$R_{ss'}^{a} = E\{r_{t+1} | s_t = s, a_t = a, s_{t+1} = s'\} \tag{4.2}$$

The interactions that occur between the agent and its surrounding environment can be divided into two categories [60]: Continuous interactions and episodic interactions. Interactions that occur continuously between the agent and its surrounding environment are called continuous interactions. The agent receives continuous feedback from the environment and learns the optimal behavior. In episodic interactions, the agent interacts with the environment on an episode-by-episode basis. The feedback, i.e., the accumulated reward, from each episode is used by the agent to formulate an optimal policy. Episodic interactions are mathematically easier to handle because of the finite number of reward values in every episode.

Considering the fact that the objective of RL is to find a policy which maximizes the accumulated reward or the expected return in the long term, the manner in which rewards are computed becomes very important. Basically, reward is a numerical value (r_t) awarded to the agent that takes an action a_t when the environment is in state s_t at time *t*. For an RL task with *N* discrete

time instants, the agent can receive rewards at each time t. The total sum of all the rewards is referred to as the expected return (R_t). The expression for R_t is given as,

$$R_t = \sum_{t=0}^{N}(r_t) \tag{4.3}$$

The above expression is for a RL task in which the interaction between the agent and the environment is episodic with t_N being the final step. Such RL models are called finite-horizon models. For RL tasks that involve continuous interaction with the environment (infinite-horizon models), the calculation of the expected return is modified by including a discount rate γ:

$$R_t = \sum_{t=0}^{\infty}(\gamma^t\ r_t) \tag{4.4}$$

The discount rate estimates the present value of a future reward. Its value can be assigned in the range between 0 and 1.

The ultimate goal of RL is to search and find an optimal policy (π^*) so that the expected return is maximized. The RL algorithm searches for the optimal policy using value functions. A value function provides an estimate of the expected return by associating the state of the environment to the actions taken by the agent when following a specific policy. Whereas reward functions provide an estimate of how good the action taken is in the short term, value functions provide a goodness estimate of actions taken in the long term.

State-based value functions, or state-value functions, (V^π) and action-based value functions, or action-value functions (Q^π), can be constructed by an agent following a policy π in a reinforcement learning task modelled as a MDP. The state-value function (V^π) estimates the expected return given a starting state s of the environment upon which the agent follows a policy π, and is defined as follows,

$$V^\pi(s) = E_\pi\{R_t|s_t = s\} \tag{4.5}$$

In the above formulation, $E_\pi\{\ \}$ is the expected return when a policy π is followed; R_t is the reward obtained in state s_t at time t. The action-value function (Q^π) estimates the expected reward

when the agent takes an action a while the environment is in state s and thereafter follows a policy π. The action-value function ($Q^{\pi}(s,a)$) is defined as follows,

$$Q^{\pi}(s,a) = E_{\pi}\{R_t | s_t = s, a_t = a\} \quad (4.6)$$

In the above formulation, $E_{\pi}\{\}$ is the expected return for action a_t taken by the agent in state s_t under policy π. In conclusion, a solution to a RL task provides a policy that maximizes the expected return in the long term. Such a policy is called the optimal policy (π^*). The value functions for this policy are called optimal state-value function $V^*(s)$ and optimal action-value function $Q^*(s,a)$.

4.3 Methodologies to Solve Reinforcement Learning Problems

Three solution methodologies are widely used to solve reinforcement learning problems are [60]: Dynamic Programming (DP) methods, Monte Carlo (MC) methods, and Temporal-difference (TD) learning methods. The RL approach adopted in this research, Q-learning [77], is based on TD learning. A concise description of TD-learning and Q-learning is provided in the following section.

4.3.1 Temporal-difference learning

Temporal-difference (TD) learning is a hybrid methodology of the MC and DP methods. In TD learning, the agent learns the optimal behavior both through experience (like in MC methods) gained by interacting with the environment and, also, by using other estimates such as action-values or state-values (like in DP methods). There are three main approaches in TD learning [60]: Sarsa, Q-learning, and Actor-Critic methods. A variant of Q-learning is the method utilized in this research.

Q-learning involves the construction of a matrix known as the Q-matrix. The Q-matrix is iteratively updated in every RL trial (or episode). The elements of the Q-matrix are computed using the Q function. The environment is approximately represented by a set of discrete states S. The set of actions A that can be taken by the agent is also specified. Using the Q-function and the action set,

the Q-matrix is updated in every trial. If the environment at time t occupies state s_t, and action a_t is taken by the agent, the Q function is updated as follows [78],

$$Q(s_t, a_t) \leftarrow Q(s_t, a_t) + \alpha\,[R(s_t, a_t) + \gamma \max Q(s_{t+1}, a) - Q(s_t, a_t)\,] \tag{4.7}$$

In the above expression, $R(s_t, a_t)$ is the reward or reinforcement function for the action a_t taken when the environment is in state s_t. The parameters α and γ correspond to the learning rate and the discount rate, respectively. The reward is a system-dependent function. After a sufficient number of trials has been performed, Q-learning converges to the policy that is optimal for the RL task at hand. In the following section, a case study using Q-learning to solve a RL task is presented.

4.3.2 Case Study: Using RL to Control a Heating Coil

The research presented in [79] by Anderson et al., explores the possibility of utilizing computational intelligence techniques, such as neural networks (NNs) and reinforcement learning (RL), to improve the efficiency of PI feedback controllers of HVAC systems. Anderson et al. explore an alternative approach wherein the output of a single PI feedback controller is augmented by the output of an adaptive system which uses a combination of NNs and RL. In As part of this research, and in order to evaluate the capabilities of RL, it was decided to perform the same test but to utilize only RL to augment the PI controller.

A schematic of the heating coil with the PI controller is provided in Figure 4.2. The heating coil consists of an inlet, an exit, and the coil itself. Water enters the coil at a flow rate f_w and temperature T_{wi}. Air enters the inlet section at a flow rate f_a and temperature T_{ai}. Heat exchange occurs between the low temperature air and the high temperature water and, thus, air flows out of the exit section at a higher temperature T_{ao}. Water leaves the coil at a lower temperature T_{wo}. The PI feedback controller is trying to reach the requested temperature set point T_{sp} for the air

temperature at the exit by generating the control signal c which controls the water flow rate f_w to the coil.

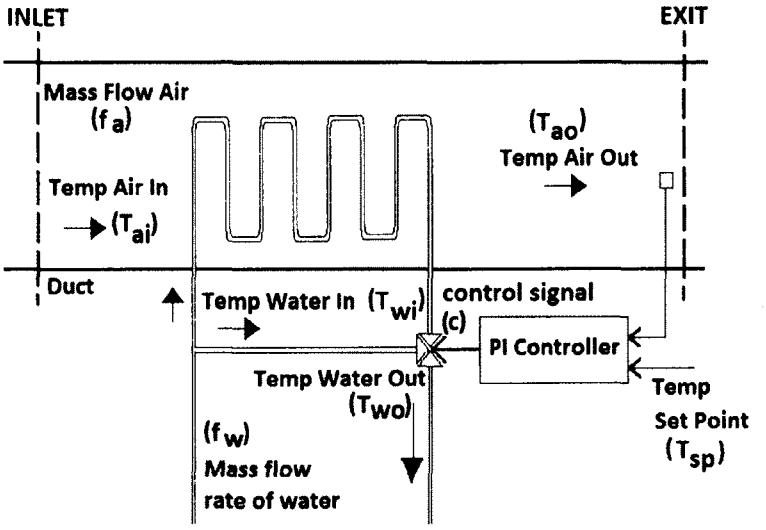

Figure 4.2. Schematic of the heating coil with the PI controller.

A mathematical model of the heating coil, developed by Underwood and Crawford [80], is used.

$$f_w(t) = 0.008 + 0.00703 \cdot (-41.29 + 0.30932 \cdot c(t-1) - 3.2681 \cdot 10^{-4} \cdot c(t-1)^2 + \\ + 9.56 \cdot 10^{-8} \cdot c(t-1)^3) \quad (4.8)$$

$$T_{wo}(t) = T_{wo}(t-1) + 0.64908 \cdot f_w(t-1) \cdot \left(T_{wi}(t-1) - T_{wo}(t-1)\right) + \left(0.02319 + \\ + 0.10357 \cdot f_w(t-1) + 0.02806 \cdot f_a(t-1)\right) \cdot \left(T_{ai}(t-1) - \frac{\left(T_{wi}(t-1) + T_{wo}(t-1)\right)}{2}\right) \quad (4.9)$$

$$T_{ao}(t) = T_{ao}(t-1) + 0.19739 \cdot f_a(t-1) \cdot \left(T_{ai}(t-1) - T_{ao}(t-1)\right) + \left(0.03184 + \\ + 0.15440 \cdot f_w(t-1) + 0.04468 \cdot f_a(t-1)\right) \cdot \left(\frac{\left(T_{wi}(t-1) + T_{wo}(t-1)\right)}{2} - T_{ai}(t-1)\right) + 0.20569 \cdot \\ \left(T_{ai}(t) - T_{ai}(t-1)\right) \quad (4.10)$$

The constants in the above expressions are determined by applying the method of least squares to the measurements from the actual heating coil. The state of the virtual heating coil at any given time is represented by the temperatures and flow rates of air and water at the inlet and exit

sections. The inlet temperature of water T_{wi}, the inlet flow rate of air f_a and the inlet temperature of air T_{ai} are randomly varied over the specific ranges listed in Table 4.1.

Input parameters	Range of variation
Inlet water temperature (T_{wi})	73 ^{0}C – 81 ^{0}C
Inlet air temperature (T_{ai})	4 ^{0}C – 10 ^{0}C
Inlet air flow rate (f_a)	0.7 kg/s – 0.9 kg/s

Table 4.1. Range of variation for key input variables.

Before applying the RL algorithm to the PI controller, the proportional and the integral gains of the controller are determined. The PI controller tuning algorithm is as follows,

$$c'(t) = k_p\, e(t) + k_i \int e(t)\, dt \tag{4.11}$$

In the above expression, k_p is the proportional gain, k_i is the integral gain, $e(t)$ is the difference between the set-point temperature T_{sp} and the actual outlet air temperature T_{ao} at time t, and $c'(t)$ is the normalized control signal in the range from 0 to 1. The set-point temperature is changed every 100 seconds. The optimal values of k_p and k_i were found to be 0.185 and 0.0178, respectively [79], after tuning the PI controller. The value of the control signal c ranges from a minimum of 670 (valve fully open) to a maximum of 1400 (valve fully closed). The PI controller tries to minimize $e(t)$ by varying $c(t)$. Even though the PI feedback controller is suited to perform this task, the possibility of augmenting the efficiency of the PI controller using RL is explored. The schematic of the RL algorithm applied to the PI controller along with the heating coil is shown below. This combination is henceforth referred to as the RL/PI controller. The value of each variable is allowed to vary in the specific ranges listed in Table 4.2.

Each of the seven variables is discretized into six intervals with equal length, such that the state space of the heating coil system consists of 6^7 states. The RL agent performs an action on the

control signal. This action involves adding a certain value, selected from the action matrix A, to the PI controller control signal: $A = \{-100, -50, -20, -10, 0, 10, 20, 50, 100\}$. The reward function $R(t)$ is defined as follows,

$$R(t) = -\left(T_{sp}(t) - T_{ao}(t)\right)^2 + \beta\,(a_t - a_{t-1})^2 \tag{4.12}$$

In the above expression, the terms a_t and a_{t-1} are the indices of the action values from the action matrix A obtained at consecutive discrete times. The value of parameter β is set at 0.1.

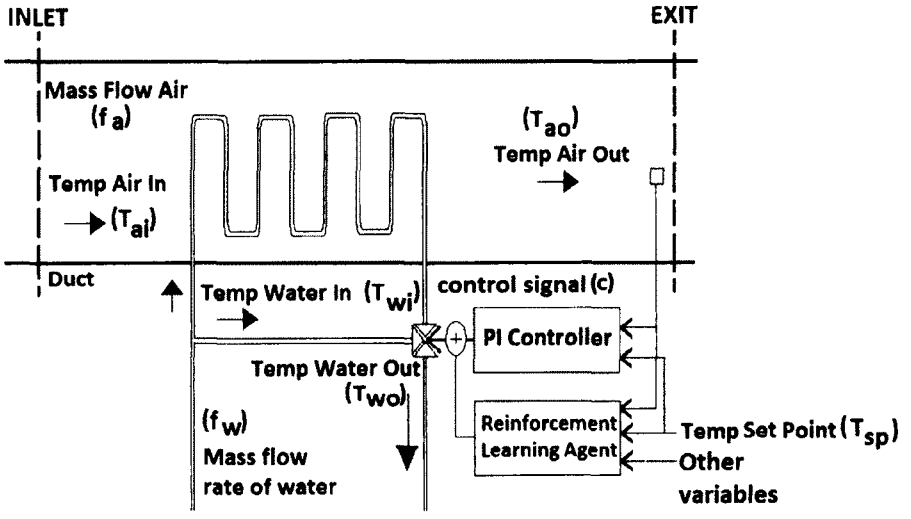

Figure 4.3. RL agent applied to the PI controller.

Input variables to the RL/PI controller	Range
Inlet water temperature (T_{wi})	73 ^{0}C – 81 ^{0}C
Inlet air temperature (T_{ai})	4 ^{0}C – 10 ^{0}C
Inlet air flow rate (f_a)	0.7 kg/s – 0.9 kg/s
Exit air temperature (T_{ao})	36 ^{0}C – 52 ^{0}C
Exit water temperature (T_{wo})	40 ^{0}C – 60 ^{0}C
Inlet water flow rate (f_w)	0.10317 kg/s – 0.34546 kg/s
PI controller control signal (c)	670 – 1400

Table 4.2. Ranges for the variables of the RL/PI controller.

In order to generate the Q-values for the heating coil system, a MATLAB® code was developed (see Appendix H) and executed for 1000 episodes. The set-point temperature is defined at the beginning of each episode and is changed after 500 steps. The parameters α and γ are assigned values of 0.1 and 0.95, respectively. The Q-learning algorithm converges to an optimal policy only after a sufficient number of trials has been performed. A random action is chosen with probability p_t at time t and the action with the maximum Q value at the corresponding state is selected with probability 1-p_t. The probability value is calculated as: $p_{t+1} = \lambda\, p_t$ where $p_0 = 1$ and the value of λ is set equal to 0.995. As time t increases, the chances of selecting a random action are reduced. The RL/PI controller, therefore, is able to choose an action a_t and alter the control signal, c, such that the root mean square error between the set point temperature (T_{sp}) and the exit air temperature (T_{ao}) over several episodes is reduced.

The variation of the root mean squared error (RMSE) versus the number of episodes, when only the PI controller is applied to the heating coil and when the RL/PI controller is applied is demonstrated in Figure 4.4. It is concluded from the plot that the RL/PI controller combination is capable of reducing the RMSE by a greater magnitude than the stand-alone PI controller after approximately 600 trials: Whereas, the RMSE remains at a constant value of 0.76 for the stand-alone PI controller, the RMSE has been reduced to 0.556 by the RL/PI controller by the 1000th trial.

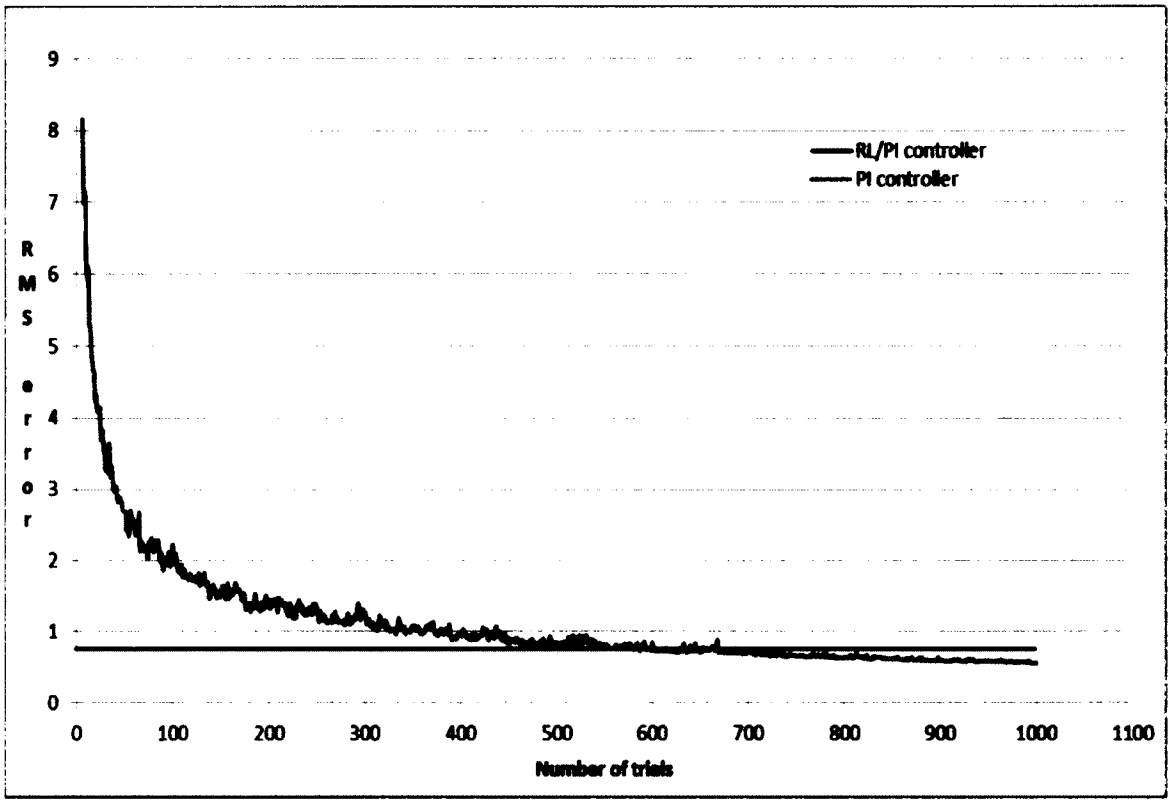

Figure 4.4. Variation of RMS error.

CHAPTER V

A PSO-TRAINED, ELM-BASED RBF NETWORK ENSEMBLE FOR THE PREDICTION OF THE WAVE-EXCITATION FORCE

5.1 Introduction

In order to effectively perform phase control operations on a point absorber, the knowledge of the future wave excitation force is required. This chapter details the development of a time series prediction algorithm based on an ensemble of Radial Basis Function (RBF) networks. The RBF networks have been trained using the Extreme Learning Machine (ELM) algorithm [81] and Particle Swarm Optimization (PSO) [82]. An experimental investigation was conducted to compare the performance of the proposed prediction algorithm with the performance of other single-hidden-layer feedforward neural networks (SLFNs).

The extreme learning machine (ELM) is a fast machine learning algorithm utilized for the training of single-hidden-layer feedforward neural networks (SLFNs) [81, 83]. It was developed as an alternative to gradient-based learning algorithms, e.g., back-propagation, in order to accelerate the training of the network, provide good generalization performance by obtaining the smallest norm of the connection weights, and also obviate the need for time-consuming algorithmic parameter tuning [81]. Various ELM-based algorithms have been proposed over the last few years [84, 85] in an attempt to reduce the typically high number of hidden nodes required by the ELM due to the random determination of the connection weights between input and hidden layer. Furthermore, the ELM has been combined with evolutionary algorithms [86] in order to evolve the network parameters in tandem with the connection weights.

Radial basis function (RBF) networks [87, 88] are a particular type of SLFNs, which has been used extensively for function approximation and time series prediction. RBF networks are universal approximators [88], i.e., given a sufficiently large number of hidden layer nodes they, can be

trained to approximate any real multivariate continuous function on a finite data set. An RBF network utilizes a radial basis kernel in each hidden node in order to obtain accurate local, relative to the kernel center, approximations of the unknown function. The Gaussian and the inverse multiquadric kernels, which are radially symmetric and bounded, are frequently used as basis functions in RBF networks. The output of the network is obtained through a linear combination of the hidden nodes' output.

A comparison between the performance of an ELM-based RBF network and a support vector regression (SVR) algorithm in a very small number of regression problems is presented in [89]. The two methods have comparable performance in terms of approximation accuracy, but the ELM-based RBF network requires a significantly shorter time for training. Given that the kernel centers and basis widths are selected randomly in the aforementioned ELM-based methodology, the algorithmic performance would most likely improve via a less-random selection scheme; however, such a scheme should not mitigate the major advantage of ELMs, i.e., the fast training of the network. Furthermore, as shown in [90], the performance of an RBF network in a number of time series prediction problems strongly depends on the choice of kernel function, number of hidden nodes, and basis width values.

The training of artificial neural networks (ANNs), including RBF networks, using evolutionary algorithms has been an active area of research during the last fifteen years. Evolutionary algorithms have been employed in order to evolve the network connection weights [91-92], the location of the kernel centers of an RBF network [93], and also to evolve basis width values, location of kernel centers, and connection weights simultaneously [94]. The determination of the values of the network connection weights in tandem with the network architecture has also been investigated in [95-97]. Finally, evolutionary multi-objective optimization algorithms have been employed in order to generate ensembles of neural networks and/or learning machines [98-101].

The main advantage of using stochastic evolutionary algorithms for the network training over traditional, gradient-based algorithms is the inherent capability of the former to minimize the risk of getting trapped in locally optimal values during the search/training process. Furthermore, most evolutionary algorithms are population-based, i.e., perform multiple parallel searches during a single run; this enables them to explore different regions of the decision variable space simultaneously and through the utilization of appropriate mechanisms to transmit search-related information across the population. In this work, PSO and the ELM are combined in order to develop an algorithm that generates ensembles of RBF networks. The generalization error of an ensemble of networks/learners is equal to the weighted average of the generalization error of the individual networks minus the ensemble ambiguity [102]; the latter quantifies the diversity within the ensemble. Therefore, the objective when generating such an ensemble is that it comprises a diverse set of accurate learners. The global best (*gbest*) PSO search mechanism [103] attempts to direct each population member towards the global optimal solution vector that has been found up to the current iteration, but also towards the personal best position (solution vector) that has been found by the corresponding population member thus far. In this chapter, it is shown that these two features of the *gbest* search and network training mechanism provide the desirable diverse ensemble of accurate learners. Diversity is preserved via the attraction of each population member towards its current personal best solution and improved prediction accuracy is achieved via its attraction towards the solution with the current minimum validation error. When the stopping criterion of the training process has been met, the current set of personal best solution vectors comprises the ensemble of RBF networks that is utilized to compute the network output. The proposed methodology for training, pruning, and ensembling of RBF networks is presented in Section 5.2. The results of its application to regression and time series prediction benchmark problems and comparisons with other SLFN learners are presented in Section 5.3.

5.2 Training, Pruning, and Ensembling of RBF Networks using PSO and the ELM

5.2.1 ELM-based RBF network

An RBF network is an SLFN with a radial basis function assigned to each hidden node. Therefore, the function to be approximated is represented as an expansion in basis functions, which are modeled using kernel functions. Even though, there are no connection weights between input and hidden layer, the coordinates of the kernel centers need to be determined and, thus, are considered parameters of the network. In this work, the inverse multiquadric kernel is utilized in the following form:

$$\phi(\mathbf{x}) = (\|\mathbf{x} - \bar{\mathbf{x}}\|^2 + \sigma^2)^{-1/2} \tag{5.1}$$

where $\bar{\mathbf{x}}$ is the kernel center coordinate vector, $\mathbf{x}$ is the input vector, and σ is the basis width, or smoothing parameter, which also needs to be determined for each kernel. The RBF network output is computed as the weighted average of the output of the hidden nodes, including the contribution of a bias node. Assuming a network with N hidden layer nodes and a single output node, the value of the approximated function at $\mathbf{x}$ is computed as follows,

$$f(\mathbf{x}) = \sum_{n=1}^{N} w_n \phi_n(\mathbf{x}) + w_0 \tag{5.2}$$

where w_n is the weight of the nth radial basis function in the corresponding hidden node and w_0 is the bias node weight. These $N + 1$ weights are obtained through a supervised learning approach, i.e., the network is trained by adjusting its parameters so that the overall output error is minimized when it is evaluated on a training dataset. The training objective is typically formulated as a minimization of the sum-of-squares problem:

$$\min_{(\sigma_n, \bar{x}_n, w_n)_1^N} \sum_{p=1}^{P} \left(f(\mathbf{x}_p) - y(\mathbf{x}_p)\right)^2 \tag{5.3}$$

where *P* is the number of instances in the training dataset. The optimization problem defined in eq. (5.3) is nonconvex with multiple local minima [105]. Gradient descent can be utilized to obtain a solution for the network weights, the kernel centers, and the basis widths [88]. Given the local-approximator nature of bounded radial basis functions, a clustering algorithm, e.g., *K*-means, can also be employed at the initial phase of the training process to determine the positions of the kernel centers [106]. The ELM algorithm adapted for RBF networks [90] provides a much faster approach: The kernel centers and basis widths are initialized with random values from within a specific range and the problem of determining the weights is then formulated as follows,

$$\sum_{n=1}^{N} w_n \phi_n(\mathbf{x}_p) + w_0 = y(\mathbf{x}_p), \quad p \in \{1, \ldots\ldots, P\} \tag{5.4}$$

This corresponds to a linear system of P equations, which can be written in a compact matrix form as follows,

$$\boldsymbol{Hw} = \boldsymbol{Y} \tag{5.5}$$

The training of the network can then be accomplished by finding a least-squares solution $\hat{\mathbf{w}}$ of eq. (5.5): $\min_{\mathbf{w}} \|\boldsymbol{Hw} - \boldsymbol{Y}\|$. In most practical applications, the number of hidden nodes is much smaller than the size of the training dataset. In this case, eq. (5.5) corresponds to an over determined system of equations and the unique smallest-norm least squares solution is as follows.

$$\hat{\mathbf{w}} = \mathbf{H}^{\dagger}\mathbf{Y} \tag{5.6}$$

where $\mathbf{H}^{\dagger}$ is the Moore-Penrose generalized inverse matrix [107]. This can be computed using a number of methods; in this work this is done using the *singular value decomposition* (SVD) approach. As is pointed out in [90, 108], in general, the smaller the network weights, the better the generalization performance; using the $\mathbf{H}^{\dagger}$ matrix, the smallest hidden-to-output layer weights are obtained.

5.2.2 Particle swarm optimization

The utilization of the ELM for the training of SLFNs results in a significant reduction in the training time compared to gradient-based tuning algorithms. However, as is reported in [86], when the ELM is employed for the training of ANNs, the random selection of the values of the input weights tends to favor networks with a larger number of hidden nodes compared to gradient-based network tuning. In order to address this issue, an evolutionary algorithm can be utilized to evolve the network parameters, as is done in [86] where a differential evolution algorithm is combined with the ELM to train ANNs. In addition to a shorter training time, a more compact network architecture could also result in better generalization performance. These observations are expected to be applicable to other types of SLFNs like RBF networks. In this work, PSO is utilized to evolve both the position of each kernel and the corresponding basis width.

The *gbest* PSO model [109] uses a population of swarm particles (solution vectors) that search for the optimal solution simultaneously and in a cooperative manner. The position vector of each particle $\mathbf{x} \in \mathbb{R}^J$ is updated at each iteration t + 1 using the following scheme $\forall\, j \in \{1, \ldots., J\}$:

$$x_j(t+1) = x_j(t) + v_j(t+1) \tag{5.7}$$

$$v_j(t+1) = \chi(v_j(t) + \phi_1.U_j(0,1).\left(\hat{y}_j(t) - x_j(t)\right) + \phi_2.U_j(0,1).\left(y_j(t) - x_j(t)\right) \tag{5.8}$$

where $x_j(t)$,$v_j(t)$, $x_j(t+1)$ and $v_j(t+1)$ are the particle's j^{th} position coordinate and velocity over a single time increment at iteration t and $t+1$, respectively. ϕ_1 and ϕ_2 are coefficients that adjust the attraction of the particle towards the global best solution that has been found by the swarm thus far, $\hat{\mathbf{y}}(t)$, and towards the best solution that has been found by the particle up to iteration t, $\mathbf{y}(t)$, respectively. $U_j(0,1)$ is a uniformly distributed random number in (0, 1) sampled anew for each j and particle.

In order to prevent the velocity of each particle from increasing uncontrollably when using eq. (5.7), various methods have been proposed over the years; here the concept of the constriction

coefficient [110] is adopted. The constriction coefficient, χ, is computed using the following scheme as shown.

$$\chi = \frac{2k}{\left|2 - \phi - \sqrt{\phi^2 - 4\phi}\right|} \tag{5.9}$$

where $\phi = \phi_1 + \phi_2, \phi > 4, k \in [0,1]$

In this work, k is set equal to one in order to promote a high degree of exploration of the search space, ϕ is set equal to 4.1, as is suggested in [111], and ϕ_1 is set equal to ϕ_2. The condition $\phi >$ 4 is a necessary condition for the convergence of the particle's trajectory to a position inside the search space. This is proven in [110], where the equations of motion are modeled as a discrete-time dynamic system and a stability analysis is performed in order to derive conditions for its convergence to an equilibrium point. Using the *gbest* model, the particle attractor (equilibrium point) corresponds to a weighted average between its personal best and global best positions. In the current application, when the network training has been completed, it is anticipated that the set of personal best positions contains solution vectors close to the global best solution, depending on the size of the attraction basin, which are also distinct enough to satisfy the diversity requirement for the ensemble members.

The positions of the particles are initialized randomly within the range of each coordinate (input variable): $x_j \in \left[x_j^{(L)}, x_j^{(U)}\right], j \in \{1, \ldots \ldots J\}$. The velocities are initialized with zero values. During the iterative search process, when a particle moves to a position outside of the allowable range in coordinate j, its position coordinate j is set equal to the closest boundary value and the corresponding velocity component is set equal to zero. At the end of each iteration, the performance of the swarm particles is assessed by computing the root mean squared error (RMSE) on a validation set, which contains data that are not included in the training dataset. This is done

in order to update, if applicable, the global best and personal best solution vectors. The RBF network parameters that are optimized are the kernel center coordinates and basis widths.

In this research, the PSO algorithm is modified as follows: The particle with the worst (highest) RMSE value at the end of each iteration is replaced by a mutated (perturbed) copy of the global best solution vector. The mutation is performed using the following scheme $j \in \{1, \ldots . J\}$ as shown below.

$$x_j = \begin{cases} \hat{y}_j + msf.\ \left(x_j^{(U)} - x_j^{(L)}\right), & if\ U_j(0,1) < mrt \\ \hat{y}_j \quad , & otherwise \end{cases} \tag{5.10}$$

where *msf* is the mutation scaling factor and *mrt* is the mutation rate. In this way, the optimizer is able to perform a local search in the vicinity of the global best solution found thus far through small perturbations of the corresponding solution vector. During the initialization of the PSO parameters' values for each swarm particle, the input layer of each corresponding RBF network, *i*, is pruned by randomly selecting the input variables that will be included in the network as shown below.

$$x_{ij} = \begin{cases} deactivated, & if\ U_{ij}(0,1) < prr \\ activated \quad , & otherwise \end{cases} \tag{5.11}$$

where *prr* is the pruning rate and $j \in \{1, \ldots . , J\},\ i \in \{1, \ldots \ldots , I\}$.

The main reason for pruning the input layer is to remove variables that do not contribute towards a better understanding of the underlying process that produced the dataset and, thus, their inclusion does not cause a substantial increase in the accuracy of the approximation/prediction model. In the proposed approach, the importance of the input variables is not estimated explicitly; the determination of the optimal input layer architecture is done gradually through the aforementioned particle replacement operation as, at each iteration, the network with the worst performance is discarded and replaced by a network with the optimal input layer architecture that has been found thus far.

5.2.3 Implementation of the proposed algorithm for training and ensembling of RBF networks

The PSO algorithm described in the previous section is utilized for the training of the ELM-based RBF networks. The training of the ELM-based RBF networks is stopped if either the global optimal solution has not changed after I_{ch} iterations or the algorithm has reached the maximum allowable number of iterations, I_{max}. Two distinct sets of data points are used during the training process; the first corresponds to the training data set, which is used to compute the network weights via Singular Value Decomposition (SVD). The particles (solution vectors) are then evaluated on a validation set in order to find global and personal best positions. In this way, the risk of overtraining the network is reduced. The global best position corresponds to the network with the smallest prediction error on the validation set. The prediction error is quantified by computing the root mean squared error (RMSE). The training and validation data sets, both input and output values, are normalized in the range [-1.0, 1.0].

The ensembling process commences immediately after the training of the RBF networks has been finalized. The output of the ensemble is obtained by averaging the output of its members, i.e., the personal best solutions of the swarm particles. Prior to the evaluation of the generalization performance of the ensemble on a testing dataset, the existence of outliers among the ensemble members is investigated by applying Chauvenet's criterion [112]. This criterion specifies that all points that fall within a band around the mean that corresponds to a probability of $[1 - 1/(2E)]$ should be retained. E is the original size of the ensemble and, thus, is equal to the swarm population size. The criterion is applied only once for each point of the testing dataset. Using Gaussian probabilities, the ratio of maximum acceptable deviation to sample standard deviation is computed and utilized for the detection of outliers [113]. The algorithm has been developed in FORTRAN 95 (Appendix I). The training and testing processes of the PSO-trained ELM-based RBF network ensemble are outlined in the figure 5.1.

```
Specify the RBF network architecture
Initialize the swarm population particles (each particle corresponds to an RBF network)
Iter = 0
do
   Compute the connection weights of each RBF network using the training data set and SVD
   Evaluate each RBF network on the validation data set by computing the RMSE
   Find the global best RBF network up to the currect iteration
   Update, if applicable, the personal best position of each particle
   Move each particle to a new position inside the search space using the gbest PSO algorithm
   Iter = Iter + 1
until stopping criterion is satisfied
Form RBF network ensemble by combining the personal best positions of the swarm particles
Apply Chauvenet's criterion while computing the ensemble prediction on the testing data set
```

Figure 5.1. Pseudo-code of training and testing process of the PSO-trained ELM-based RBF network ensemble.

5.3 Experimental Investigation

The generalization performance of the RBF networks trained using the proposed methodology is investigated and the results are presented in this section. In all the experiments, the swarm population size, I, is set equal to 20 and I_{ch} and I_{max} are set equal to 8 and 50, respectively. In the first part of this investigation, the number of hidden nodes is set equal to 10 in order to observe the algorithmic effectiveness and efficiency using a small-sized network. The coordinates of the kernel centers are allowed to vary within the range [-1.0, 1.0], while the basis width values within the range [1.0, 60.0]. The mutation parameters, *msf* and *mrt*, are set equal to 0.2 and 0.5, respectively, and the pruning rate, *prr*, is set equal to 0.2. The training and validation datasets are normalized in the range [-1.0, 1.0].

Ten widely-utilized benchmark problems are considered: Eight regression and two time series prediction problems. The datasets of the majority of these problems have been obtained from the UCI machine learning repository [114]. The problem features and additional references are provided in Table 5.1.

ID	Problem description	Number of data points	Number of inputs	Input types
BNK	Bank queues simulation[1]	8192	8	integer, real
FF	Forest fires [116]	517	4	real
BH	Housing values in Boston	506	13	categorical, integer, real
CCS	Concrete compressive strength [117]	1030	8	real
SRV	Servomechanism	167	4	categorical, integer
CS	Concrete slump test [118]	103	7	real
CH	Computer hardware performance	209	7	integer
WBP	Breast Cancer Wisconsin (Prognostic)	198	32	real
BJ	Box-Jenkins time series [119]	290	10	real
MG	Mackey-Glass time series [120]	4898	11	real

Table 5.1. Features of regression and time series prediction benchmark problems.

The dataset of each problem is first randomized and then split into three groups: 40% of the data are used for training, 10% for validation, and 50% for testing. Fifty independent runs are performed for each problem. The RMSE and the mean absolute error (MAE) of the predictions on the testing set are computed using the network output, after it has been transformed back to its original scale, and recorded for the ensemble and for the RBF network with the lowest RMSE value on the validation set. The same 10 problems are used in all phases of this investigation. The computational cost of obtaining the ensemble predictions is negligible compared to the

[1] http://www.cs.toronto.edu/~delve/data/datasets.html (last accessed on 7/25/2015)

corresponding cost of the training process; on average, the time used to compute the ensemble predictions is equal to 0.7% of the time required for the training process on a machine with 16 GB of RAM and a quad-core 2.80 GHz processor running on a 64-bit Linux operating system.

5.3.1 Effectiveness of the proposed ensembling methodology

In the first part, the effectiveness of the proposed methodology is tested, and in particular the utilization of the mutation operator combined with the pruning of the input layer. The RMSE and the mean absolute error (MAE) of the predictions are computed on the testing dataset using the network output, after the latter has been transformed back to its original scale, and recorded for the ensemble (ENS) and for the global best RBF network (GB), i.e., the network with the lowest RMSE value on the validation set at the end of each run. The corresponding versions without mutation and pruning are denoted by ENS_NMP and GB_NMP, respectively. The lower the RMSE and the MAE values, the better the algorithmic performance.

In all cases, a single hidden layer with 10 nodes is utilized and the maximum number of training iterations per run is set equal to 1000. A pairwise comparison between ENS and ENS_NMP to determine the statistical significance of the results is also performed using the two-tailed p-values, which have been computed using the t-test for unequal variances. In the problems where an algorithm has statistically better performance than the other at the 0.05 significance level, the mean value of its RMSE is highlighted in bold font. The results are shown in Table 5.2.

The results reported in Table 5.2 demonstrate the effectiveness of mutation and input-layer pruning on the algorithmic performance: ENS outperforms ENS_NMP in all 10 problems and in both metrics; the difference in the mean values is statistically significant at the 0.05 level in 7 problems using either metric. Furthermore, the generalization performance of the ensemble (ENS) is clearly better than the performance of the global best network (GB) in both metrics when mutation and input-layer pruning are incorporated into the algorithm; the same conclusion

cannot be drawn from a generalization performance comparison between GB_NMP and ENS_NMP, which further corroborates the claim that mutation and pruning enhance the PSO-training and ensembling effectiveness.

ID	RMSE & MAE	ENS	GB	ENS_NMP	GB_NMP
BNK	RMSE	**7.209**$\cdot 10^{-2}$	7.254$\cdot 10^{-2}$	8.721$\cdot 10^{-2}$	8.725$\cdot 10^{-2}$
	MAE	**5.457**$\cdot 10^{-2}$	5.497$\cdot 10^{-2}$	6.797$\cdot 10^{-2}$	6.793$\cdot 10^{-2}$
FF	RMSE	1.338	1.340	13.341	1.340
	MAE	**1.067**	1.069	1.096	1.092
BH	RMSE	**4.436**	4.601	4.986	4.893
	MAE	**3.411**	3.545	3.897	3.820
CCS	RMSE	**1.281**$\cdot 10^{1}$	1.368$\cdot 10^{1}$	1.531$\cdot 10^{1}$	1.536$\cdot 10^{1}$
	MAE	**1.006**$\cdot 10^{1}$	1.055$\cdot 10^{1}$	1.258$\cdot 10^{1}$	1.247$\cdot 10^{1}$
SRV	RMSE	**9.675**$\cdot 10^{-1}$	1.038	9.973$\cdot 10^{-1}$	1.002
	MAE	**5.442**$\cdot 10^{-1}$	5.941$\cdot 10^{-1}$	6.200$\cdot 10^{-1}$	6.156$\cdot 10^{-1}$
CS	RMSE	8.133	9.139	8.295	9.764
	MAE	6.612	7.253	6.728	7.781
CH	RMSE	1.265$\cdot 10^{1}$	1.474$\cdot 10^{1}$	1.311$\cdot 10^{1}$	1.617$\cdot 10^{1}$
	MAE	5.581	6.338	5.801	6.967
WBP	RMSE	**3.546**$\cdot 10^{1}$	3.832$\cdot 10^{1}$	4.160$\cdot 10^{1}$	4.237$\cdot 10^{1}$
	MAE	**2.953**$\cdot 10^{1}$	3.198$\cdot 10^{1}$	3.497$\cdot 10^{1}$	3.546$\cdot 10^{1}$
BJ	RMSE	**4.324**$\cdot 10^{-1}$	4.437$\cdot 10^{-1}$	4.414$\cdot 10^{-1}$	4.559$\cdot 10^{-1}$
	MAE	3.095$\cdot 10^{-1}$	3.171$\cdot 10^{-1}$	3.128$\cdot 10^{-1}$	3.225$\cdot 10^{-1}$
MG	RMSE	**1.187**$\cdot 10^{-2}$	1.276$\cdot 10^{-2}$	2.165$\cdot 10^{-2}$	2.144$\cdot 10^{-2}$
	MAE	**1.027**$\cdot 10^{-2}$	1.034$\cdot 10^{-2}$	1.783$\cdot 10^{-2}$	1.759$\cdot 10^{-2}$

Table 5.2. RMSE and MAE results for ENS, GB, ENS_NMP and GB_NMP.

In the next part, the performance of the ensemble (ENS) and of the global best (GB) of the PSO-ELM-trained RBF networks is compared with the performance of two other SLFN learners: an artificial neural network (ANN) that uses the back propagation algorithm for training and an RBF network that uses *K*-means clustering (RBF_K) to obtain the kernel parameters and linear regression to compute the network weights. Both algorithms are available in the open source data mining software WEKA [122]. The ANN uses a momentum term with value set equal to 0.2 and a

learning rate with value set equal to 0.3. Both SLFN learners use a single hidden layer with 10 nodes; the number of training iterations is set equal to 1000.

ID	Mean & Deviation	RBF_K	ANN	GB	ENS
BNK	Mean	$(1.420 \cdot 10^{-1})^*$	$(8.130 \cdot 10^{-2})^*$	$7.254 \cdot 10^{-2}$	$\mathbf{7.209} \cdot 10^{-2}$
	Deviation	$1.484 \cdot 10^{-4}$	$1.276 \cdot 10^{-2}$	$2.640 \cdot 10^{-4}$	$3.545 \cdot 10^{-4}$
FF	Mean	$(1.359)^*$	$(1.461)^*$	1.340	1.338
	Deviation	$1.391 \cdot 10^{-2}$	$1.326 \cdot 10^{-1}$	$2.500 \cdot 10^{-2}$	$2.562 \cdot 10^{-2}$
BH	Mean	$(7.505)^*$	$(5.455)^*$	4.601	**4.436**
	Deviation	$2.919 \cdot 10^{-1}$	1.089	$4.694 \cdot 10^{-1}$	$2.954 \cdot 10^{-1}$
CCS	Mean	$(1.844 \cdot 10^{1})^*$	$(1.727 \cdot 10^{1})^*$	$1.368 \cdot 10^{1}$	$\mathbf{1.281} \cdot 10^{1}$
	Deviation	1.870	3.071	2.052	1.969
SRV	Mean	$(1.524)^*$	1.014	1.038	$\mathbf{9.675} \cdot 10^{-1}$
	Deviation	$7.097 \cdot 10^{-2}$	$2.278 \cdot 10^{-1}$	$6.677 \cdot 10^{-2}$	$4.355 \cdot 10^{-2}$
CS	Mean	$(1.169 \cdot 10^{1})^*$	$(8.715)^*$	9.139	**8.133**
	Deviation	9.547	1.381	1.085	$9.001 \cdot 10^{-1}$
CH	Mean	$(1.261 \cdot 10^{2})^*$	$1.380 \cdot 10^{1}$	$1.474 \cdot 10^{1}$	$\mathbf{1.265} \cdot 10^{1}$
	Deviation	$3.996 \cdot 10^{1}$	$1.271 \cdot 10^{1}$	6.197	3.342
WBP	Mean	$(3.835 \cdot 10^{1})^*$	$(4.172 \cdot 10^{1})^*$	$3.832 \cdot 10^{1}$	$\mathbf{3.546} \cdot 10^{1}$
	Deviation	1.222	9.467	2.114	$5.716 \cdot 10^{-1}$
BJ	Mean	$(1.364)^*$	$(5.893 \cdot 10^{-1})^*$	$4.437 \cdot 10^{-1}$	$\mathbf{4.324} \cdot 10^{-1}$
	Deviation	$1.102 \cdot 10^{-1}$	$1.913 \cdot 10^{-1}$	$2.878 \cdot 10^{-2}$	$2.236 \cdot 10^{-2}$
MG	Mean	$(8.180 \cdot 10^{-2})^*$	$1.068 \cdot 10^{-2}$	$1.276 \cdot 10^{-2}$	$1.187 \cdot 10^{-2}$
	Deviation	$5.506 \cdot 10^{-3}$	$3.257 \cdot 10^{-3}$	$3.624 \cdot 10^{-3}$	$2.809 \cdot 10^{-3}$

Table 5.3. Mean and standard deviation values of RMSE for RBF_K, ANN, GB and ENS.

The computed mean (Mean) and standard deviation (Deviation) values of RMSE are listed in Table 5.3. Pairwise comparisons between ENS, RBF_K, and ANN are performed in order to determine the statistical significance of the results. If the performance of ENS in a problem is statistically better than the performance of another algorithm, then there is an asterisk (*) next to the other algorithm's corresponding mean RMSE value. If the difference in performance between ENS and GB is statistically significant at the 0.05 level, the mean value of the more accurate algorithm is highlighted in bold font.

The RMSE results displayed in Table 5.3 reveal that the PSO-ELM-trained RBF network ensemble has better generalization performance than the RBF_K learner in 10 problems, a result that is statistically significant in all 10 problems, and in 9 problems compared to the ANN, a result that is statistically significant in 7 problems. Furthermore, the variance in the ENS results is very small compared to the other two SLFN learners. In none of the 10 problems the performance of either ANN or RBF_K is statistically better than the performance of ENS. A comparison between the results of GB and ENS shows that the latter performs better in all 10 problems, a result that is statistically significant in 8 problems. Overall, these results demonstrate that the PSO-trained ELM-based RBF network ensembling methodology has very good generalization performance even when applied to a small-sized network. The proposed PSO-ELM-based training methodology without the ensembling is also successful as GB has a lower mean RMSE value than the RBF_K and the ANN in 10 and 6 problems, respectively.

5.3.2 RBF networks with optimal number of hidden layer nodes

In this section, the number of hidden layer nodes is varied in an attempt to optimize the network size. Starting with 2 hidden nodes, the number is increased manually in steps of 1 node to a maximum number of 20 nodes. The network size of the ensemble (ENS_OPT) that produces the lowest mean RMSE value in each problem is (following the sequence used in Table 5.1): {20, 11, 5, 12, 20, 12, 20, 18, 20, 20}. The corresponding mean RMSE values are shown in Table 5.4.

The results obtained using the IB5 k-nearest neighbor algorithm [123], a Gaussian process (GP) learner, and M5P [124], a tree-based method with pruning, are also listed in Table 5.4. GP uses the Gaussian kernel function with a basis width that is varied manually from within the following set of discrete values: {0.25, 0.5, 1.0, 1.5, 2.0, 3.0, 5.0, 10.0}. The results that correspond to the basis width value that produces the lowest mean RMSE in each problem are shown in Table 5.4. The corresponding basis width values are: {1.0, 1.0, 1.5, 1.0, 0.5, 5.0, 1.5, 3.0, 2.0, 10.0}. The data

mining software WEKA was utilized to generate the results for IB5, GP, and M5P. The lowest mean RMSE and MAE values in each problem are highlighted in bold font in Table 5.4.

The generalization performance of the proposed methodology is significantly improved by using an optimal-sized hidden layer as is observed through a comparison between the results of ENS listed in Table 5.2 and the results of ENS_OPT listed in Table 5.4. A comparison between the results of the GP and the IB5 learners and the results of ENS_OPT reveals that the latter outperforms both learners in all 10 problems using either metric. It also outperforms M5P in 9 problems using the RMSE metric and in 8 problems using the MAE metric.

ID	RMSE & MAE	GP	IB5	M5P	ENS_OPT
BNK	RMSE	$7.251 \cdot 10^{-2}$	$1.155 \cdot 10^{-1}$	$7.090 \cdot 10^{-2}$	$\mathbf{7.085} \cdot 10^{-2}$
	MAE	$5.491 \cdot 10^{-2}$	$8.940 \cdot 10^{-2}$	$\mathbf{5.322} \cdot 10^{-2}$	$5.331 \cdot 10^{-2}$
FF	RMSE	1.345	1.443	1.352	**1.336**
	MAE	1.060	1.095	1.124	**1.058**
BH	RMSE	4.715	6.615	**3.776**	4.139
	MAE	3.180	4.602	**2.797**	3.152
CCS	RMSE	$1.317 \cdot 10^{1}$	$1.743 \cdot 10^{1}$	$1.308 \cdot 10^{1}$	$\mathbf{1.264} \cdot 10^{1}$
	MAE	$1.094 \cdot 10^{1}$	$1.410 \cdot 10^{1}$	$1.036 \cdot 10^{1}$	**9.972**
SRV	RMSE	1.061	1.098	$9.261 \cdot 10^{-1}$	$\mathbf{9.030} \cdot 10^{-1}$
	MAE	$5.514 \cdot 10^{-1}$	$5.644 \cdot 10^{-1}$	$4.611 \cdot 10^{-1}$	$\mathbf{4.350} \cdot 10^{-1}$
CS	RMSE	8.218	8.519	8.194	**8.073**
	MAE	6.401	6.625	6.409	**6.395**
CH	RMSE	$4.328 \cdot 10^{1}$	$5.904 \cdot 10^{1}$	$3.189 \cdot 10^{1}$	**9.121**
	MAE	$1.678 \cdot 10^{1}$	$1.953 \cdot 10^{1}$	$1.476 \cdot 10^{1}$	**4.385**
WBP	RMSE	$3.664 \cdot 10^{1}$	$3.965 \cdot 10^{1}$	$3.549 \cdot 10^{1}$	$\mathbf{3.404} \cdot 10^{1}$
	MAE	$3.116 \cdot 10^{1}$	$3.291 \cdot 10^{1}$	$2.877 \cdot 10^{1}$	$\mathbf{2.770} \cdot 10^{1}$
BJ	RMSE	1.003	1.074	$4.521 \cdot 10^{-1}$	$\mathbf{3.915} \cdot 10^{-1}$
	MAE	$7.001 \cdot 10^{-1}$	$7.899 \cdot 10^{-1}$	$3.213 \cdot 10^{-1}$	$\mathbf{2.867} \cdot 10^{-1}$
MG	RMSE	$1.540 \cdot 10^{-2}$	$1.071 \cdot 10^{-2}$	$3.612 \cdot 10^{-2}$	$\mathbf{7.238} \cdot 10^{-3}$
	MAE	$1.180 \cdot 10^{-2}$	$8.700 \cdot 10^{-3}$	$2.860 \cdot 10^{-2}$	$\mathbf{5.758} \cdot 10^{-3}$

Table 5.4. RMSE and MAE results for GP, IB5, M5P and ENS_OPT.

CHAPTER VI

SIMULATION RESULTS FOR REGULAR WAVES

6.1 Introduction

The WEC system described in Chapter III is simulated in MATLAB®. In this way, the response of the point absorber to regular waves, with and without phase control, is computed. Subsequently, the mean generated power of the point absorber WEC system, the corresponding efficiency, relative capture width, and maximum and minimum amplitude of the point absorber are computed and tabulated. The first half of the simulation is excluded from the computations due to the transient character of the response of the heaving point absorber.

6.2 Definition of Evaluation Criteria

The output of the numerical simulations in regular waves with and without phase control is evaluated using the following criteria:

a) Mean generated power (P_{mg}): The mean of the values of the generated power in the second half of the simulation.

b) Power absorption efficiency (η_{pa}): Ratio of mean generated power (P_{mg}) to available power (P_{av}),

$$\eta_{pa} = \frac{P_{mg}}{P_{av}} \tag{6.1}$$

The available power (P_{av}) of an incident wave front is the power of the wave front whose width is equal to the diameter (D) of the point absorber.

c) Maximum amplitude (A_{max}): The absolute value of the maximum distance attained by the heaving point absorber measured from the equilibrium position and along the vertical axis during the second half of the simulation.

6.3 Settings for the Point Absorber WEC System

The point absorber WEC system consists of numerous components whose physical properties must be initialized prior to performing the simulations. The values of key physical properties and constants of the WEC system used in the simulations are listed in Table 6.1.

Component	Notation	Units	Value
Radius of the point absorber	*r*	m	4
Piston surface area	*sp*	m^2	0.05
Density of oil in the hydraulic cylinder	*rho_o*	kg/m^3	850
Ratio of specific heats (gamma) for nitrogen	*γ*	-	1.4
Volume of gas in compressibility accumulator (c)	*vca1*	m^3	0.05
Volume of gas in compressibility accumulator (d)	vca2	m^3	0.05
Volume of gas in phase control accumulator (e)	*vpc1*	m^3	0.5
Volume of gas in phase control accumulator (f)	*vpc2*	m^3	0.5
Volume of gas in HP accumulator (g)	*v_hp*	m^3	2
Volume of gas in LP accumulator (h)	*v_lp*	m^3	1
Gas pressure in HP accumulator (g)	*p_hp*	Pa	10^7
Gas pressure in LP accumulator (h)	*p_lp*	Pa	10^7
Gas pressure in compressibility accumulator (c)	*pca1*	Pa	10^7
Gas pressure in compressibility accumulator (d)	*pca2*	Pa	10^7
Gas pressure in phase control accumulator (e)	*ppc1*	Pa	10^7
Gas pressure in phase control accumulator (f)	*ppc2*	Pa	10^7
Maximum continuous speed of the hydraulic motor	*speed_max*	rev/min	3000
Maximum volumetric displacement of the hydraulic motor	*max_dhm*	m^3/rev	$165 \cdot 10^{-6}$
Maximum output torque of the hydraulic motor	*torqm_max*	N·m	659
Control valve discharge coefficient for compressibility accumulators	C_v	-	0.95
Control valve discharge coefficient for phase control accumulators	C_c	-	0.95
Cross sectional area of the control valve to the phase control accumulators	A_c	m^2	0.002
Cross sectional area of the control valve to the compressibility, HP and LP accumulators	A_v	m^2	0.002
Combined rotational inertia of motor-generator-shaft	*Jr*	$kg \cdot s^2$	7.5

Table 6.1. Initial values and constants for components of the point absorber WEC system.

The pressure and volume changes of the gas in the accumulators are assumed to follow an isentropic process. The rotational speed of the motor is assumed to be fixed. Also, the generator torque is assumed to match the hydraulic motor torque.

6.4 Calculation of Available Power in Regular Waves

The available power in a regular wave is the maximum power that can be extracted from the wave using a point absorber of known diameter. The available power for a point absorber, P_{av}, which depends on wave amplitude and wave frequency [35], corresponds to the product of the wave power per meter of the incident wave crest and the diameter of the point absorber. The formula to compute available power for in regular waves is as follows,

$$P_{av} = \frac{D\,\rho\,g^2 T\,H^2}{32\,\pi} \tag{6.2}$$

where D is the diameter of the point absorber, ρ is the density of sea water, g is the acceleration of gravity, T is the wave period, and H is the wave height. The wave height is equal to twice the absolute value of the wave amplitude, A. The available power for various combinations of wave period and amplitude is listed in Table 6.2 and plotted in Figure 6.1.

Wave period, T (s)	P_{av} (kW) - A = 0.5 m	P_{av} (kW) - A = 1.0 m	P_{av} (kW) - A = 1.5 m
5	39.3	157.0	353.2
6	47.1	188.4	423.9
7	55.0	219.8	494.5
8	62.8	251.2	565.2
9	70.7	282.6	635.8
10	78.5	314.0	706.5
11	86.4	345.4	777.1
12	94.2	376.8	847.8
13	102.1	408.2	918.4

Table 6.2. Values of available power for various wave periods and amplitudes.

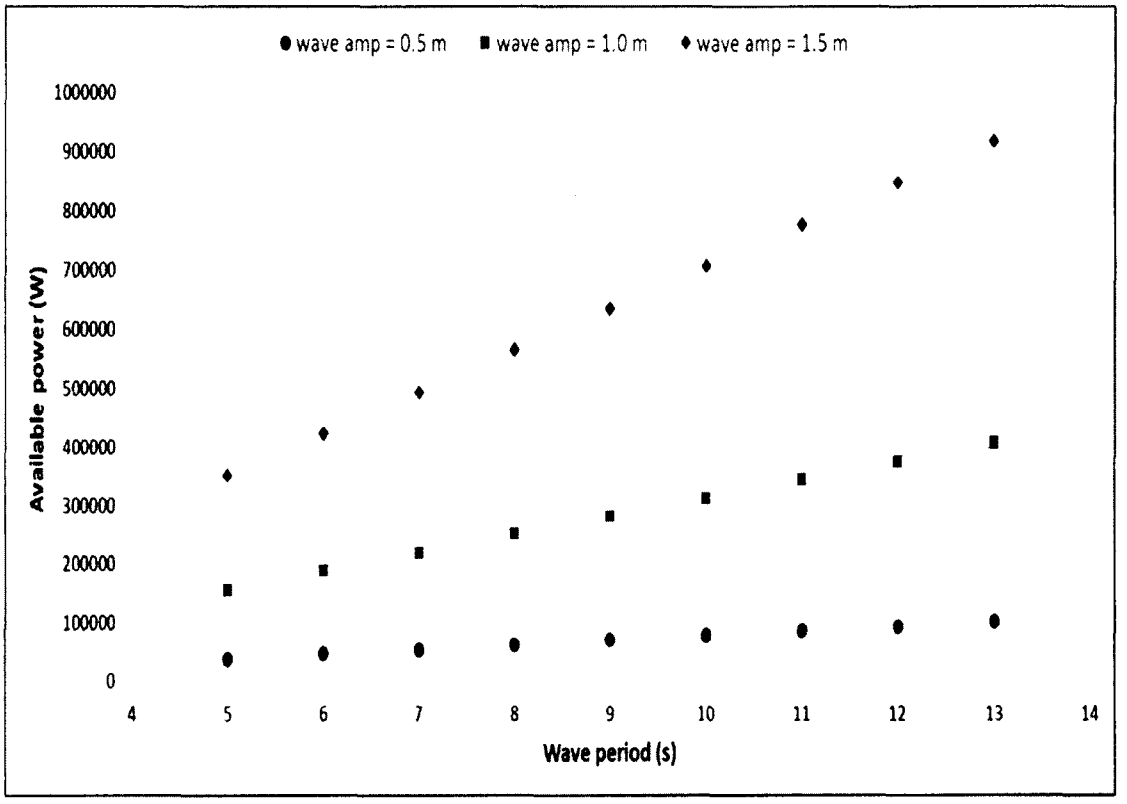

Figure 6.1. Variation of available power in regular waves.

6.5 Simulation of the WEC System Operation in Regular Waves

The performance of the point absorber WEC system is evaluated in all the combinations of wave period and amplitude listed in Table 6.2. When phase control is utilized, the valve of the phase control accumulator is set to open (T_0/C_{coe}) seconds before the peak of the excitation force, where T_0 is the undamped and uncoupled heave natural period of the point absorber. Therefore, the values of the control coefficient C_{coe} correspond to different fractions of T_0. The following values are utilized in this parametric investigation: $C_{coe} = \{4,\ 7,\ 10,\ 15\}$.

The undamped and uncoupled heave natural period is computed from the following equation:

$$T_0 = 2\pi\sqrt{\frac{m_b + m_a}{k_{hs}}} \tag{6.3}$$

where m_b is the mass of the point absorber, m_a is the added mass at wave frequency ω, which is calculated using the piecewise cubic Hermite polynomial (see Appendix E), and k_{hs} is the hydrostatic stiffness of the buoy. The equations for the calculation of m_b and k_{hs} for a spherical point absorber are provided in the nomenclature list of Eq. (3.1). For a point absorber radius of 4 m, T_0 varies monotonically in the range from 4.04 to 4.47 seconds for the wave period values listed in Table 6.2. All the simulations are conducted for a simulated time of 500 seconds with a time step of 0.04 seconds. The motor displacement is kept at its maximum value, i.e., f_{dc} = 1.00.

6.5.1 Results for wave amplitude of 0.5 m

Regular waves with various periods but with a constant wave amplitude of 0.5 m are considered. The mean generated power of the point absorber without phase control (NPC) and with phase control (for each C_{coe} value) is listed in Table 6.3. The corresponding power absorption efficiency is reported in Table 6.4.

Wave period, T (s)	**P_{mg} (kW) (NPC)**	**P_{mg} (kW) ($C_{coe} = 4$)**	**P_{mg} (kW) ($C_{coe} = 7$)**	**P_{mg} (kW) ($C_{coe} = 10$)**	**P_{mg} (kW) ($C_{coe} = 15$)**
5	11.9	8.53	18.2	20.1	**20.2**
6	12.8	13.1	18.2	**20.3**	20.0
7	13.3	10.6	17.9	18.5	**19.7**
8	13.3	10.0	15.9	17.0	**17.2**
9	13.1	8.08	12.8	14.2	**15.2**
10	12.1	4.95	9.77	11.5	**12.5**
11	6.96	2.05	6.97	**6.98**	6.96
12	1.97	1.90	2.02	2.05	**2.06**
13	1.82	1.71	1.86	1.89	**1.97**

Table 6.3. Mean generated power as a function of wave period for A = 0.5 m.

The highest value of the mean generated power for each wave period is highlighted in bold font. It becomes quite clear based on the results listed in Table 6.3 that phase control can have a significant impact on the power absorption of the WEC system for a wide range of wave periods.

Wave period, T (s)	**η_{pa} (%) (NPC)**	**η_{pa} (%) ($C_{coe} = 4$)**	**η_{pa} (%) ($C_{coe} = 7$)**	**η_{pa} (%) ($C_{coe} = 10$)**	**η_{pa} (%) ($C_{coe} = 15$)**
5	30.3	21.7	46.4	51.0	**51.4**
6	27.3	27.9	38.6	**43.2**	42.5
7	24.1	19.3	32.6	33.7	**35.8**
8	21.2	16.0	25.3	27.1	**27.4**
9	18.5	11.4	18.1	20.1	**21.5**
10	15.4	6.31	12.5	14.7	**15.9**
11	8.05	2.38	8.07	**8.08**	8.06
12	2.09	2.01	2.14	2.17	**2.18**
13	1.78	1.67	1.82	1.85	**1.92**

Table 6.4. Power absorption efficiency as a function of wave period for A = 0.5 m.

Furthermore, opening the control valve later, i.e., at an instant closer to the wave peak, seems to work best for almost all wave periods at a fairly small wave amplitude.

The power absorption efficiency is quite high for wave periods near the natural heave period of the point absorber and they decrease monotonically with increasing wave period. Values greater than 50% are observed with phase control. The absolute value of the maximum motion amplitude of the point absorber for each test case is provided in Table 6.5. The lowest value for each wave period is highlighted in bold font.

Wave period, T (s)	A_{max} (m) (NPC)	A_{max} (m) ($C_{coe} = 4$)	A_{max} (m) ($C_{coe} = 7$)	A_{max} (m) ($C_{coe} = 10$)	A_{max} (m) ($C_{coe} = 15$)
5	**0.258**	0.698	0.677	0.637	0.568
6	**0.308**	0.651	0.613	0.563	0.530
7	**0.350**	0.591	0.578	0.554	0.523
8	**0.390**	0.571	0.569	0.542	0.518
9	**0.429**	0.559	0.543	0.526	0.524
10	**0.469**	0.521	0.529	0.514	0.505
11	**0.487**	0.501	0.488	0.488	**0.487**
12	0.486	0.505	0.480	**0.477**	0.485
13	**0.477**	0.506	0.487	0.481	0.479

Table 6.5. Maximum motion amplitude as a function of wave period for A = 0.5 m.

Phase control increases the motion amplitude compared to the no-phase-control case for wave periods less than 10 seconds. Overall, the difference diminishes as the wave period increases. When utilizing phase control, the motion amplitude is lower for the cases when the valve is open later, and thus, it seems that there is no trade-off between minimizing the motion amplitude while maximizing the mean generated power.

6.5.2 Results for wave amplitude of 1.0 m

Similar to the previous case, but with a constant wave amplitude of 1.0 m, regular waves with various periods are considered. The mean generated power of the point absorber with and without phase control is listed in Table 6.6.

Wave period, T (s)	P_{mg} (kW) (NPC)	P_{mg} (kW) ($C_{coe} = 4$)	P_{mg} (kW) ($C_{coe} = 7$)	P_{mg} (kW) ($C_{coe} = 10$)	P_{mg} (kW) ($C_{coe} = 15$)
5	26.1	32.1	56.1	**59.7**	58.5
6	29.5	59.5	**72.8**	72.0	71.5
7	32.6	71.0	**79.8**	78.2	75.1
8	35.8	74.7	**81.2**	78.6	75.3
9	40.1	74.4	**78.9**	77.0	74.3
10	43.1	70.3	**75.7**	74.7	72.4
11	40.8	67.4	**72.5**	72.4	70.7
12	37.9	68.8	**74.2**	73.6	72.4
13	35.6	75.1	**79.8**	79.3	77.9

Table 6.6. Mean generated power as a function of wave period for A = 1.0 m.

For a wave period of 5 seconds, the highest value of mean generated power is attained when the control coefficient is equal to 10. For all the other wave periods, the highest value of mean generated power is attained when the control coefficient is equal to 7. It can be easily observed that phase control has a significant impact on the power absorption of the WEC system, but contrary to the 0.5-m-amplitude case (see Table 6.3), all the control coefficients and for all wave periods provide a substantial increase in the mean generated power compared to NPC. In contrast to what is observed for a smaller wave amplitude, opening the control valve earlier, i.e., $C_{coe} = 7$, seems to have a small advantage over the $C_{coe} = 10$ and the $C_{coe} = 15$ cases. Furthermore, with a wave amplitude of 1.0 m, the mean generated power is not a monotonic function of the wave period.

The corresponding power absorption efficiency is reported in Table 6.7. The efficiency is quite high for wave periods near the natural heave period of the point absorber but, in this case, it attains its maximum value for a wave period of 6 seconds. In the 1.0-m-amplitude case, the efficiency attains lower values up to a wave period of 7 seconds compared to the 0.5-m-amplitude case, and it does not fall for longer wave periods as steeply as it does in the latter.

Wave period, T (s)	η_{pa} (%) (NPC)	η_{pa} (%) ($C_{coe} = 4$)	η_{pa} (%) ($C_{coe} = 7$)	η_{pa} (%) ($C_{coe} = 10$)	η_{pa} (%) ($C_{coe} = 15$)
5	16.6	20.4	35.8	**38.0**	37.3
6	15.7	31.6	**38.6**	38.2	37.9
7	14.8	32.3	**36.3**	35.6	34.2
8	14.2	29.7	**32.3**	31.3	30.0
9	14.2	26.3	**27.9**	27.3	26.3
10	13.7	22.4	**24.1**	23.8	23.1
11	11.8	19.5	**21.0**	20.9	20.5
12	10.1	18.3	**19.7**	19.5	19.2
13	8.72	18.4	**19.6**	19.4	19.1

Table 6.7. Power absorption efficiency as a function of wave period for A = 1.0 m.

The absolute value of the maximum motion amplitude of the point absorber for each test case is provided in Table 6.8.

Wave period, T (s)	A_{max} (m) (NPC)	A_{max} (m) ($C_{coe} = 4$)	A_{max} (m) ($C_{coe} = 7$)	A_{max} (m) ($C_{coe} = 10$)	A_{max} (m) ($C_{coe} = 15$)
5	**0.328**	1.29	1.16	1.06	0.912
6	**0.390**	1.26	1.12	1.01	0.931
7	**0.444**	1.34	1.19	1.10	0.999
8	**0.501**	1.42	1.28	1.16	1.09
9	**0.568**	1.51	1.37	1.26	1.18
10	**0.626**	1.58	1.46	1.36	1.26
11	**0.654**	1.63	1.52	1.45	1.35
12	**0.682**	1.67	1.58	1.52	1.44
13	**0.709**	1.60	1.52	1.49	1.43

Table 6.8. Maximum motion amplitude as a function of wave period for A = 1.0 m.

Phase control increases the motion amplitude significantly compared to the no-phase-control case for any wave period listed in Table 6.8. This difference remains significant even for long wave

periods, in contrast to what is observed in Table 6.5 for a smaller wave amplitude. In addition to this, when utilizing phase control, the motion amplitude is lower for the cases when the valve is open later, however, in this case, there is a trade-off between minimizing the motion amplitude, with $C_{coe} = 15$, and maximizing the mean generated power, with $C_{coe} = 7$.

6.5.3 Results for wave amplitude of 1.5 m

The mean generated power of the point absorber with and without phase control is listed in Table 6.9 for a number of wave periods with a constant wave amplitude of 1.5 m.

Wave period, T (s)	P_{mg} (kW) (NPC)	P_{mg} (kW) ($C_{coe} = 4$)	P_{mg} (kW) ($C_{coe} = 7$)	P_{mg} (kW) ($C_{coe} = 10$)	P_{mg} (kW) ($C_{coe} = 15$)
5	40.7	56.5	97.2	103.3	**106.6**
6	46.4	117.6	139.3	**139.6**	132.5
7	51.4	153.8	**164.3**	156.1	146.7
8	56.6	159.5	**170.9**	164.3	156.9
9	64.3	154.2	**166.6**	164.1	159.1
10	67.3	140.9	**151.3**	150.2	147.9
11	66.6	146.3	**161.1**	159.5	154.3
12	65.6	163.8	**171.2**	170.7	166.0
13	65.2	164.1	**171.8**	170.2	168.5

Table 6.9. Mean generated power as a function of wave period for A = 1.5 m.

With the exception of the wave periods of 5 and 6 seconds, where the maximum mean generated power is attained at $C_{coe} = 15$ and $C_{coe} = 10$, respectively, for all the other wave periods, the highest value of mean generated power is attained at $C_{coe} = 7$. This is similar to what is observed for A = 1.0 m, however, in this case, the mean generated power for almost all the considered wave periods is approximately three times the corresponding power generated without phase control. The differences in mean generated power between the employed control coefficient values are fairly small for wave periods greater than 6 seconds. For a wave amplitude of 1.5 m, the mean

generated power is not a monotonic function of the wave period in all five control approaches considered.

The corresponding power absorption efficiency is reported in Table 6.10. The efficiency is quite high for wave periods near the natural heave period of the point absorber but, in this case, it attains its maximum value at a wave period of 7 seconds for $C_{coe} = 4$ and $C_{coe} = 7$, while it attains its maximum value at a wave period of 6 seconds for $C_{coe} = 10$ and $C_{coe} = 15$. Even though there is a slight decrease in maximum attained efficiency for the 1.5-m-amplitude case compared to the 1.0-m-amplitude case, a closer inspection of the data listed in Tables 6.7 and 6.10 reveals that the variation in power absorption efficiency between corresponding pairs of wave period and wave amplitude is not substantial.

Wave period, T (s)	**η_{pa} (%) (NPC)**	**η_{pa} (%) ($C_{coe} = 4$)**	**η_{pa} (%) ($C_{coe} = 7$)**	**η_{pa} (%) ($C_{coe} = 10$)**	**η_{pa} (%) ($C_{coe} = 15$)**
5	11.5	16.0	27.5	29.3	**30.2**
6	11.0	27.7	32.9	**32.9**	31.3
7	10.4	31.1	**33.2**	31.6	29.7
8	10.0	28.2	**30.2**	29.1	27.8
9	10.1	24.3	**26.2**	25.8	25.0
10	9.53	19.9	**21.4**	21.3	20.9
11	8.57	18.8	**20.7**	20.5	19.9
12	7.74	19.3	**20.2**	20.1	19.6
13	7.10	17.9	**18.7**	18.5	18.4

Table 6.10. Power absorption efficiency as a function of wave period for A = 1.5 m.

The absolute value of the maximum motion amplitude of the point absorber for A = 1.5 m is listed in Table 6.11. Phase control increases the motion amplitude substantially compared to the no-phase-control case for any wave period listed in Table 6.11. A closer inspection of the data listed in Tables 6.8 and 6.11 reveals that the increase for the NPC case is fairly small, the opposite is true

for every value of the control coefficient. Similar to the conclusions drawn for A = 1.0 m, there is a trade-off between minimizing the motion amplitude, with $C_{coe} = 15$, and maximizing the mean generated power, with $C_{coe} = 7$.

Wave period, T (s)	A_{max} (m) (NPC)	A_{max} (m) ($C_{coe} = 4$)	A_{max} (m) ($C_{coe} = 7$)	A_{max} (m) ($C_{coe} = 10$)	A_{max} (m) ($C_{coe} = 15$)
5	**0.400**	1.77	1.58	1.46	1.25
6	**0.470**	1.84	1.62	1.44	1.32
7	**0.542**	2.05	1.83	1.66	1.51
8	**0.608**	2.29	2.09	1.91	1.78
9	**0.694**	2.49	2.33	2.19	2.05
10	**0.740**	2.59	2.42	2.30	2.17
11	**0.790**	2.66	2.53	2.44	2.33
12	**0.830**	2.70	2.56	2.49	2.40
13	**0.860**	2.71	2.60	2.50	2.42

Table 6.11. Maximum motion amplitude as a function of wave period for A = 1.5 m.

6.6 Impact of Phase Control on the Point Absorber Response in Regular Waves

As mentioned earlier, the phase control accumulators are used in an attempt to match the phase of the point absorber velocity with the phase of the wave excitation force. Prior to discussing the impact of phase control on the point absorber motion, the case of no phase control (NPC) is considered. Figure 6.2 shows the variation of the point absorber velocity and wave excitation force during a specific part of the simulation when there is no phase control on the point absorber. The maximum value of the velocity is 0.5 m/s. The regular wave considered has a wave amplitude of 1.5 m and a wave period of 13 s. Evidently, the velocity and the wave excitation force are out of phase. Let us now consider the case of the point absorber subject to phase control. The control coefficient chosen for the phase control operation is $C_{coe} = 7$. Figure 6.3 shows the phase control

accumulator opening instant t_{pco}, and the wave excitation force peak instant t_{fpeak}. The time $(T_0/7)$ is also shown in the plot.

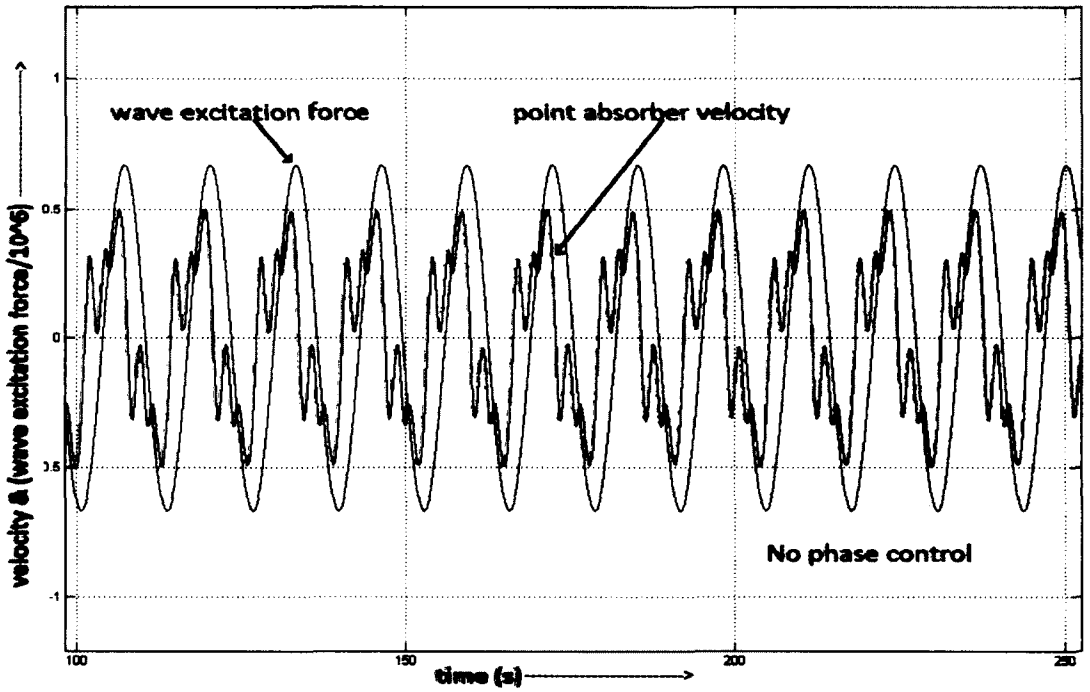

Figure 6.2. Point absorber velocity and wave excitation force without phase control.

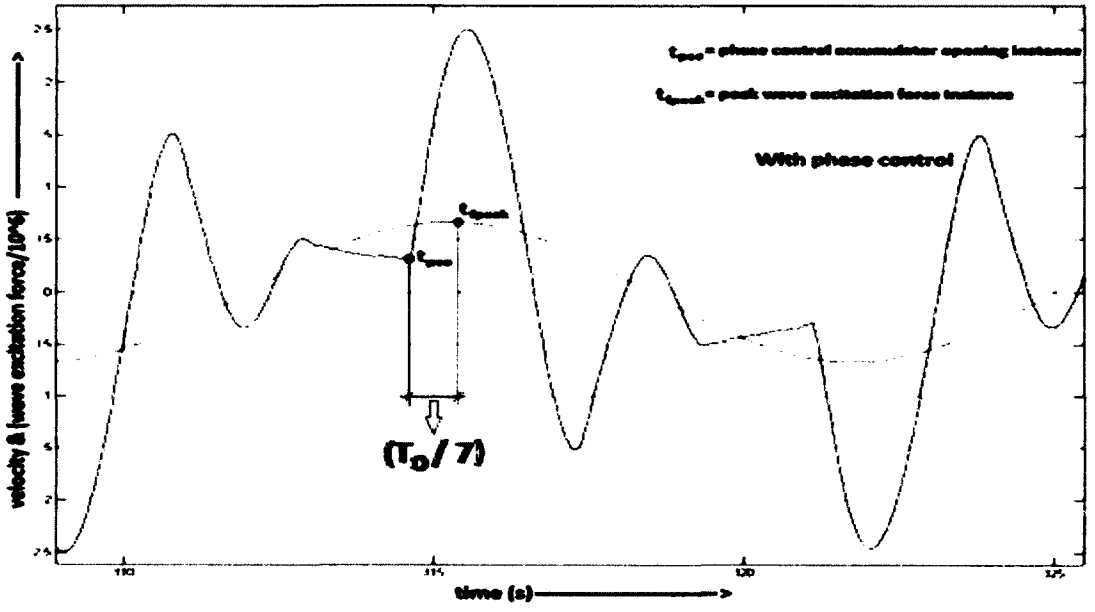

Figure 6.3. Point absorber velocity and wave excitation force with phase control.

The valves of the phase control accumulators are opened at 314.6 seconds and the wave excitation force attains a peak value at 315.4 seconds. After the valves have been opened, the velocity of the point absorber attains a peak value of approximately 2.46 m/s at 315.5 seconds. Therefore, phase control has successfully altered the natural response of the point absorber in such a way that the point absorber's velocity and the wave excitation force reach their peak values almost simultaneously. Subsequently, the control valves are closed when the point absorber velocity becomes zero at time 316.6 seconds. The aforementioned procedure is then repeated before reaching the wave trough, as can be seen in Figure 6.3.

6.6.1 Pressure and volume variation in the compressibility accumulators during phase control

The pressure and volume in the compressibility accumulators (*c* & *d*) vary during phase control operations. Figures 6.4 and 6.5 show the variation in pressure and volume, respectively. The phase control accumulators are activated at time 321.1 seconds, which results in pressure increase in accumulator *d* and pressure drop in accumulator *c*. The point absorber motion is accelerated downward and attains a maximum velocity of 2.46 m/s at time 322.1 seconds. The wave force attains a peak value of $-6.7020 \cdot 10^5$ N at time 321.8 seconds. Subsequently, at time 323.2 seconds, the control valves of the phase control accumulators are closed. This cycle is then repeated before reaching the wave crest.

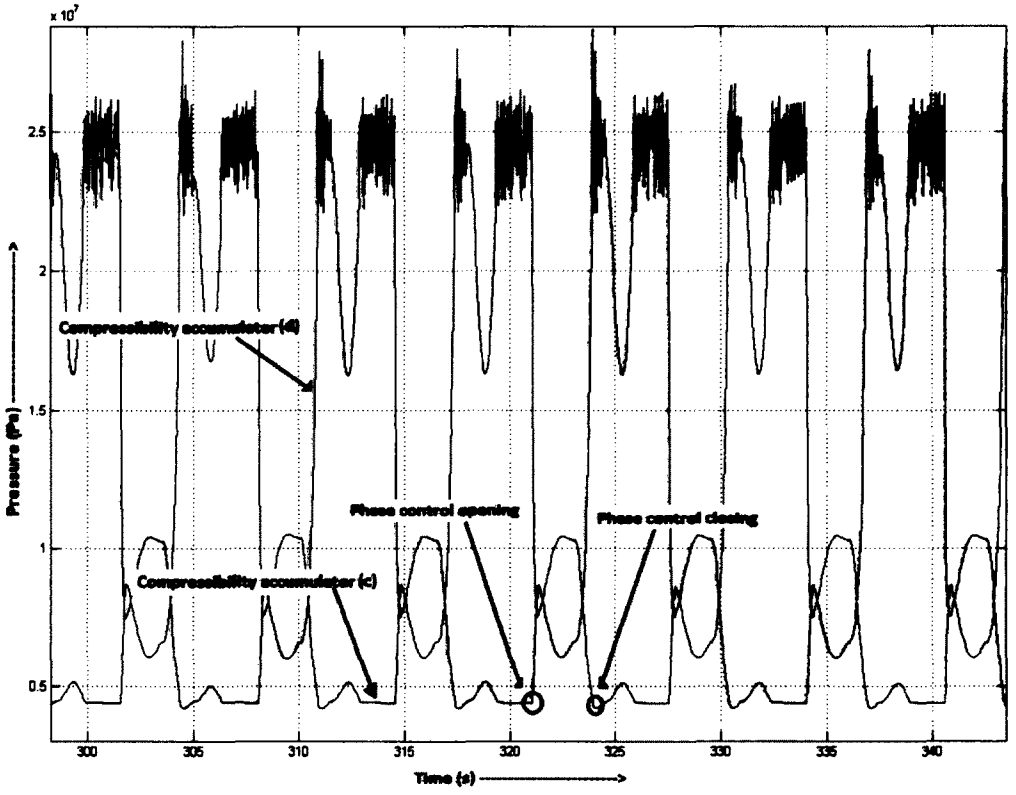

Figure 6.4. Pressure variation in compressibility accumulators during phase control operations.

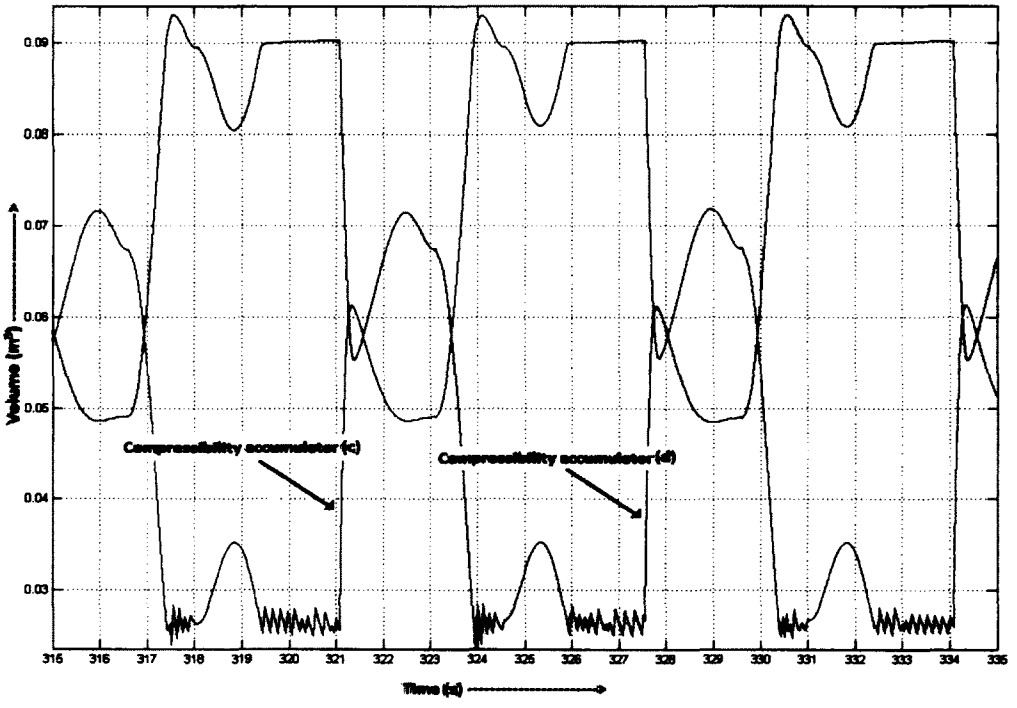

Figure 6.5. Volume variation in compressibility accumulator during phase control operations.

6.6.2 Pressure and volume variation in the phase control accumulators during phase control

During phase control operations, the phase control accumulators are alternatively charged and discharged depending on the direction of motion of the point absorber. For instance, when the point absorber, subject to phase control, is moving upwards, the pressure in phase control accumulator *e* increases (charged) and the pressure in phase control accumulator *f* decreases (discharged). The opposite occurs when the phase controlled point absorber starts to move downwards. Figures 6.6 and 6.7 show the variation in pressure and volume, respectively. When the control valves of the phase control accumulators are closed, the pressure in the accumulator remains a constant.

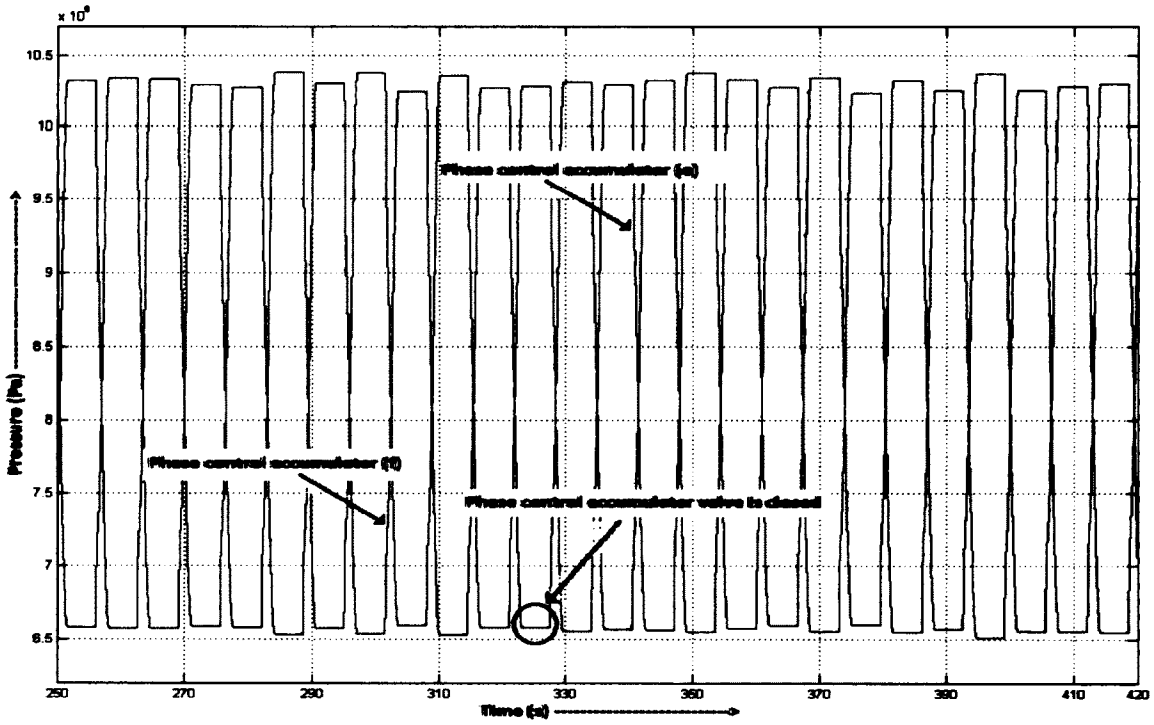

Figure 6.6. Pressure variation in phase control accumulators during phase control operations.

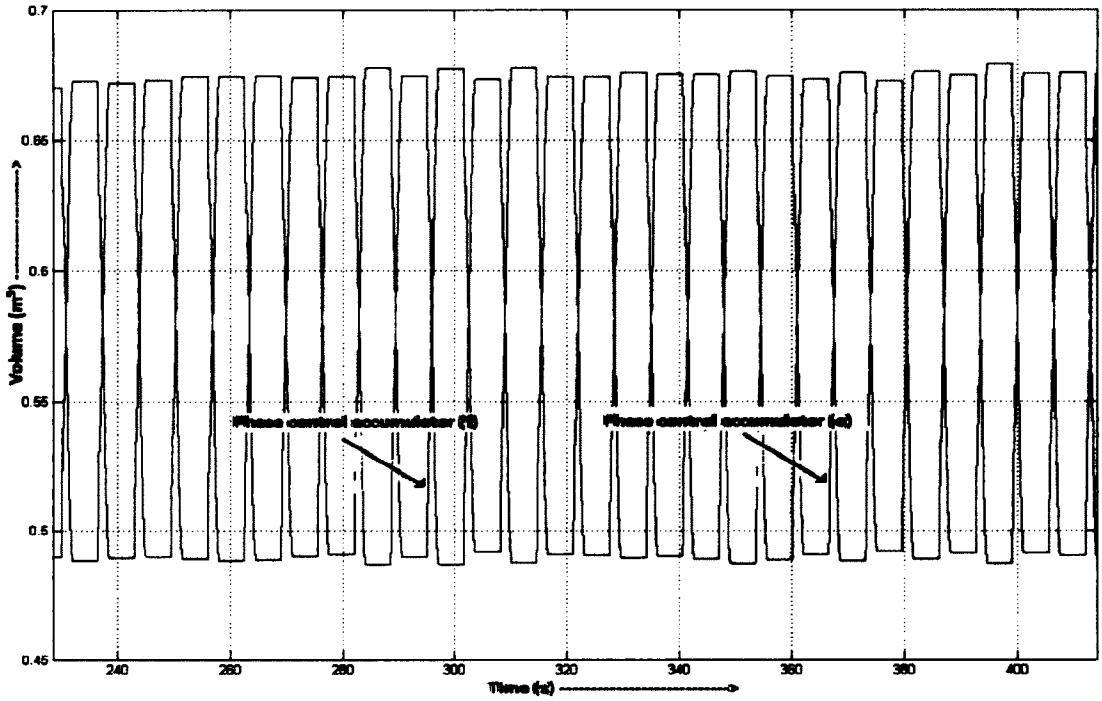

Figure 6.7. Volume variation in phase control accumulators during phase control operations.

6.6.3 Pressure and volume variation in the HP and the LP accumulators during phase control

The pressure difference between the HP and the LP accumulator is used to run a fixed-speed, variable-displacement motor in the hydraulic PTO system. Figures 6.8 and 6.9 show the variation in pressure and volume, respectively, in the HP and LP accumulators.

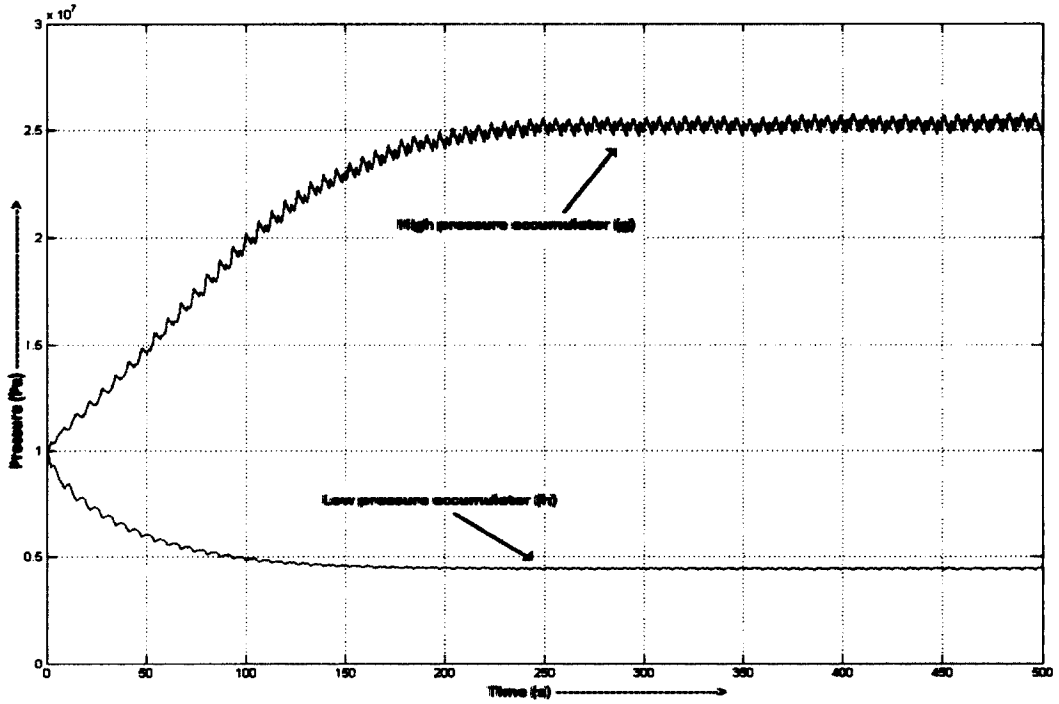

Figure 6.8. Pressure variation in the HP and LP accumulators during phase control operations.

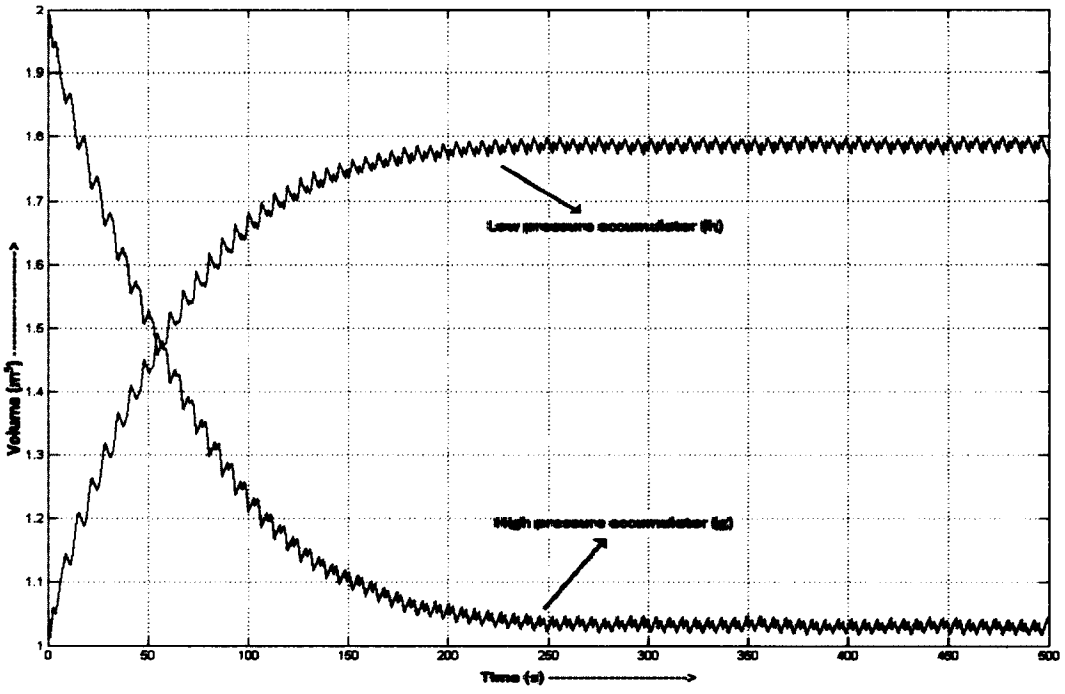

Figure 6.9. Volume variation in the HP and LP accumulators during phase control operations.

CHAPTER VII

SIMULATION RESULTS FOR IRREGULAR SEAS

7.1 Introduction

The components of the point absorber WEC and the hydraulic PTO system described in Chapter III are modelled in the MATLAB® code. This code is used to compute the motion response of the point absorber to irregular waves. Also, motion response of the point absorber when subjected to phase control and no phase control is computed. Furthermore, parameters such as mean generated power of the point absorber WEC system, point absorber efficiency and maximum motion amplitude are computed and tabulated. The point absorber WEC system settings are the same as in the simulations of the regular waves (see Table 6.1).

7.2 Computation of Available Power of Fully-Developed, Deep-Water Irregular Seas

The available power for deep-water, fully developed irregular seas is the maximum power that could be extracted from the waves using a point absorber of known diameter. In the case of irregular seas, the modified Pierson-Moskowitz (P-M) energy distribution spectrum is used in the simulations and, thus, to compute the available power, P_{av}. The modified P-M spectrum is characterized by two parameters: The significant wave height and the modal wave period. The available power in each sea state for fully developed irregular seas, depends on the characteristics of that particular sea state [55]. The expression for the modified P-M spectrum as a function of the wave period, T, is as follows [57]:

$$S(T) = \frac{0.3125 \cdot \left(H_{1/3}\right)^2}{T_{\mathrm{m}}^4} \cdot T^3 \cdot e^{-\left(\frac{1.25}{T_{\mathrm{m}}^4} T^4\right)} \tag{7.1}$$

where $H_{1/3}$ is the significant wave height or mean of one-third highest waves for the chosen sea state and T_m is the corresponding modal wave period. The available power equation for a given sea state and using the modified P-M spectrum can be computed in the following manner:

$$P_{av} = \frac{\rho g^2 r}{2\pi} * \frac{0.3125 * \left(H_{\frac{1}{3}}\right)^2}{T_{\mathrm{m}}^4} * \int_0^{\infty} T^4 * e^{-\left(\frac{1.25}{T_{\mathrm{m}}^4} T^4\right)} dt \qquad (7.2)$$

where ρ is the density of sea water, g is the acceleration of gravity and r is the radius of the point absorber. In the MATLAB® code, the value of the integral is computed in the wave period range of [0, 100] seconds. A detailed derivation of Equation (7.2) is provided in Appendix G. The computed available power in sea states no. 3 through no. 5 is provided in Table 7.1.

Sea state no.	P_{av} (kW)
3	19.5
4	104.6
5	344.7

Table 7.1. Available power for each sea state.

The available power in sea state no. 5 is higher than the available power in sea states no. 3 and 4. This is due to the higher values of T_m and $H_{1/3}$ for sea state no. 5 when compared with the values of the same parameters for sea states no. 3 and 4. This is inferred from the data listed in Table 7.2, which provides the values of modal wave period, significant wave height, and annual probability of occurrence of the most frequently occurring sea states in the North Atlantic [58]. These sea states are used in this investigation.

Sea state	Significant wave height (m) $(H_{1/3})$	Most probable modal wave period (s) (T_m)	Percentage probability of sea state (%)
3	0.88	7.5	23.70
4	1.88	8.8	27.80
5	3.25	9.7	20.64

Table 7.2. Annual sea state characteristics and occurrence in the North Atlantic.

7.3 Simulation Results for Fully-Developed Irregular Seas

As mentioned earlier, the modified P-M energy spectrum is used to represent the state of the sea. It is assumed that the waves are irregular and occur in deep water. The state of the sea is assumed to be fully developed. Sea states no. 2 and 6 are not considered in the irregular wave simulations because sea state no. 2 has a low probability of occurrence of 6.8 % and sea state no. 6 has a very high significant wave height of 5.0 m.

The fraction of the maximum volumetric displacement of the hydraulic motor, f_{dc}, is also utilized as a control coefficient. Four discrete values are considered: $f_{dc} = \{0.25, 0.50, 0.75, 1.00\}$.

Given that irregular seas are non-deterministic by nature, a random number generator (RNG) is used in order to set the random seed and provide the series of random numbers used in the computation of the wave excitation force. The random number generator seed is varied from one to ten in steps of one. For each sea state and value of f_{dc}, ten simulation runs are performed for each value of C_{coe}, and also for the case of no phase control (NPC). After each run, the numerical values of critical parameters such as mean generated power, power absorption efficiency, and the absolute value of the maximum motion amplitude are recorded. Data sets of two critical parameters, mean generated power and maximum motion amplitude, are subjected to statistical analysis because of their usage in assessing the performance of the point absorber WEC system. The non-parametric Kolmogorov-Smirnov (K-S) test for normality is performed to see whether the data follows a normal distribution. The null and alternative hypotheses for the K-S test are as follows,

Null hypothesis: *The data set follows a normal distribution.*

Alternative hypothesis: The data set does not follow a normal distribution.

Subsequently, if it has been verified that the examined data sets follow a normal distribution, the two-tailed Student's t-test with paired samples (same *rng* seed) is performed on the

corresponding data for a given sea state and value of fraction of the motor's maximum volumetric displacement. The first set of hypotheses involves testing whether phase control has a statistically significant effect on the mean generated power by applying the t-test to the C_{coe} data set with the highest average value (HAV) of the mean generated power in the ten runs and to the corresponding NPC data set. The null and alternative hypotheses for this test are as follows,

Null hypothesis: The means of the populations from which HAV and NPC are obtained are equal, i.e., phase control does not have a statistically significant effect on the mean generated power.

Alternative hypothesis: The means of the populations from which HAV and NPC are obtained are not equal, i.e., phase control has a statistically significant effect on the mean generated power.

A similar test is applied to the C_{coe} data set with the lowest average value (LAV) of the maximum motion amplitude and to the corresponding NPC data set. Subsequently the *t*-test is employed in order to investigate whether the instant at which the control valves are opened, t_{pco}, relative to the instant when the next wave excitation peak occurs, t_{fpeak}, has a statistically significant effect on the mean generated power. The t-test is applied to the data sets with the highest and lowest average values, HAV and LAV, respectively.

The aforementioned t-tests are two tailed. The statistical significance is investigated at the 0.05 (5%) level. In this way, if the probability of obtaining the investigated data sets when the null hypothesis is true, or else the p-value is less than or equal to 0.05, then the null hypothesis is rejected. All the simulations for irregular seas are conducted for a total time of 1,500 seconds and a time step of 0.03 seconds.

7.3.1 Results for sea state no. 3

Sea state no. 3 has an available power of 19.5 kW, significant wave height of 0.88 m, most probable wave period of 7.5 seconds, and percentage probability of occurrence of 23.7 %. For a chosen value of fraction of the maximum hydraulic motor displacement, the values of the mean

generated power and the maximum motion amplitude for different control coefficients are provided.

RNG	P_{mg} (kW) (NPC)	P_{mg} (kW) ($C_{coe} = 4$)	P_{mg} (kW) ($C_{coe} = 7$)	P_{mg} (kW) ($C_{coe} = 10$)	P_{mg} (kW) ($C_{coe} = 15$)
rng(1)	0.767	1.011	1.084	1.106	1.133
rng(2)	0.984	1.309	1.338	1.398	1.322
rng(3)	1.062	1.448	1.648	1.544	1.595
rng(4)	1.141	1.631	1.662	1.722	1.675
rng(5)	1.026	1.414	1.543	1.539	1.409
rng(6)	1.019	1.425	1.545	1.626	1.588
rng(7)	0.764	0.990	0.967	0.957	1.023
rng(8)	0.903	1.263	1.326	1.275	1.253
rng(9)	1.187	1.758	1.700	1.676	1.561
rng(10)	1.001	1.507	1.568	1.582	1.528
AVG	*0.985*	**1.376**	1.438	***1.442***	1.409
STD-DEV	0.140	0.244	0.252	0.255	0.219

Table 7.3. Mean generated power, sea state no. 3, f_{dc} = 0.25.

Table 7.3 shows the mean generated power, P_{mg}, values for f_{dc} = 0.25. The overall lowest average mean generated power is 0.985 KW and corresponds to the NPC case. The corresponding value of power absorption efficiency is 5.04 %. The highest average mean generated power value is 1.442 kW (shown in bold font and italics) and the corresponding value of power absorption efficiency is 7.38 %. Among the four phase-controlled cases, the lowest average mean generated power value of 1.376 kW, shown in bold font, and is computed for C_{coe} = 4. The corresponding value of power absorption efficiency is 7.04 %.

The five data sets listed in Table 7.3 are first subjected to the K-S test. The results of the test reveal that all the data sets most likely follow a normal distribution. Therefore, it is appropriate to utilize Student's t-test for further statistical comparisons. The t-test is employed twice. The first time, it

is used to check whether phase control has a statistically significant effect on the mean generated power. In this case, the test is performed between the NPC and the C_{coe} = 10 cases. The calculated *p*-value of the t-test is $1.43 \cdot 10^{-6}$. Therefore, the null hypothesis is rejected and, thus, phase control has a statistically significant effect on the mean generated power of the heaving point absorber WEC system.

Subsequently the t-test is employed in order to investigate whether the instant at which the control valves are opened, t_{pco}, relative to the instant when the next wave excitation peak occurs, t_{fpeak}, has a statistically significant effect on the mean generated power. The t-test is applied to the aforementioned C_{coe} values with the highest and lowest average mean generated power values, 10 and 4, respectively. The calculated p-value of the t-test is $2.84 \cdot 10^{-2}$ and, thus, the null hypothesis is again rejected.

The statistics regarding the maximum motion amplitude are also of some interest because high motion amplitudes could potentially compromise the structural integrity of the WEC system. Another cause for concern is the conclusion drawn in Chapter VI regarding the trade-off between maximizing the mean generated power while minimizing the maximum motion amplitude. Even though, the latter is more a constraint than an optimization objective, control strategies that provide smaller motion amplitudes at higher sea states might be preferable than their power-absorption-maximizing counterparts. The data sets listed in Table 7.4 show the maximum motion amplitude values, A_{max}, for the f_{dc} value of 0.25. Using a similar statistical testing procedure as in the mean generated power case, the statistics of the simulation results listed in Table 7.4 are analyzed and the impact of different control strategies on the WEC system performance is assessed. First, the K-S test is applied to the five data sets and reveals that all the data sets probably follow a normal distribution. The t-test is then applied, first, to the pair of NPC and the C_{coe} value with the lowest average maximum motion amplitude value (shown in bold font and

italics), which in this case corresponds to C_{coe} = 4; subsequently, it is applied to the pair with the lowest/highest average maximum motion amplitude values, C_{coe} = 15 and C_{coe} = 4, respectively.

RNG	A_{max} (m) **(NPC)**	A_{max} (m) $(C_{coe} = 4)$	A_{max} (m) $(C_{coe} = 7)$	A_{max} (m) $(C_{coe} = 10)$	A_{max} (m) $(C_{coe} = 15)$
rng(1)	0.322	0.392	0.379	0.372	0.335
rng(2)	0.429	0.542	0.506	0.490	0.464
rng(3)	0.399	0.493	0.472	0.465	0.443
rng(4)	0.365	0.460	0.437	0.419	0.415
rng(5)	0.341	0.410	0.385	0.375	0.370
rng(6)	0.416	0.606	0.586	0.498	0.476
rng(7)	0.302	0.365	0.410	0.405	0.401
rng(8)	0.288	0.402	0.361	0.387	0.357
rng(9)	0.524	0.666	0.633	0.610	0.583
rng(10)	0.442	0.557	0.529	0.508	0.497
AVG	0.383	**0.489**	0.470	0.453	***0.434***
STD-DEV	0.073	0.101	0.092	0.076	0.075

Table 7.4. Maximum motion amplitude, sea state no. 3, f_{dc} = 0.25.

The calculated p-value of the first test is $7.33 \cdot 10^{-5}$. Therefore, phase control has a statistically significant effect on the maximum motion amplitude of the point absorber. For the second t-test, the p-value is $2.38 \cdot 10^{-3}$. Therefore, the change in the control coefficient value has a statistically significant effect on the maximum-motion-amplitude of the point absorber.

The results that are presented for the other test cases are given in terms of their statistical properties, i.e., average and standard deviation values. The HAV of the mean generated power among the four phase-controlled data sets is highlighted in bold font and italics, while the LAV is displayed in bold font. Regarding the maximum motion amplitude, the LAV of the four phase-controlled data sets is highlighted in bold font and italics, while the HAV is displayed in bold font.

It needs to be mentioned that in all cases the application of the K-S test to the corresponding data sets reveals that all the data sets probably follow a normal distribution.

f_{dc}	Statistical parameter	P_{mg} (kW)				
		NPC	$C_{coe} = 4$	$C_{coe} = 7$	$C_{coe} = 10$	$C_{coe} = 15$
$f_{dc} = 0.50$	**AVG**	0.476	**0.406**	0.461	0.471	***0.472***
	STD-DEV	0.067	0.077	0.089	0.094	0.088
$f_{dc} = 0.75$	**AVG**	0.475	**0.323**	0.362	0.385	***0.393***
	STD-DEV	0.026	0.037	0.035	0.034	0.042
$f_{dc} = 1.00$	**AVG**	0.573	**0.339**	0.390	0.407	***0.429***
	STD-DEV	0.011	0.024	0.023	0.019	0.035

Table 7.5. Mean generated power, sea state no. 3, f_{dc}= {0.50, 0.75, 1.00}.

In Table 7.5, the average and standard deviation values of the mean generated power for f_{dc} values of 0.50, 0.75, and 1.00 are provided. The corresponding t-test results, in terms of the calculated p-values, are listed in Table 7.6. In the cases where the p-values are less than or equal to 0.05, the corresponding values are highlighted in bold font.

In Table 7.7, the average and standard deviation values of the maximum motion amplitude for f_{dc} values of 0.50, 0.75, and 1.00 are provided. The corresponding t-test results are listed in Table 7.8.

f_{dc}	p-value	
	NPC - HAV	HAV - LAV
$f_{dc} = 0.50$	$6.44 \cdot 10^{-1}$	**$2.41 \cdot 10^{-5}$**
$f_{dc} = 0.75$	**$3.87 \cdot 10^{-7}$**	**$3.36 \cdot 10^{-6}$**
$f_{dc} = 1.00$	**$7.09 \cdot 10^{-8}$**	**$3.72 \cdot 10^{-6}$**

Table 7.6. T-test results for mean generated power, sea state no. 3, f_{dc}= {0.50, 0.75, 1.00}.

f_{dc}	Statistical parameter	A_{max} (m)				
		NPC	$C_{coe} = 4$	$C_{coe} = 7$	$C_{coe} = 10$	$C_{coe} = 15$
$f_{dc} = 0.50$	**AVG**	0.412	**0.494**	0.481	0.475	***0.462***
	STD-DEV	0.070	0.083	0.080	0.094	0.093
$f_{dc} = 0.75$	**AVG**	0.437	**0.513**	0.485	0.481	***0.465***
	STD-DEV	0.073	0.107	0.123	0.095	0.071
$f_{dc} = 1.00$	**AVG**	0.449	***0.501***	0.509	**0.514**	0.509
	STD-DEV	0.081	0.111	0.116	0.130	0.126

Table 7.7. Maximum motion amplitude, sea state no. 3, f_{dc} = {0.50, 0.75, 1.00}.

f_{dc}	p-value	
	NPC - HAV	HAV - LAV
$f_{dc} = 0.50$	**$2.29 \cdot 10^{-2}$**	**$4.74 \cdot 10^{-2}$**
$f_{dc} = 0.75$	**$1.62 \cdot 10^{-2}$**	**$2.76 \cdot 10^{-2}$**
$f_{dc} = 1.00$	**$6.91 \cdot 10^{-3}$**	$4.22 \cdot 10^{-1}$

Table 7.8. T-test results for maximum motion amplitude, sea state no. 3, f_{dc} = {0.50, 0.75, 1.00}.

Given that point absorber motion amplitude is critical to the structural integrity of the WEC device, it is important to keep the maximum motion amplitude within reasonable bounds.

However, if the point absorber is too constrained to heave, the mean generated power from the point absorber WEC system reduces. Therefore, for a heaving point absorber in a certain sea state, values of fraction of motor maximum displacement and control coefficient must be chosen such that power generation is maximized and maximum motion amplitude is kept within reasonable bounds. To this end, a control strategy can be devised based on the average values of mean generated power and maximum motion amplitude shown in Tables 7.3 through 7.8. The following section provides details about such control strategies.

As a control strategy, for a point absorber WEC device in sea state 3, the fraction of motor maximum displacement of 0.25 and control coefficient C_{coe} value of 10 can be chosen as it leads to a peak mean generated power value of 1.442 kW and maximum motion amplitude of 0.453 m. If the point absorber maximum motion amplitude is to be reduced, an alternate strategy is to switch to the control coefficient value of 15 while maintaining the f_{dc} value at 0.25. This leads to a minimum maximum motion amplitude value of 0.434 m and mean generated power of 1.409 kW. The maximum motion amplitude can be further lowered to 0.383 m by switching to no phase control. However, this reduces the mean generated power to 0.985 kW.

When the f_{dc} value is changed to 0.5 the mean generated power reaches a peak value of 0.476 kW for no phase control. However, the application of phase control for the f_{dc} value of 0.5 reduces the mean generated power further. Despite a reduction in mean generated power, the maximum motion amplitude tends to increase. It reaches a maximum value of 0.494 m for the phase control coefficient value of 4. Similar trends are observed for f_{dc} values of 0.75 and 1.00. Therefore, for a heaving point absorber in sea state 3, the fraction of motor maximum displacement of 0.25 is better suited as it increases mean generated power while keeping maximum motion amplitude within reasonable bounds.

7.3.2 Results for sea state no. 4

Sea state no. 4 has an available power of 104.6 kW, significant wave height of 1.88 m, most probable wave period of 8.8 seconds, and percentage probability of occurrence of 27.8 %. In Table 7.9, the average and standard deviation values of the mean generated power for f_{dc} values of 0.25, 0.50, 0.75, and 1.00 are provided. The corresponding t-test results are listed in Table 7.10. In Table 7.11, the average and standard deviation values of the maximum motion amplitude for f_{dc} values of 0.25, 0.50, 0.75, and 1.00 are provided with the corresponding t-test results listed in Table 7.12.

f_{dc}	Statistical parameter	P_{mg} (kW)				
		NPC	$C_{coe} = 4$	$C_{coe} = 7$	$C_{coe} = 10$	$C_{coe} = 15$
$f_{dc} = 0.25$	AVG	4.96	**11.51**	***11.67***	11.62	11.53
	STD-DEV	0.481	1.12	1.13	1.13	1.29
$f_{dc} = 0.50$	AVG	4.03	6.50	***6.71***	6.56	**6.30**
	STD-DEV	0.533	1.35	1.32	1.28	1.26
$f_{dc} = 0.75$	AVG	2.60	**2.44**	2.57	***2.68***	2.60
	STD-DEV	0.450	0.657	0.628	0.638	0.631
$f_{dc} = 1.00$	AVG	1.43	**1.28**	1.47	***1.49***	1.47
	STD-DEV	0.315	0.307	0.373	0.364	0.345

Table 7.9. Mean generated power, sea state no. 4.

f_{dc}	p-value	
	NPC - HAV	**HAV - LAV**
$f_{dc} = 0.25$	**$7.05 \cdot 10^{-10}$**	**$2.14 \cdot 10^{-3}$**
$f_{dc} = 0.50$	**$4.96 \cdot 10^{-6}$**	**$5.75 \cdot 10^{-3}$**
$f_{dc} = 0.75$	**$1.52 \cdot 10^{-3}$**	**$3.54 \cdot 10^{-5}$**
$f_{dc} = 1.00$	$1.81 \cdot 10^{-1}$	**$9.24 \cdot 10^{-4}$**

Table 7.10. T-test results for mean generated power, sea state no. 4.

f_{dc}	Statistical parameter	A_{max} (m)				
		NPC	$C_{coe} = 4$	$C_{coe} = 7$	$C_{coe} = 10$	$C_{coe} = 15$
$f_{dc} = 0.25$	**AVG**	0.805	**1.378**	1.313	1.278	***1.252***
	STD-DEV	0.154	0.152	0.150	0.142	0.140
$f_{dc} = 0.50$	**AVG**	0.875	**1.170**	1.129	1.069	***1.062***
	STD-DEV	0.155	0.212	0.215	0.143	0.141
$f_{dc} = 0.75$	**AVG**	0.940	**1.183**	1.157	1.092	***1.051***
	STD-DEV	0.139	0.241	0.219	0.152	0.138
$f_{dc} = 1.00$	**AVG**	0.977	**1.174**	1.218	***1.140***	1.146
	STD-DEV	0.141	0.172	0.233	0.150	0.229

Table 7.11. Maximum motion amplitude, sea state no. 4.

As a control strategy, for a point absorber WEC device in sea state 4, the fraction of motor maximum displacement of 0.25 and control coefficient C_{coe} value of 7 can be chosen as it leads to a peak average mean generated power value of 11.61 kW and maximum motion amplitude of 1.313 m. However, a reduction in the point absorber maximum motion amplitude can be achieved by switching to the control coefficient value of 10 while maintaining the f_{dc} value at 0.25. This leads to a maximum motion amplitude value of 1.278 m and an average mean generated power of 11.62 kW. For the same f_{dc} value, another strategy is to choose the control coefficient value

of 15 which results in a mean generated power of 11.53 kW and maximum motion amplitude of 1.252 m.

f_{dc}	p-value	
	NPC - HAV	**HAV - LAV**
$f_{dc} = 0.25$	**$7.19 \cdot 10^{-7}$**	**$4.83 \cdot 10^{-6}$**
$f_{dc} = 0.50$	**$9.76 \cdot 10^{-4}$**	**$5.74 \cdot 10^{-3}$**
$f_{dc} = 0.75$	**$6.60 \cdot 10^{-3}$**	**$1.31 \cdot 10^{-2}$**
$f_{dc} = 1.00$	**$2.81 \cdot 10^{-3}$**	$1.33 \cdot 10^{-1}$

Table 7.12. T-test results for maximum motion amplitude, sea state no. 4.

The maximum motion amplitude can be further reduced by changing the f_{dc} value to 0.5 and choosing a control coefficient value of 7. This leads to a mean generated power of 6.71 kW and maximum motion amplitude of 1.129 m. For the same value of f_{dc}, choosing control coefficient value of 10 leads to a further lowering of the maximum motion amplitude to 1.069 m and mean generated power to 6.56 kW. An increase in the f_{dc} value to 0.75, reduces the mean generated power to 2.68 kW for the control coefficient of 10. The corresponding maximum motion amplitude increases to 1.092 m. A change in the f_{dc} value to 1.00, further reduces the mean generated power to 1.49 kW for the control coefficient of 10. The corresponding maximum motion amplitude increases to 1.140 m.

For the f_{dc} value of 0.25 and no phase control, interestingly, the mean generated power is 4.96 kW and the maximum motion amplitude is 0.805 m. This mean generated power is higher than the mean generated power for f_{dc} values of 0.75 and 1.00. And the maximum motion amplitude

of 0.805 m is lower than the maximum motion amplitude for f_{dc} values of 0.75 and 1.00. Therefore, a better strategy is to choose the f_{dc} value of 0.25 and no phase control on the point absorber instead of f_{dc} values of 0.75 and 1.00.

7.3.3 Results for sea state no. 5

Sea state no. 5 has an available power of 344.7 kW, significant wave height of 3.25 m, most probable wave period of 9.7 seconds, and percentage probability of occurrence of 20.64 %. %. In Table 7.13, the average and standard deviation values of the mean generated power are provided. The corresponding t-test results are listed in Table 7.14. In Table 7.15, the average and standard deviation values of the maximum motion amplitude are provided with the corresponding t-test results listed in Table 7.16.

f_{dc}	Statistical parameter	P_{mg} (kW)				
		NPC	$C_{coe} = 4$	$C_{coe} = 7$	$C_{coe} = 10$	$C_{coe} = 15$
$f_{dc} = 0.25$	AVG	11.80	30.70	***31.32***	30.98	**30.68**
	STD-DEV	0.80	2.03	2.10	2.36	2.37
$f_{dc} = 0.50$	AVG	14.94	35.02	***35.38***	35.07	**34.43**
	STD-DEV	1.50	3.98	4.20	4.16	4.41
$f_{dc} = 0.75$	AVG	12.85	25.80	***25.84***	25.31	**24.72**
	STD-DEV	1.63	5.06	4.63	4.38	4.14
$f_{dc} = 1.00$	AVG	9.12	**12.91**	13.15	***13.73***	13.19
	STD-DEV	1.36	2.28	2.31	2.32	2.25

Table 7.13. Mean generated power, sea state no. 5.

f_{dc}	p-value	
	NPC - HAV	**HAV - LAV**
$f_{dc} = 0.25$	**$1.92 \cdot 10^{-11}$**	**$2.18 \cdot 10^{-3}$**
$f_{dc} = 0.50$	**$8.84 \cdot 10^{-9}$**	**$3.22 \cdot 10^{-3}$**
$f_{dc} = 0.75$	**$6.95 \cdot 10^{-7}$**	**$8.54 \cdot 10^{-3}$**
$f_{dc} = 1.00$	**$2.39 \cdot 10^{-6}$**	**$3.11 \cdot 10^{-5}$**

Table 7.14. T-test results for mean generated power, sea state no. 5.

f_{dc}	Statistical parameter	A_{max} (m)				
		NPC	$C_{coe} = 4$	$C_{coe} = 7$	$C_{coe} = 10$	$C_{coe} = 15$
$f_{dc} = 0.25$	**AVG**	1.363	**2.750**	2.684	2.631	***2.579***
	STD-DEV	0.246	0.293	0.278	0.270	0.262
$f_{dc} = 0.50$	**AVG**	1.441	**2.380**	2.350	2.304	***2.290***
	STD-DEV	0.29	0.317	0.277	0.266	0.314
$f_{dc} = 0.75$	**AVG**	1.591	**2.192**	2.097	2.059	***2.019***
	STD-DEV	0.275	0.236	0.236	0.233	0.244
$f_{dc} = 1.00$	**AVG**	1.698	**2.086**	2.029	1.987	***1.952***
	STD-DEV	0.256	0.304	0.296	0.285	0.279

Table 7.15. Maximum motion amplitude, sea state no. 5.

As a control strategy, for a point absorber WEC device in sea state 5, the fraction of motor maximum displacement of 0.25 and control coefficient C_{coe} value of 7 can be chosen as it leads to a peak mean generated power value of 31.32 kW and maximum motion amplitude of 2.684 m. However, a reduction in the point absorber maximum motion amplitude can be achieved by switching to the control coefficient value of 10 while maintaining the f_{dc} value at 0.25. This leads to a maximum motion amplitude value of 2.631 m and mean generated power of 30.98 kW. For

the same f_{dc} value, another strategy is to choose the control coefficient value of 15 which results in a mean generated power of 30.68 kW and maximum motion amplitude of 2.579 m.

f_{dc}	p-value	
	NPC - HAV	**HAV - LAV**
$f_{dc} = 0.25$	**$6.67 \cdot 10^{-9}$**	**$1.05 \cdot 10^{-5}$**
$f_{dc} = 0.50$	**$7.30 \cdot 10^{-7}$**	**$3.39 \cdot 10^{-2}$**
$f_{dc} = 0.75$	**$2.31 \cdot 10^{-5}$**	**$4.60 \cdot 10^{-7}$**
$f_{dc} = 1.00$	**$1.54 \cdot 10^{-4}$**	**$5.40 \cdot 10^{-4}$**

Table 7.16. T-test results for maximum motion amplitude, sea state no. 5.

An increase in mean generated power and a decrease in maximum motion amplitude can be achieved by changing the f_{dc} value to 0.5 and choosing a control coefficient value of 7. This combination leads to a mean generated power of 35.38 kW and a maximum motion amplitude of 2.350m. For the same value of f_{dc}, a switch to control coefficient value of 10 reduces the mean generated power to 35.07 kW and maximum motion amplitude to 2.304 m. A change in the f_{dc} value from 0.5 to 0.75, reduces the mean generated power and maximum motion amplitude to 25.84 kW and 2.097 m respectively for a control coefficient of 7. While maintaining the same f_{dc} value of 0.75, a switch to control coefficient 10, further reduces, though slightly, the maximum motion amplitude and mean generated power to 2.059m and 25.31 kW respectively.

When the value of f_{dc} is increased to 1.00, the mean generated power attains a maximum of 13.73 kW with a corresponding maximum motion amplitude value of 1.987 m for the control coefficient of 10. Although the maximum motion amplitude decreases, a better strategy, instead,

is to change the f_{dc} value to 0.5 and switch to no phase control on the point absorber. This combination results in a mean generated power of 14.94 kW and maximum motion amplitude of 1.441 m.

CHAPTER VIII

SIMULATIONS OF THE WEC SYSTEM WITH THE REINFORCEMENT LEARNING CONTROLLER

8.1 Introduction

In this chapter, numerical experiments are conducted in order to investigate the performance of a controller based on Reinforcement learning (RL) when controlling the heaving motion of the point absorber of a WEC system in regular and irregular waves. The training of the controller is done using a modified version of the Q-learning method described in Chapter IV. The ability of the RL-based controller to obtain an optimal policy is validated first in regular waves. Subsequently, the modified P-M spectrum is employed to obtain a time series of wave excitation and train the controller in irregular seas. The computed optimal policy is then tested on the P-M spectrum for fully developed seas. During the training and validation of the controller, perfect knowledge of the future wave excitation is assumed. In an actual implementation of the proposed control approach, the wave excitation will need to be predicted for a specific time period in the near future, thus, the RL-based controller is combined with the RBF-network predictor presented in Chapter V. The impact of the level of accuracy of the predicted wave excitation on the generated power is then investigated using the previously derived control policy.

8.2 Reinforcement-Learning-based Controller for Constrained Phase Control of a Heaving WEC

An adaptation of the Q-learning algorithm [78] is utilized to compute the optimal policy in order to control the heaving point absorber WEC system presented in Chapter III. The Q-learning code has been integrated in the R-K4 solver and is available in Appendix J. Using discrete phase control, the valves that connect the hydraulic system to the phase control accumulators are opened at a specific instant before the next wave excitation peak and then are closed when the velocity of the heaving point absorber is equal to zero. The WEC system can be modeled as a discrete event

system, where events, e.g. opening/closing the valves, occur at discrete times, but the amount of time between events is a real-valued variable [125]. The state of the WEC system is defined by the wave excitation peaks. A similar but non-RL-based approach has been utilized in [68], where a threshold value of the pressure difference between the LP and HP accumulators is utilized to determine the instant of the valve activation. It has been demonstrated in [126] that the correlation between two successive wave peaks is fairly high and its value depends on the wave spectrum formulation, but the correlation decreases significantly as the number of consecutive waves considered becomes greater than two. These results support the assumption that successive wave peaks have properties very close to the Markov property [127] and, thus, can be modeled as a Markov Decision Process (MDP) process in an RL-based controller. Considering the fact that the system is modeled as a discrete-event system, the process is a semi-Markov Decision Process (s-MDP).

The state space of a time series of irregular waves is defined as the wave excitation peak; the latter is a continuous variable that is discretized by considering a number of equally divided segments. The state space is defined as: $S = \{s \mid s_n = F_{wp,n}, n \in [1, 2, \dots, N]\}$. The RL-based controller can take two actions at each state: The first action, a_1, corresponds to adjusting the fraction of the motor displacement, f_{dc}, while the second action, a_2, is defined as the value of the control coefficient, C_{coe}, (defined in Chapter III), which determines the time instant when the valve of the phase control accumulator is opened. The action space is defined as follows: $A = \{a \mid a_{k,j} = (a_{1,k}, a_{2,j}),\ k \in [1, 2, \dots K], j \in [1, 2, \dots J]\}$. After the controller has observed the next state, s_{c+1}, it takes a pair of actions, i.e. $(a_{1,c}, a_{2,c})$ and receives a reward between the times the phase control accumulator valve is opened and closed, t_1 and t_2, respectively. The reward is computed as [125]:

$$r_{c+1} = \int_{t_1}^{t_2} e^{-\beta(\tau - t_1)} r_\tau d\tau \tag{8.1}$$

where $r_\tau = P_{gw}$, i.e., the generated electric power at time step τ, and β is a parameter that controls the rate of exponential decay. A constraint is imposed on the reward by specifying a maximum value, x_{crit}, of the motion amplitude. If at any time between t_1 and t_2 the motion amplitude exceeds x_{crit} then r_{c+1} is set equal to zero.

The discount factor is calculated as:

$$\gamma = e^{-\beta(t_2 - t_1)} \tag{8.2}$$

The update of the Q function for the current state s_c and action pair $\boldsymbol{a}_c$ is then performed as follows:

$$Q(s_c, \boldsymbol{a}_c) \leftarrow Q(s_c, \boldsymbol{a}_c) + \eta \left[r_{c+1} + \gamma \max_{\boldsymbol{a}'_c} Q(s_{c+1}, \boldsymbol{a}'_c) - Q(s_c, \boldsymbol{a}_c) \right] \tag{8.3}$$

where η is the learning rate. In order to balance exploration of the search space and utilization of the optimal pair of actions, the following scheme is utilized to select a pair of actions in state s_c at time t: The probability of selecting a random action is defined as, $P_{t+1}(s_c) = \sigma \cdot P_t(s_c)$, with $\sigma = 0.99$. A uniformly distributed random number is generated and if its' value is less than $P_{t+1}(s_c)$, a random action is taken. Otherwise, the action with the maximum Q-value at state s_c is selected. In all the simulations performed as part of the investigation described in this chapter, the following parameter values have been utilized: $\beta = 0.01$, $\eta = 0.05$.

8.3 Numerical Experiments with the Reinforcement-Learning-Based Controller

8.3.1 Regular waves

The first test of the RL-based controller is performed in regular waves. In this case, there is only one state and the controller needs to find the optimal action pair that maximizes the reward over a finite horizon, which corresponds to the total simulation time. For the purpose of this investigation, the total simulation time is set equal to 1,500 seconds and the time step to 0.05

seconds. The wave period is equal to 11 seconds and the wave amplitude is equal to 1.5 m. The maximum value of the motion amplitude is set equal to 2.40 m. The action space is defined using the following values:

$$A_1 = \{0.80, 0.84, 0.88, 0.92, 0.96, 1.00\}, A_2 = \{6, 8, 10, 12, 14\}.$$

In order to validate the results, the WEC system is run by setting the motor displacement fraction and valve opening time to various constant values and manually find the pair of values that optimizes the power absorption without violating the motion amplitude constraint. The results are reported in Table 8.1. The optimal value is shown in bold font. The cases where the motion amplitude does not exceed the constraint value are highlighted in bold font and italics.

f_{dc}, C_{coe}	P_{mg} (kW)	A_{max} (m)
(0.96, 10)	165.8	2.462
(1.00, 10)	164.0	2.440
(0.96, 12)	164.6	2.426
(1.00, 12)	162.0	***2.394***
(0.92, 14)	163.1	2.403
(0.96, 14)	**162.9**	***2.386***
(1.00, 14)	159.8	***2.372***

Table 8.1. Optimal control policy for wave period of 11 seconds and amplitude of 1.5 m.

The RL-based controller is switched on after 375 seconds of simulation time and is able to find the optimal policy, i.e., the optimal pair of actions, within approximately 350 seconds of simulation time as shown in Figure 8.1. It needs to be emphasized that the RL algorithm has no knowledge of the WEC system. The fact that $P_t(s_c)$ has not reached a value near zero is the reason why random actions are still taken, even though their occurrence has significantly decreased after approximately 750 simulation seconds.

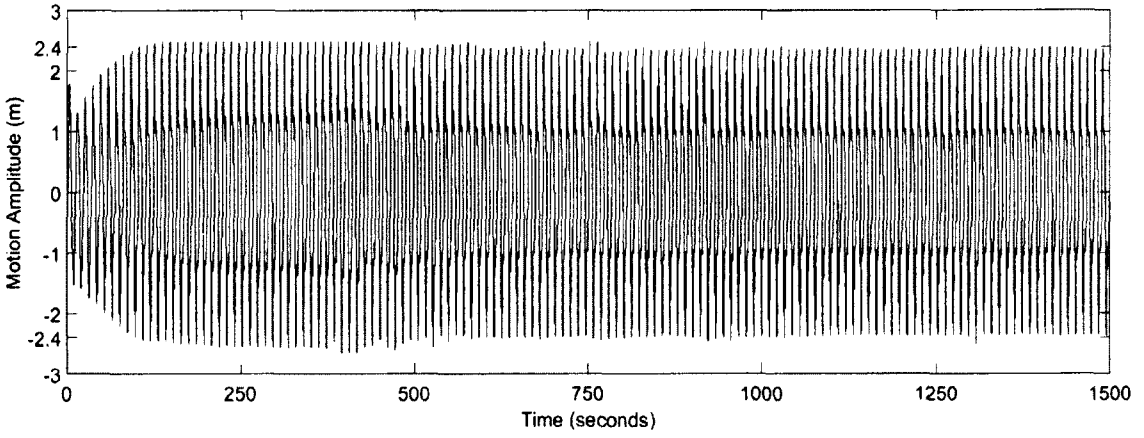

Figure 8.1. RL optimal control policy for wave period of 11 seconds and amplitude of 1.5 m.

A second case with the wave period set equal to 8 seconds and the wave amplitude set equal to 1.0 m is also investigated. The maximum value of the motion amplitude is set equal to 1.15 m. In order to validate the results, the WEC system is run by setting the motor displacement fraction and valve opening time to various constant values and manually finding the pair of values that optimizes the power absorption without violating the motion amplitude constraint. The results are reported in Table 8.2.

f_{dc}, C_{coe}	P_{mg} (kW)	A_{max} (m)
(1.00, 8)	81.2	1.234
(1.00, 10)	79.5	1.175
(0.96, 12)	77.9	1.154
(1.00, 12)	***78.6***	***1.146***
(0.92, 14)	75.7	***1.128***
(0.96, 14)	76.8	***1.120***
(1.00, 14)	77.3	***1.113***

Table 8.2. Optimal control policy for wave period of 8 seconds and amplitude of 1.0 m.

The RL-based controller is switched on again after 375 seconds of simulation time and is able to find the optimal policy within approximately 650 simulation seconds as shown in Figure 8.2.

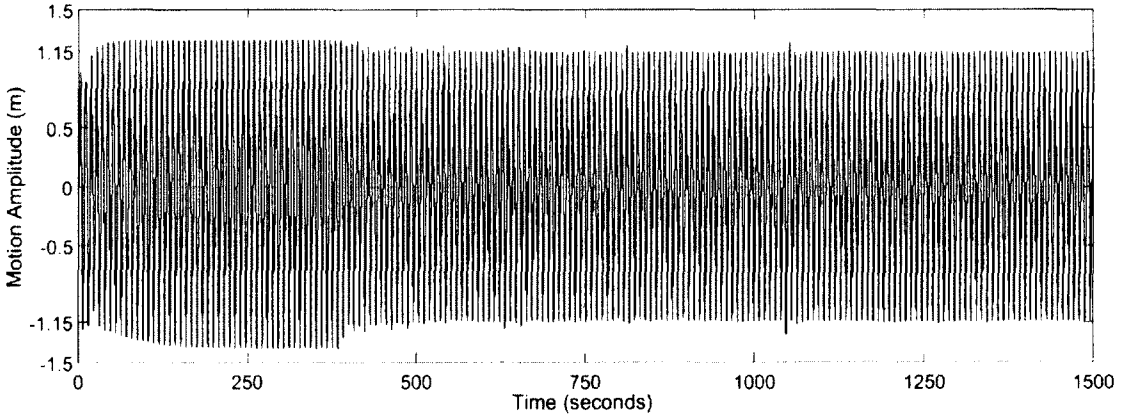

Figure 8.2. RL optimal control policy for wave period of 8 seconds and amplitude of 1.0 m.

8.3.2 Irregular waves

The modified Pierson-Moskowitz spectrum with sea state no. 5 conditions in the North Atlantic is utilized for the training of the RL-based controller. For the purpose of this investigation, the simulation time is set equal to 5,000 seconds and the time step equal to 0.05 seconds. The maximum motion amplitude is constrained to 2m. Ten simulations, each with a different random seed, are performed in order to obtain the optimal policy. The number of states is set equal to 20 and, thus, the wave excitation force is considered to vary between 0 and 1.2 MN. This range is divided in 20 segments of equal length. The action space is defined using the following values:

$$A_1 = \{0.20, 0.25, 0.30, 0.35, 0.40, 0.45, 0.50, 0.55, 0.60\}, A_2 = \{6, 8, 10, 12, 14\}.$$

The results obtained during the final 1,000 seconds of each simulation are utilized in order to calculate the mean generated power and to check whether the motion amplitude constraint is satisfied by the computed optimal policy. The corresponding values are listed in Table 8.3. A plot

of the motion amplitude for rng(5), the run with the highest maximum motion amplitude for the RL-based controller, is shown in Figure 8.3.

RNG	P_{mg} (kW) RL	A_{max} (m) RL	P_{mg} (kW) ($C_{coe} = 10$) ($f_{dc} = 0.60$)	A_{max} (m) ($C_{coe} = 10$) ($f_{dc} = 0.60$)
rng(1)	28.8	1.99	19.8	1.87
rng(2)	33.4	2.12	31.9	2.26
rng(3)	36.6	2.19	33.0	2.52
rng(4)	32.1	2.09	31.8	2.24
rng(5)	29.3	2.26	24.5	2.14
rng(6)	36.1	2.19	33.1	2.46
rng(7)	34.5	2.01	32.2	2.13
rng(8)	32.5	2.02	31.0	2.28
rng(9)	32.2	2.05	30.2	2.35
rng(10)	34.9	2.08	32.2	2.17
AVG	***33.0***	***2.10***	***29.9***	***2.24***
STD. DEV	***2.62***	***0.09***	***4.357***	***0.18***

Table 8.3. Mean generated power and maximum motion amplitude with RL-based controller.

Based on the results reported in Table 8.3, the RL-based controller is able to derive a policy that satisfies the motion amplitude constraint. The optimality of the policy can be evaluated by comparing the average mean absorbed power of the WEC system with the RL-based controller vs. the average mean absorbed power in sea state no. 5 of the WEC system with fixed values of the motor displacement fraction, f_{dc}, and the control coefficient, C_{coe}. Specifically, through a trial-and-error process, it has been determined that $f_{dc} = 0.65$ and $C_{coe} = 10$ provide a good compromise between maximizing the mean generated power and satisfying the motion amplitude constraint. The corresponding results are also listed in Table 8.3.

The t-test is performed on the average mean generated power and average maximum motion amplitude of the data sets in order to evaluate the statistical significance of the results. The p-

value of the t-test for the mean generated power and the maximum motion amplitude is 0.0032 and 0.020, respectively. Therefore, the RL-based has a statistically significant effect on the operation of the WEC system.

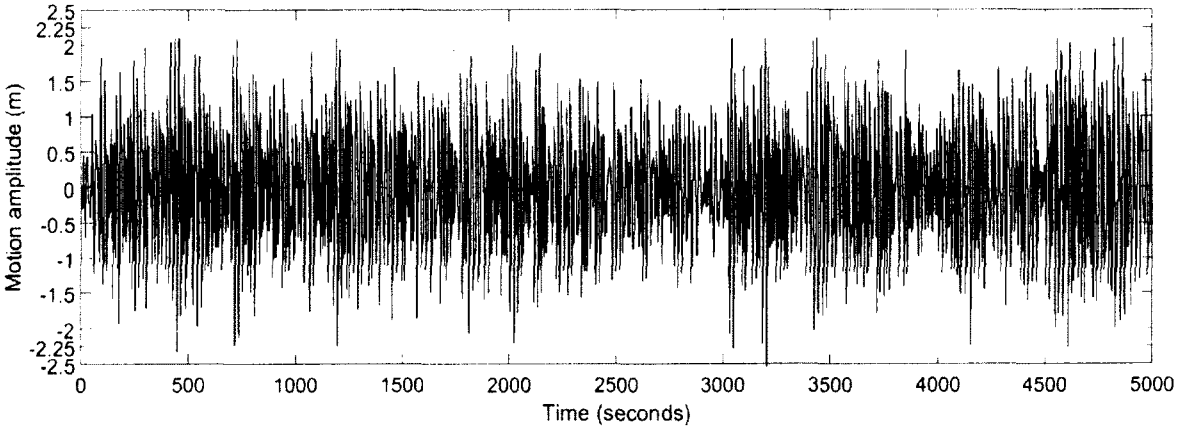

Figure 8.3. WEC system simulation with RL-based controller in sea state no. 5.

8.3.2 RL-based control with predicted wave excitation values

The RL-based controller is evaluated in a realistic scenario, where the future wave excitation force is predicted and is utilized in order to select the f_{dc}, and the C_{coe}, values based on the optimal policy. In this way, the impact of the prediction accuracy of the RL-based controller can be assessed. The PSO-ELM-trained RBF network ensemble is utilized assuming that the wave excitation force is required to be known 10 seconds ahead. Through a trial-and-error process, the optimal number of hidden nodes has been determined to be equal to 20. Wave excitation is derived using the modified Pierson-Moskowitz spectrum with sea state no. 5 conditions. The time series is obtained using a time step of 0.05 for 2,500 seconds. Half of the generated points are used for the training of the network, 20% for validation, and 30% for testing. The trained network is then utilized for the prediction of the wave excitation using the modified P-M spectrum at sea state no. 5 and a different random seed for 5,000 seconds. The mean generated power with perfect knowledge of the future wave excitation computed for the last 1,000 simulation seconds

is equal to 33.2 kW with a maximum motion amplitude of 2.15 m. The corresponding mean generated power using the predicted wave excitation force is 32.7 kW with a maximum motion amplitude of 2.18 m. The difference between the average maximum motion amplitude values is fairly small; a similar observation can be made regarding the difference between the average mean generated power values.

CHAPTER IX

CONCLUSIONS

The software developed in MATLAB® as part of this investigation is successful in controlling effectively the operation of a typical wave energy converter (WEC) system with a single heaving point absorber. Furthermore, this software can be utilized for parametric investigations of WEC systems using heaving spherical point absorbers. Specifically, using the Cummins equation to model the dynamics of the point absorber in the time domain, the motion response parameters such as displacement and velocity of the point absorber in both regular waves and irregular seas can be computed. System level parameters such as mean generated power, power absorption efficiency, and maximum motion amplitude can be estimated for a broad range of sea conditions. The effectiveness of phase control when applied to the point absorber through a hydraulic power take-off (PTO) system is systematically investigated in both regular and irregular waves. Two phase control accumulators are utilized in the hydraulic PTO system.

In regular waves, the mean generated power, the power absorption efficiency, and the maximum motion amplitude are computed in a number of combinations of wave period and amplitude. The results reveal that the mean generated power is not always a monotonic function of wave period for large wave amplitudes. The same results also demonstrate that the optimal value of the mean generated power does not occur at the same opening instant of the phase control accumulator valves, but the optimal opening instant depends on the sea conditions for a given point absorber WEC system. In this way, the power absorption efficiency of the point absorber WEC system can be increased by altering the phase control opening instant. Furthermore, the maximum motion amplitude of the heaving point absorber is taken into consideration as it can affect the structural integrity of the WEC system. The results of the parametric investigation reveal that there is a

trade-off between maximizing the mean generated power and minimizing the maximum motion amplitude, especially for large wave amplitudes

Fully developed irregular seas are modelled using the modified Pierson-Moskowitz (P-M) spectrum. Based on the results of a parametric investigation of different sea states in the North Atlantic, it is demonstrated that by utilizing discrete phase control, a significant increase in the power absorption efficiency can be obtained compared to the WEC system operation without phase control. Given the stochastic nature of irregular seas, a statistical analysis performed as part of this investigation revealed that the observed power increase is statistically significant in most cases. In addition to this, by varying the opening instant of the phase control accumulator valves, the power absorption efficiency can be increased even further. Finally, by properly controlling the volumetric displacement of the hydraulic motor, the generated power can be maximized while satisfying specific motion amplitude constraints. These results clearly show that a heaving point absorber WEC system cannot operate optimally in irregular seas using a single setting of the control parameters.

In the last part of this investigation, the problem of providing an effective phase control strategy that maximizes the average mean generated power subject to motion amplitude constraints is formulated and solved using a Reinforcement Learning (RL) approach based on the Q-learning algorithm. For this purpose, the heaving point absorber WEC system is modelled as a semi-Markov decision process. This RL-based controller chooses actions that determine the opening instant of the phase control accumulator valves and the volumetric displacement of the hydraulic motor. A reward function appropriate for discrete-event systems is successfully incorporated into the Q-learning model. As demonstrated in both regular waves and irregular seas, the RL-based controller is successful in improving the phase-control strategy of the WEC system while satisfying the imposed motion amplitude constraints.

The successful implementation of discrete control requires prediction of the wave excitation force. For this purpose, a PSO-ELM-trained RBF network ensemble is developed and validated in benchmark time-series prediction problems. The wave excitation force is predicted using the RBF network ensemble and the data is inputted to the RL-based controller in order to evaluate the impact of the prediction accuracy on the controller's performance. The results show that the computed mean generated power and maximum motion amplitude values using the RBF network ensemble predictions compare very well with the corresponding values computed assuming perfect knowledge of the future wave excitation.

In the near future, application of RL-based discrete phase control wave farms, i.e., arrays of heaving point absorbers will be investigated. Furthermore, the performance of the RL-based controller and RBF network ensemble in developing irregular seas will be explored. The modeling of the heaving point absorber WEC system using non-linear wave theory is another interesting area of future research. Finally, more research needs to be performed on the effects of other types of discrete control, e.g. declutching, or a combination of discrete control methods.

REFERENCES

[1] Mora, C., Tittensor, D.P., Adl, S., Simpson, A.G.B. and Worm, B. 2011. How Many Species Are There on Earth and in the Ocean? PLoS Biol, 9(8).

[2] Food and Agriculture organization of the United Nations [Online], available at: http://www.fao.org/docrep/w7241e/w7241e06.htm#TopOfPage (last accessed on 7/25/2015).

[3] Donald, H.T. 2008. Biological Thermodynamics. Cambridge: Cambridge University Press.

[4] Singhal, G.S., Renger, G., Sopory, S.K., Irrgang, K.D. and Govindjee. 1999. Editors: Concepts in Photobiology: Photogenesis and Photomorphogenesis. Springer: USA.

[5] Odum, E.P. 1971. Fundamentals of Ecology, 3rd ed. Philadelphia: W.B Saunders Company.

[6] Aubrecht, J.G. 2005. Energy: Physical, Environmental and Social Impact, 3rd ed. Boston: Addison-Wesley.

[7] Shulevitz, J. 2013. The Lethality of Loneliness, The New Republic [Online], available at: http://www.newrepublic.com/article/113176/science-loneliness-how-isolation-can-kill-you (last accessed on 7/25/2015).

[8] Mumovic, D and Santamouris, M. 2009. Editors: A Handbook of Sustainable Building Design and Engineering – An Integrated Approach to Energy, Health and Operational Performance of Buildings. London: Earthscan/James & James Publishers.

[9] United Nations Population Fund (UNFPA). Population Trends [Online], available at: http://www.unfpa.org/pds/trends.htm (last accessed on 7/25/2015).

[10] Oliver, R. 2007. All about Cities and Energy Consumption [Online], available at: http://www.cnn.com/2007/TECH/12/31/eco.cities/index.html?iref=nextin (last accessed on 7/25/2015).

[11] Kramer T.J. 2006. The Traditional Way: The Importance of Wood. International Wood Working Magazine [Online], available at: http://www.kramers.org/whywood.html (last accessed on 7/25/2015).

[12] Biomass Energy Center. 2011. Typical Calorific Values of Fuels [Online], available at: http://www.biomassenergycentre.org.uk/portal/page?_pageid=75,20041&_dad=portal&_schema=PORTAL (last accessed on 7/25/2015).

[13] U.S Energy Information Administration. 2014. What is the U.S Electricity Generation by Energy Source? [Online], available at: http://www.eia.gov/tools/faqs/faq.cfm?id=427&t=3 (last accessed on 7/25/2015).

[14] Krappe, J.H. and Pomorski, K. 2012. Theory of Nuclear Fission. Berlin: Springer-Verlag.

[15] World Nuclear Association. 2014. What is Uranium? [Online], available at: http://www.world-nuclear.org/info/Nuclear-fuel-cycle/introduction/what-is-Uranium--How-Does-it-Work-/ (last accessed on 7/25/2015).

[16] World Nuclear Association. 2010. Heat Values of Various Fuels. [Online], available at: http://www.world-nuclear.org/info/Facts-and-Figures/Heat-values-of-various-fuels/ (last accessed on 7/25/2015).

[17] Sovacool, B.K. 2012. The Avian and Wildlife Costs of Fossil Fuels and Nuclear Power. Journal of Integrative Environmental Sciences vol. 9, no. 4, pp: 255-278.

[18] Annamalai, K and Puri, I.K. 2006. Combustion Science and Engineering. Florida: CRC Press.

[19] U.S Environmental Protection Agency. 1995. Global Warming and Climate Change [Online], available at: http://www.epa.gov/airtrends/aqtrnd95/globwarm.html (last accessed on 7/25/2015).

[20] Walker, S.J. 2006. Three Mile Island: A Nuclear Crisis in Historical Perspective. Oakland: University of California Press.

[21] Mara, W. 2010. The Chernobyl Disaster: Legacy and Impact on the future of Nuclear Energy. Singapore: Times Publishing Group.

[22] Lochbaum, D., Lyman, E., Stranahan, S.Q., The Union of Concerned Scientists. 2014. Fukushima: The Story of a Nuclear Disaster. New York: New Press.

[23] Gloystein, H. 2011. Renewable Energy becoming Cost Competitive, IEA says, Reuters [Online], available at: http://www.geni.org/globalenergy/library/technical-articles/generation/general-renewable-energy/reuters.com/renewable-energy-becoming-cost-competitive-iea-says/index.shtml (last accessed on 7/25/2015).

[24] Barstow, S. et.al. 2008. The Wave Energy Resource. In: Cruz, J. (ed.) Ocean Wave Energy: Current Status and Future Perspective, Berlin: Springer, pp. 93-132.

[25] Ross D. 1995. Power from Sea Waves. Oxford: Oxford University Press.

[26] McCormick, M.E. 1981. Ocean Wave Energy Conversion, New York: Wiley Publications.

[27] Bureau of Ocean Energy Management. Ocean Wave Energy, [Online], available at: http://www.boem.gov/Renewable-Energy-Program/Renewable-Energy-Guide/Ocean-Wave-Energy.aspx (last accessed on 7/25/2015).

[28] Falcao, A.F. de O. 2010. Wave Energy Utilization: A Review of the Technologies, Renewable and Sustainable Energy Review, 14, pp. 899-918.

[29] Kishore, S., Snyder, L. and Pradhan, P. 2013. Electricity from Ocean Wave Energy: Technologies, Opportunities and Challenges. IEEE Smart Grid Newsletter.

[30] Thomas, G. 2008. The Theory behind the Conversion of Ocean Wave Energy. A Review. In: Cruz, J. (ed.) Ocean Wave Energy: Current Status and Future Perspectives, Berlin: Springer, pp. 41-89.

[31] Reedsport OPT wave park. 2012. Ocean Power Technologies, [Online], available at: http://www.power-technology.com/projects/reedsportwavepowerst (last accessed on 7/25/2015).

[32] Stahl A. 1892. The Utilization of the Power of Ocean Waves. Trans. Am Soc Mech Eng; 13:438-506.

[33] Falnes, J. 2007. A Review of Wave-Energy Extraction, Marine Structures, 20, pp. 185-201.

[34] Falnes, J. 1994. Small is Beautiful: How to Make Wave Energy Economic, Proceedings of the 1993 European Wave Energy Symposium, pp. 367-372.

[35] Falnes, J. 2002. Ocean Waves and Oscillating Systems. Cambridge: Cambridge University Press.

[36] Babarit, A. and Clement, A.H. 2006. Optimal Latching Control of a Wave Energy Device in Regular and Irregular Waves, Applied Ocean Research, 28 (2), pp. 77-91.

[37] Budal, K. and Falnes, J. 1980. Interacting Point Absorbers with Controlled Motion. In: Count, B. (ed.) Power from Sea Waves, London: Academic Press, pp. 381-399.

[38] Ringwood, J.V., Bacelli, G. and Fusco, F. 2014. Energy-maximizing Control of Wave-Energy Converters, Control Systems, IEEE, 34(5), pp. 30-55.

[39] Schoen, M.P., Hals, J. and Moan, T. 2011. Wave Prediction and Robust Control of Heaving Wave Energy Devices for Irregular Waves, IEEE Transactions on Energy Conversation, 26 (2), pp. 627-637.

[40] Falnes, J. and Budal, K. 1978. Wave Power Conversion by Point Absorbers, Norwegian Maritime Research, 6(4), pp. 2-11.

[41] Ricci, R., Lopez, J., Santos, M., Ruiz-Minguela, P., Villate, J.L., Salcedo, F. and Falcao, A.F. de O. 2011. Control Strategies for a Wave Energy Converter Connected to a Hydraulic Power Take-off. IET Renewable Power Generation, 5(3), pp. 234-244.

[42] Eidsmoen, H. 1996. Simulation of a Tight-moored Amplitude-limited Heaving-buoy Wave-Energy Converter with Phase Control, available at: http://folk.ntnu.no/falnes/web_arkiv/InstFysikk/simconve.pdf (last accessed on 7/25/2015).

[43] Eidsmoen, H. 1998. Tight-moored Amplitude-limited Heaving Buoy Wave Energy Converter with Phase Control. Applied Ocean Research, 20, pp. 157-161.

[44] Fusco, F. and Ringwood, J.V. 2010. Short-term Wave Forecasting for Real-Time Control of Wave Energy Converters, IEEE Transactions on Sustainable Energy, 1(2), pp. 99-106.

[45] Cruz, J. editor. 2008. Ocean Wave Energy: Current Status and Future Perspectives, Berlin: Springer.

[46] Hulme, H. 1982. The Wave Forces Acting on a Floating Hemisphere undergoing Forced Periodic Oscillations. Journal of Fluid Mechanics, 121, pp. 443-463.

[47] Budal, K and Falnes, J. 1975. A Resonant Point Absorber of Ocean-wave Power, Nature, 257, 478-479.

[48] Mei, C.C. 1976. Power Extraction from Water Waves, Journal of Ship Research, 20, 63-66.

[49] Evans, D. V. 1976. A Theory for Wave -power Absorption by Oscillating Bodies, Journal of Fluid Mechanics, 77, 1-25.

[50] Newman, J.N. 1976. The Interaction of Stationary Vessels with Regular waves. In: Proceedings of 11th Symposium on Naval Hydrodynamics, pp. 491-501.

[51] Jefferys, E.R. 1980. In: Count B, editor. Power from Sea Waves. London: Academic Press, pp. 413-438.

[52] Cummins, W. 1962. The Impulse Response Function and Ship Motions. Technical Report No. 1961, Schiffstechnik, 9, pp. 101-109.

[53] Budal, K. 1977. Theory for Absorption of Wave Power by a System of Interacting Bodies, Journal of Ship Research, 21, 248-253.

[54] Evans, D.V. Some Theoretical Aspects of Three-dimensional Wave energy Absorbers. In: Proceedings of 1st symposium on Ocean Wave Energy Utilization, pp. 77-113.

[55] Faltinsen, O.M. 1990. Sea Loads on Ships and Offshore Structures. Cambridge: Cambridge University Press.

[56] National Oceanic and Atmospheric Administration's National Data Buoy Center [Online], available at: http://www.ndbc.noaa.gov/ (last accessed on 7/25/2015).

[57] Michel, W.H. 1999. Sea Spectra Revisited, Marine Technology, 36 (4), pp. 211-227.

[58] Lee, W.T., Bales, W.L. and Sowby, S.E. 1985. Standardized Wind and Wave Environments for North Pacific Ocean Areas. R/SPD-0919-02, DTNSRDC, Washington D.C.

[59] Kaelbling, P.L., Littman, L.M and Moore, W.A. 1996. Reinforcement Learning: A Survey, Journal of Artificial Intelligence Research, 4, pp. 237-285.

[60] Sutton, S.R and Barto, G.A. 1998. Reinforcement Learning: An Introduction. Cambridge: MIT Press.

[61] Falcao, A.F. de O. 2007. Modelling and Control of Oscillating-body Wave Energy Converters with Hydraulic Power Take-off and Gas Accumulator. Ocean Engineering, 34, pp. 2021-2032.

[62] Lopes, M.F.P., Hals, J., Gomes, R.P.F, Moan, T., Gato, L.M.C. and Falcao, A.F. de O. 2009. Experimental and numerical Investigation of Non-predictive Phase Control Strategies for a Point-absorbing Wave Energy Converter. Ocean Engineering, 36, pp. 386-402.

[63] Budal, K. and Falnes, J. 1982. Wave Power Conversion by Point Absorbers: a Norwegian Project. International Journal of Ambient Energy, 3, pp. 59-67.

[64] Fusco, F. and Ringwood, J. 2012. A Study of Prediction Requirements in Real-time Control of Wave Energy Converters. IEEE Transactions in Sustainable Energy, 3(1), pp. 176-184.

[65] Newman, J. 1977. Marine Hydrodynamics. Cambridge: Cambridge University Press.

[66] Count, B, editor. 1987. Power from Sea Waves. London: Academic Press.

[67] Hals, J., Taghipour, R. and Moan, T. 2007. Dynamics of a Force-compensated Two-body Wave Energy Converter in Heave with Hydraulic Power Take-off subject to Phase Control. Proceedings of the 7th European Wave and Tidal Energy Conference, Porto, Portugal.

[68] Falcao, A.F. de O. 2008. Phase Control through Load Control of Oscillating-body Wave Energy Converters with Hydraulic PTO System. Ocean Engineering, 35, pp. 358-366.

[69] Jefferys, E.R. 1980. Device characterization. In: Count, B. (Ed.), Power from Sea Waves. London: Academic Press.

[70] Kurniawan, A., Hals, J. and Moan, T., 2011. Assessment of Time-Domain Models of Wave Energy Conversion Systems. Proceedings of the 9th European Wave and Tidal energy conference, EWTEC 2011.

[71] Tucker, M.J., Challenor, P.G and Carter, D.J.T. 1984. Numerical Simulation of a Random sea: a Common Error and its Effect upon Wave Group Statistics. Applied Ocean Research, Vol. 6, No.2, pp. 118-122.

[72] Koopmans, L.H. 1974. The Spectral Analysis of Time Series. Academic Press.

[73] Borgnakke, C. and Sonntag, R.E. 2009. Fundamentals of Thermodynamics. Hoboken: John Wiley & Sons. 7th edition.

[74] Bailey, H., Ortiz, P.J., Robertson, B., Buckham, J.B. and Nicoll, S.R. 2014. A Methodology for Wave-to-wire Simulations. Proceedings of the 2nd Marine Energy Technology Symposium, METS2014, Seattle, WA, USA.

[75] Michel, W.H. 1968. Sea Spectra Simplified, Marine Technology, pp. 17-30.

[76] Hafner, R and Riedmiller, M. 2011. Reinforcement Learning in Feedback Control, Machine Learning, 84, pp. 137-169.

[77] Watkins, C.J.C.H. 1989. Learning from Delayed Rewards, Ph.D. thesis, Cambridge University.

[78] Watkins, C.J.C.H and Dayan, P. 1992. Q-learning, Machine Learning, 8, pp. 279-292.

[79] Anderson, W.C., Hittle, C.D., Katz, D.A. and Kretchmar, R.M. 1997. Synthesis of Reinforcement Learning, Neural Networks and PI Control Applied to a Simulated Heating Coil, Artificial Intelligence in Engineering, 11, pp. 421-429.

[80] Underwood, D. M. and Crawford, R.R. 1991. Dynamic Nonlinear Modeling of a Hot-water-to-air Heat Exchanger for Control Applications, ASHRAE Transactions, 97(1), pp. 149-155.

[81] Huang, G.B., Zhu, Q.Y. and Siew, C.K. 2006. Extreme Learning Machine: Theory and Applications, Neurocomputing, 70(1-3), pp. 489-501.

[82] Kennedy, J. and Eberhart, R.C. 1995. Particle Swarm Optimization. In: Proceedings of the IEEE International Conference on Neural Networks, Perth, Australia, IV, pp. 1942-1948.

[83] Wang Y., Cao F. and Yuan, Y. 2011. A Study on Effectiveness of Extreme Learning Machine, Neurocomputing, 74(16), pp. 2483-2490.

[84] Huang, G.B. and Chen, L. 2007. Convex Incremental Extreme Learning Machine, Neurocomputing, 70(16-18), pp. 3056-3062.

[85] Feng, G., Huang, G.B., Lin, Q. and Gay, R. 2009. Error Minimized Extreme Learning Machine with Growth of Hidden Nodes and Incremental Learning, IEEE Transactions Neural Networks, 20(8), pp. 1352-1357.

[86] Zhu, Q.Y., Qin, A.K., Suganthan, P.N. and Huang, G.B. 2005. Evolutionary Extreme Learning Machine, Pattern Recognition, 38(10), pp. 1759-1763.

[87] Broomhead, D.S. and Lowe, D. 1988. Multivariate Functional Interpolation and Adaptive Networks, Complex Systems, 2, pp. 321-355.

[88] Poggio, T. and Girosi, F. 1990. Networks for Approximation and Learning, Proceedings of IEEE, 78(9), pp. 1481-1497.

[89] Harpham, C. and Dawson, C.W. 2006. The Effect of Different Basis Functions on a Radial Basis Function Network for Time Series Prediction: A Comparative Study, Neurocomputing, 69(16-18), pp. 2161-2170.

[90] Huang, G.B. and Siew, C.K. 2005. Extreme Learning Machine with Randomly Assigned RBF Kernels, International Journal of Information Technology, 11(1), pp. 16-24.

[91] Mendes, R., Cortez, P., Rocha, M. and Neves, J. 2002. Particle swarms for Feedforward Neural Network Training, In: Proceedings of the 2002 International Joint Conference on Neural Networks, Honolulu, Hawaii, pp. 1895-1899.

[92] Han, F., Yao, H.F. and Ling, Q.H. 2013. An Improved Evolutionary Extreme Learning Machine based on Particle Swarm Optimization, Neurocomputing, 116, pp. 87-93.

[93] Mak, M.W. and Cho, K.W. 1998. Genetic Evolution of Radial Basis Function Centers for Pattern Classification. In: Proceedings of the 1998 IEEE International Joint Conference on Neural Networks, Anchorage, Alaska, pp. 669-673.

[94] Feng, H.M. 2006. Self-generation RBFNs Using Evolutional PSO learning, Neurocomputing, 70(1-3), pp. 241-251.

[95] Gonzalez, J., Rojas, I., Ortega, J., Pomares, H., Fernandez, F.J. and Diaz AF. 2003. Multi-objective Evolutionary Optimization of the Size, Shape, and Position Parameters of Radial Basis Function Networks for Function Approximation, IEEE Transactions Neural Networks, 14(6), pp. 1478-1495.

[96] Rocha, M., Cortez, P. and Neves, J. 2007. Evolution of Neural Networks for Classification and Regression, Neurocomputing, 70(16-18), pp. 2809-2816.

[97] Du, H. and Zhang, N. 2008. Time Series Prediction using Evolving Radial Basis Function Networks with New Encoding Scheme, Neurocomputing, 71(7-9), pp. 1388-1400.

[98] Kokshenev, I. and Braga, A.P. 2008. A Multi-objective Approach to RBF Network Learning, Neurocomputing, 71(7-9), pp. 1203-1209.

[99] Kondo, N., Hatanaka, T. and Uosaki, K. 2006. Pattern Classification by Evolutionary RBF Networks Ensemble based on Multi-objective Optimization, In: Proceedings of the 2006 International Joint Conference on Neural Networks, Vancouver, British Columbia, pp. 2919-2925.

[100] Jin, Y., Okabe, T. and Sendhoff, B. 2006. Neural Network Regularization and Ensembling using Multi-objective Evolutionary Algorithms, In: Proceedings of the 2004 IEEE Congress on Evolutionary Computation, Portland, Oregon, pp. 1-8.

[101] Chandra, A. and Yao, X. 2006. Evolving Hybrid Ensembles of Learning Machines for Better Generalization, Neurocomputing, 69(7-9), pp. 686-700.

[102] Krogh, A. and Vedelsby, J. 1995. Neural Network Ensembles, Cross Validation, and Active Learning, Advances in Neural Information Processing Systems, 7, pp. 231-238.

[103] Eberhart, R.C., Simpson, P.K. and Dobbins, R.W. 1995. Computational Intelligence PC Tools. Boston: Academic Press.

[104] Hardy, R.L. 1971. Multiquadric Equation of Topography and other Irregular Surfaces, Journal of Geophysical Research, 76(8), pp. 1905-1915.

[105] Hastie, T., Tibshirani, R. and Friedman, J. 2009. The Elements of Statistical Learning. New York: Springer Science plus Business Media, 2nd edition, pp. 212-214.

[106] Moody, J.E. and Darken, C. 1989. Learning with Localized Receptive Fields, In: Touretzky D, Hinton G, Sejnowski T (eds) Proceedings of the Connectionist Models Summer School, San Mateo, California, Morgan Kaufmann, pp. 133-143.

[107] Rao, C.R. and Mitra, S.K. 1971. Generalized Inverse of Matrices and its Applications. New York: Wiley publications.

[108] Bartlett, P.L. 1998. The Sample Complexity of Pattern Classification with Neural Networks: the Size of the Weights is More Important than the Size of the Network, IEEE Transactions on Information Theory, 44(2), pp. 522-536.

[109] Kennedy, J. and Eberhart, R.C. 1995. Particle Swarm Optimization, In: Proceedings of the 1995 IEEE International Conference on Neural Networks, Perth, Australia, pp. 1942-1948.

[110] Clerc, M. and Kennedy, J. 2002. The Particle Swarm Explosion, Stability, and Convergence in a Multi-dimensional Complex Space, IEEE Transactions on Evolutionary Computing, 6(1), pp. 58-73.

[111] Eberhart, R. and Shi, Y. 2000. Comparing Inertia Weights and Constriction Factors in Particle Swarm Optimization, In: Proceedings of the 2000 IEEE Congress on Evolutionary Computation, San Diego, California, pp. 84-88.

[112] Chauvenet, W. 1863. A Manual of Spherical and Practical Astronomy. Philadelphia: Lippincott, Vol. 2, 1st edition.

[113] Coleman, H.W. and Steele, W.G. 2002. Experimentation and Uncertainty Analysis for Engineers. New York: Wiley publications, 2nd edition.

[114] Bache, K. and Lichman, M. 2013. UCI Machine Learning Repository, University of California, School of Information and Computer Science, Irvine, CA, 2013, http://archive.ics.uci.edu/ml (last accessed on 7/25/2015).

[115] Cortez, P., Cerdeira, A., Almeida, F., Matos, T. and Reis, J. 2009. Modeling Wine Preferences by Data Mining from Physiochemical Properties, Decision Support Systems, 47(4), pp. 547-553.

[116] Cortez, P. and Morais, A. 2007. Data Mining Approach to Predict Forest Fires using Meteorological Data, In: Neves J, Santos MF, Machado J (eds) New trends in artificial intelligence, Proceedings of the 13th EPIA, Portuguese Conference on Artificial Intelligence, Guimaraes, Portugal, pp. 512-523.

[117] Yeh, I.C. 1998. Modeling of Strength of High Performance Concrete using Artificial Neural Networks, Cement Concrete Research, 28(12), pp. 1797-1808.

[118] Yeh, I.C .2007. Modeling Slump Flow of Concrete using Second-order Regressions and Artificial Neural Networks, Cement Concrete Composites, 29(6), pp. 474-480.

[119] Box, G.E.P. and Jenkins, G.M. 1976. Time Series Analysis: Forecasting and Control. San Francisco: Holden-Day, Revised edition.

[120] Mackey, M.C. and Glass, L. 1977. Oscillation and Chaos in Physiological Control Systems, Science, 197(4300), pp. 287-289.

[121] Welch, B.L. 1947. The Generalization of 'Student's' problem when Several Different Population Variances are Involved, Biometrika, 34(1-2), pp. 28-35.

[122] Hall, M., Frank, E., Holmes, G., Pfahringer, B., Reutemann, P. and Witten, I.H. 2009. The WEKA Data Mining Software: an update. ACM SIGKDD Exploration Newsletter, 11(1), pp. 10-18.

[123] Aha, D. and Kibler, D. 1991. Instance-based Learning Algorithms, Machine Learning, 6, pp. 37-66.

[124] Quinlan, R.J. 1992. Learning with Continuous Classes, In: Proceedings of the 5th Australian Joint Conference on Artificial Intelligence, Singapore, pp. 343-348.

[125] Crites, R. H. and Barto, A. G. 1996. Improving elevator performance using reinforcement learning. In: Advances in Neural Information Processing Systems, 8, pp. 1017-1023.

[126] Arhan, M., and Ezraty, R. 1978. Statistical relations between successive wave heights. Oceanologica Acta, 1(2), pp. 151-158.

[127] Kimura, A. 1980. Statistical properties of random wave groups. In: Proceedings of the 17th Coastal Engineering Conference, Sydney, 3, pp. 2955-2973.

APPENDICES

APPENDIX – A

CODE FOR MOTION RESPONSE OF POINT ABSORBER WEC SYSTEM

```
% code developed by Miltos Kotinis and Praveen Malali - last updated on
8/1/2015
clear;
% characteristics of sea states in North Atlantic
% mean significant wave height, most probable modal wave period, %
probability of sea state
seastch = {0.30, 7.50, 0.0680; ... % Sea State no. 2
           0.88, 7.50, 0.2370; ... % Sea State no. 3
           1.88, 8.80, 0.2780; ... % Sea State no. 4
           3.25, 9.70, 0.2064; ... % Sea State no. 5
           5.00, 12.4, 0.1315; ... % Sea State no. 6
           7.50, 15.0, 0.0605}; ...% Sea State no. 7
global m_b; global m_inf; global k_hs; global inx; global sol_tmp;
global control_coef_1;
global tm_c; global omega_d; global dt; global control_m; global
t_span; global conv_inx;
global k_rad_0; global k_rad_t; global pcf_h; global pcf_kr; global
w_exc;
global q_m; global hydro_f; global gen_speed; global f_peak;
global fpto; global hpw; global gpw; global t_latch; global torqm;
global omega_m;
global pca1; global pca2; global ppc1; global ppc2; global p_hp; global
p_lp;
global vpc1; global vpc2; global v_lp; global v_hp; global vca1; global
vca2;

tic();
% input section starts here %%%%%%%%%%%%%%%%%%%%%%%%%%%%%%%%
grv = 9.81; % acceleration of gravity in m/s^2
rho = 1025; % water density in kg/m^3
wave_type = 0; % 0 for regular waves, 1 for irregular waves
rng(1); % random number generator seed
if wave_type == 0
  wave_amp = 1.0; % wave amplitude in m
  wave_per = 8; % wave period in s
elseif wave_type == 1
   idst = 4; % sea state ID
end
control_m = 1; % 0 for no phase control, 1 for phase control
control_coef_1 = 10; % fraction of the natural heave period before the
wave excitation peak value
%%%%%%%%%%%%%%%%%%%%%%%%%%%%%%
fpto = 0;
gen_speed = 0;
rds = 4; % sphere radius in m
t_sim = 500; % simulation time in seconds
dt = 0.05; % time step in s
% input section ends here %%%%%%%%%%%%%%%%%%%%%%%%%%%%%%%%
% Heave added mass and damping data obtained from the paper "The wave
forces acting on a floating hemisphere undergoing forced periodic
oscillations,"
```

```
% authored by A. Hulme, which was published in the Journal of Fluid
Mechanics, vol. 121, pp. 443-463, in 1982.
omega_add_h = [0, 0.8310; 0.2236068, 0.8764; 0.3162278, 0.8627;
0.4472136, 0.7938; 0.5477226, 0.7157; 0.6324555, 0.6452; 0.7071068,
0.5861; 0.7745967, 0.5381; ...
                0.8366600, 0.4999; 0.8944272, 0.4698; 0.9486833, 0.4464;
1.0, 0.4284; 1.0954451, 0.4047; 1.1832160, 0.3924; 1.2649111, 0.3871;
1.3416408,0.3864; ...
                1.4142136, 0.3884; 1.5811388, 0.3988; 1.7320508, 0.4111;
2.0, 0.4322; 2.2360680, 0.4471; 2.4494897, 0.4574; 2.6457513, 0.4647;
2.8284271, 0.4700; ...
                3.0, 0.4740; 3.1622777, 0.4771; 5.0, 0.5];
pcf_am = pchip(omega_add_h(:,1),omega_add_h(:,2)); % compute the
piecewise cubic Hermite interpolating polynomial coefficients for the
heave added mass coefficient
omega_dmp_h = [0, 0; 0.2236068, 0.1036; 0.3162278, 0.1816; 0.4472136,
0.2793; 0.5477226, 0.3254; 0.6324555, 0.3410; 0.7071068, 0.3391;
0.7745967, 0.3271; ...
                0.8366600, 0.3098; 0.8944272, 0.2899; 0.9486833, 0.2691;
1.0, 0.2484; 1.0954451, 0.2096; 1.1832160, 0.1756; 1.2649111, 0.1469;
1.3416408,0.1229; ...
                1.4142136, 0.1031; 1.5811388, 0.0674; 1.7320508, 0.0452;
2.0, 0.0219; 2.2360680, 0.0116; 2.4494897, 0.0066; 2.6457513, 0.0040;
2.8284271, 0.0026; ...
                3.0, 0.0017; 3.1622777, 0.0012; 5.0, 0.0];
pcf_h = pchip(omega_dmp_h(:,1),omega_dmp_h(:,2)); % compute the
piecewise cubic Hermite interpolating polynomial coefficients for the
heave damping coefficient
m_b = rho*(2/3)*pi*rds^3; % mass of the hemispherical buoy
if wave_type == 0
  m_inf = ppval(pcf_am,sqrt(rds/grv)*(2*pi/wave_per))*m_b; % heave
added mass of the buoy at the wave frequency
elseif wave_type == 1
  m_inf = omega_add_h(end,2)*m_b; % heave added mass of the buoy at
infinite frequency
end
k_hs = rho*grv*pi*rds^2; % hydrostatic stiffness of the heaving buoy
omega_d = sqrt(k_hs/(m_b+m_inf)); % heave natural resonance frequency
(undamped and uncoupled)
t_span = 0:dt:t_sim; % the instances where the response will be
calculated
tm_c = 0:dt/2:t_sim; % computation points for R-K4
n_pts = 2*t_sim/dt; % number of points in the time series (t=0 is not
included)
inx = 1; sol_tmp = zeros(size(tm_c,2),2); k_rad_t =
zeros(1,size(tm_c,2));
f_irf_0 = @(y) y.*ppval(pcf_h,sqrt(rds/grv)*y); k_rad_0 =
m_b*(2/pi)*quadgk(f_irf_0,0,5);  % compute the memory kernel at time
zero
while tm_c(1,inx) <= 15 % compute the memory kernel for heave at the
specified set of discrete points
  f_irf_t = @(y) y.*ppval(pcf_h,sqrt(rds/grv)*y).*cos(y*tm_c(1,inx));
  k_rad_t(1,inx) = m_b*(2/pi)*quadgk(f_irf_t,0,5);
  inx = inx+1;
end
conv_inx = inx;
```

```
inx = 1; pcf_kr = pchip(tm_c,k_rad_t); % compute the piecewise cubic
Hermite interpolating polynomial coefficients for the memory kernel for
heave
if wave_type == 0
  b_rad_h =
m_b*(2*pi/wave_per)*ppval(pcf_h,sqrt(rds/grv)*(2*pi/wave_per)); %
compute the radiation damping of the heaving sphere
  f_amp_h = wave_amp*sqrt(rho*grv^3*2*b_rad_h/(2*pi/wave_per)^3); %
compute the wave excitation force amplitude of the heaving sphere
  w_exc = f_amp_h*sin((2*pi/wave_per)*tm_c)'; % compute the wave
excitation force of the heaving sphere
elseif wave_type  == 1
  dw = 4*pi/t_sim; % frequency interval in rad/s - wave series repeats
itself after 2*pi/dw seconds
  w = dw:dw:(n_pts/2)*dw; % frequency range in rad/sec
  w0 = (2*pi)/seastch{idst,2}; % modal (peak) frequency
  f_e_sq = abs(2*rho*m_b*(grv^3)*ppval(pcf_h,sqrt(rds/grv)*w)./w.^2); %
compute the square of the excitation force amplitude per unit incident
wave using the Haskind relation
  s = (((1.25/4)*w0^4*seastch{idst,1}^2)./w.^(5)).*exp(-
1.25*(w0./w).^4); % compute the spectral density of the modified P-M
spectrum for the selected sea state
  a_n = zeros(1,n_pts/2+1); b_n = zeros(1,n_pts/2+1);% initialize the
Fourier series coefficients a_n and b_n with zero values
  a_n(1,2:n_pts/2+1) = sqrt(dw*(f_e_sq.*s)).*randn(1,n_pts/2); %
compute a_n and b_n assuming that they are independent random variables
chosen from
  b_n(1,2:n_pts/2+1) = sqrt(dw*(f_e_sq.*s)).*randn(1,n_pts/2); % a
Gaussian distribution with zero mean and common variance S(w_n)*dw
  c_n = complex(n_pts*a_n/2,-n_pts*b_n/2); c_n(1,n_pts/2+2:n_pts+1) =
complex(n_pts*fliplr(a_n(2:n_pts/2+1))/2,n_pts*fliplr(b_n(2:n_pts/2+1))
/2);
  w_exc = real(ifft(c_n))'; % use inverse Fast Fourier transform to
compute the wave excitation force in the time domain
end
pk = 0; zcr = 0; f_peak = zeros(1,1); % find the wave excitation peaks
for i=3:size(w_exc,1)-1
  if abs(w_exc(i))>abs(w_exc(i-1)) && abs(w_exc(i))>=abs(w_exc(i+1)) %
find the extreme values of the wave excitation
    pk = pk+1; f_peak(pk,1) = i;
  end
end
xp_h = feval('ode4',@Buoy_heave,t_span,[0;0]); % specify initial
conditions and run simulation for heaving sphere
figure(1);  plot(t_span,xp_h(:,1)); % plot the displacement of the
heaving sphere
figure(2);  plot(t_span,xp_h(:,2),tm_c,w_exc/1000000); % plot the
velocity of the heaving sphere and the wave excitation (in MN)

if wave_type == 0
   avpw = (rho*2*rds*grv^2/(32*pi))*(wave_per)*(2*wave_amp)^2 %
available power of regular waves
elseif wave_type ==1
   a_pm = ((0.3125*(w0^4)*seastch{idst,1}^2)/(2*pi)^4);
   int_pm = @(y) (y.^4).*exp((-(1.25*w0^4)/(2*pi)^4)*y.^4);
```

```
   avpw = ((rho*grv^2)*rds*a_pm*quadgk(int_pm,0,100))/(2*pi) %
available power of the given sea state with the modified P-M spectrum
end
mgpw = mean(gpw(ceil(0.75*t_sim/dt):end,:)) % average value of the mean
generated power
eff = 100*(mgpw/avpw) % power absorption efficiency
amp_min = min(xp_h((0.75*t_sim/dt):end,1)); % maximum motion amplitude
(trough)
amp_max = max(xp_h((0.75*t_sim/dt):end,1)); % maximum motion amplitude
(crest)
amp_max_abs = max(abs(amp_min),abs(amp_max)) % maximum motion amplitude
cgpw = cumsum(gpw); % cumulative mean generated power
figure(3); plot(t_span,cgpw);
toc();
```

APPENDIX – B

RUNGE-KUTTA (R-K4) SOLVER FOR ODE

```
function Y = ode4(odefun,tspan,y0,varargin)
%ODE4  The solver implements the classical Runge-Kutta method of order
4

global inx; global sol_tmp; global f_peak; global t_latch; global gpw;
global control_coef_1; global k_rad_0; global conv; global control_m;
global omega_d; global tm_c; global dt; global gen_speed; global fpto;
global w_exc; global k_hs; global q_m; global f_pto; global mdf;
global hydro_f; global torqm; global torqg; global omega_m;
global p_hp; global p_lp; global pca1; global pca2;
global v_lp; global v_hp; global vca1; global vca2;
global ppc1; global ppc2; global vpc1; global vpc2;

h = diff(tspan);
y0 = y0(:);   % Make a column vector
neq = length(y0); N = length(tspan); Y = zeros(neq,N); F =
zeros(neq,4);
Y(:,1) = y0;
p_lp = zeros(N,1); p_hp = zeros(N,1); v_lp = zeros(N,1); v_hp =
zeros(N,1);
pca1 = zeros(N,1); pca2 = zeros(N,1); vca1 = zeros(N,1); vca2 =
zeros(N,1);
ppc1 = zeros(N,1); ppc2 = zeros(N,1); vpc1 = zeros(N,1); vpc2 =
zeros(N,1);
f_pto = zeros(N,1); hydro_f = zeros(N,1); gpw = zeros(N,1);
torqm = zeros(N,1); torqg = 30*ones(N,1); omega_m = zeros(N,1);
q_m = zeros(N,1);

gamma = 1.4; % isentropic process, value for nitrogen
rho_o = 850; % density of oil in kg/m^3
mdf = 0.92; % fraction of maximum volumetric motor displacement
ul = 1;
% initial values
vca1(1) = 0.05; % in m^3
vca2(1) = 0.05; % in m^3
vpc1(1) = 0.5; % in m^3
vpc2(1) = 0.5; % in m^3
v_lp(1) = 1; % in m^3
v_hp(1) = 2; % in m^3
p_lp(1) = 10*10^6; % pressure in LP accumulator in N/m^2
p_hp(1) = 10*10^6; % pressure in HP accumulator in N/m^2
pca1(1) = 10*10^6; % pressure in compressibility accumulator #1 in
N/m^2
pca2(1) = 10*10^6; % pressure in compressibility accumulator #2 in
N/m^2
ppc1(1) = 10*10^6; % pressure in phase control accumulator #1 in N/m^2
ppc2(1) = 10*10^6; % pressure in phase control accumulator #2 in N/m^2

% constants
sp = 0.05; % piston surface area in m^2
% hydraulic motor data
```

```
speed_max = 3000; % maximum continuous speed in rev/min
max_dhm = 165*10^-6; % in m^3 per rev
torqm_max = 659; % continuous output torque in N*m
omega_m(1) = 2*pi*(speed_max/2)/60; % angular velocity in radians per
second
omega_max = 2*pi*speed_max/60; % maximum angular velocity in radians
per second
% Control parameters
cv = 0.95;
cc = 0.95;
av = 0.002; % m^2
ac = 0.002; % m^2
Jr = 7.5; % kg*s^2, combined rotational inertia of motor, generator,
and shaft
openv = 1;
for i = 2:N
  ti = tspan(i-1);
  hi = h(i-1);
  yi = Y(:,i-1);
  F(:,1) = feval(odefun,ti,yi); inx = inx+1;
  F(:,2) = feval(odefun,ti+0.5*hi,yi+0.5*hi*F(:,1),varargin{:});
  sol_tmp(inx,:) = F(:,2)';
  F(:,3) = feval(odefun,ti+0.5*hi,yi+0.5*hi*F(:,2),varargin{:});
  sol_tmp(inx,:) = F(:,3)'; inx = inx+1;
  F(:,4) = feval(odefun,tspan(i),yi+hi*F(:,3),varargin{:});
  Y(:,i) = yi + (hi/6)*(F(:,1) + 2*F(:,2) + 2*F(:,3) + F(:,4));
  sol_tmp(inx,:) = Y(:,i)';
  hydro_f(i) = -k_hs*Y(1,i)-(0.5*(tm_c(1,inx)-tm_c(1,inx-
1))*k_rad_0+conv)*Y(2,i)+w_exc(inx,1); % hydrodynamic force

  vca1(i) = vca1(i-1)+dt*(-
sp*Y(2,i)+ul*cv*av*sqrt((2/rho_o)*max((pca1(i-1)-p_hp(i-1)),0)) -
ul*cv*av*sqrt((2/rho_o)*max((p_lp(i-1)-pca1(i-1)),0)) - (ul-
1)*cc*ac*sqrt((2/rho_o)*abs(pca1(i-1)-ppc1(i-1)))*sign(pca1(i-1)-
ppc1(i-1)));
  vca2(i) = vca2(i-
1)+dt*(sp*Y(2,i)+ul*cv*av*sqrt((2/rho_o)*max((pca2(i-1)-p_hp(i-1)),0))
- ul*cv*av*sqrt((2/rho_o)*max((p_lp(i-1)-pca2(i-1)),0)) - (ul-
1)*cc*ac*sqrt((2/rho_o)*abs(pca2(i-1)-ppc2(i-1)))*sign(pca2(i-1)-
ppc2(i-1)));
  v_lp(i) = v_lp(i-1)+dt*(ul*cv*av*sqrt((2/rho_o)*max((p_lp(i-1)-
pca1(i-1)),0)) + ul*cv*av*sqrt((2/rho_o)*max((p_lp(i-1)-pca2(i-1)),0))
- q_m(i-1));
  v_hp(i) = v_hp(i-1)+dt*(-ul*cv*av*sqrt((2/rho_o)*max((pca1(i-1)-
p_hp(i-1)),0)) - ul*cv*av*sqrt((2/rho_o)*max((pca2(i-1)-p_hp(i-1)),0))
+ q_m(i-1));
  vpc1(i) = vpc1(i-1)+dt*((ul-1)*cc*ac*sqrt((2/rho_o)*abs(pca1(i-1)-
ppc1(i-1)))*sign(pca1(i-1)-ppc1(i-1)));
  vpc2(i) = vpc2(i-1)+dt*((ul-1)*cc*ac*sqrt((2/rho_o)*abs(pca2(i-1)-
ppc2(i-1)))*sign(pca2(i-1)-ppc2(i-1)));

  pca1(i) = pca1(1)*(vca1(1)/vca1(i))^gamma;
  pca2(i) = pca2(1)*(vca2(1)/vca2(i))^gamma;
  p_lp(i) = p_lp(1)*(v_lp(1)/v_lp(i))^gamma;
  p_hp(i) = p_hp(1)*(v_hp(1)/v_hp(i))^gamma;
  ppc1(i) = ppc1(1)*(vpc1(1)/vpc1(i))^gamma;
```

```
  ppc2(i) = ppc2(1)*(vpc2(1)/vpc2(i))^gamma;

  f_pto(i) = -sp*(pca1(i)-pca2(i));
  fpto = f_pto(i);
  torqm(i) = mdf*max_dhm*(p_hp(i)-p_lp(i))/(2*pi);
  if torqm(i) > torqm_max, torqm(i) = torqm_max; end

  % angular velocity in radians per second
  if gen_speed == 0 % for fixed rotational speed of the generator
    omega_m(i) = 2*pi*speed_max/60; % the generator torque matches the
motor torque
  else % for variable rotational speed of the generator
    omega_m(i) = omega_m(i-1)+dt*(torqm(i)-torqg(i))/Jr; % the
generator speed matches the motor speed
    if omega_m(i) > omega_max, omega_m(i) = omega_max; end
  end

  q_m(i) = mdf*max_dhm*omega_m(i)/(2*pi); % fluid flow rate from the
high pressure accumulator into the hydraulic motor

  if (v_hp(1)-v_hp(i))/dt < q_m(i)
    q_m(i) = (v_hp(1)-v_hp(i))/dt;
    omega_m(i) = 2*pi*q_m(i)/(mdf*max_dhm);
    if omega_m(i) > omega_max, omega_m(i) = omega_max; end
  end

  if gen_speed == 0 % fixed rotational speed of the generator
    gpw(i) = torqm(i)*omega_m(i);
  else % variable rotational speed of the generator
    gpw(i) = torqg(i)*omega_m(i);
  end

  if control_m == 1
    if sign(Y(2,i)) ~= sign(Y(2,i-1)) && i > openv
      [f_indx] = find(tm_c(f_peak)>tm_c(1,inx));
      if isempty(f_indx) == 0
        if (tm_c(1,f_peak(f_indx(1)))-tm_c(1,inx)) >
(2*pi/(control_coef_1*omega_d))
          t_latch = tm_c(1,f_peak(f_indx(1))) -
2*pi/(control_coef_1*omega_d);
          openv = fix(t_latch/dt); % open valve at this time step
          if i < openv
            ul = 1;
          end
        end
      end
    else
      if i == openv
        ul = 0;
      end
    end
  end
end
Y = Y';
```

APPENDIX – C

CONVOLUTION INTEGRAL FOR THE RADIATION KERNEL

```
function [xpr_h] = Buoy_heave(t,x)
% code developed by Miltos Kotinis and Praveen Malali - last updated on
7/25/2015
  global inx; global k_rad_0; global w_exc; global sol_tmp; global
tm_c; global conv; global fpto;
  global m_b; global m_inf; global k_hs; global pcf_kr; global k_rad_t;
global conv_inx;
  % compute the convolution integral
  if inx>1
    k_rad = ppval(pcf_kr,t);
    conv = 0.5*tm_c(1,2)*k_rad*sol_tmp(1,2);
  end
  if inx>2
    if max(inx-conv_inx-1,0)==0
      imin = 3;
    else
      imin = inx-conv_inx+2;
    end
    for i=imin:inx
      k_rad = k_rad_t(1,inx-i+2);
      conv = conv + 0.5*(tm_c(1,i) - tm_c(1,i-2))*k_rad*sol_tmp(i-1,2);
    end
  end
  % compute the response
  if inx > 1
    xpr_h = [x(2,1); (-k_hs*x(1,1)-(0.5*(tm_c(1,inx) - tm_c(1,inx-
1))*k_rad_0)*x(2,1)+w_exc(inx,1)-conv+fpto)/(m_b+m_inf)];
  else
    xpr_h = x;
  end
end
```

APPENDIX – D

RADIATION DAMPING COEFFICIENT AS A FUNCTION OF NON-DIMENSIONALIZED WAVE FREQUENCY

Non-dimensional wave frequency	Radiation damping coefficient
0.0000	0.0000
0.2236	0.1036
0.3162	0.1816
0.4472	0.2793
0.5477	0.3254
0.6325	0.3410
0.7071	0.3391
0.7746	0.3271
0.8367	0.3098
0.8944	0.2899
0.9487	0.2691
1.0000	0.2484
1.0955	0.2096
1.1832	0.1756
1.2649	0.1469
1.3416	0.1229
1.4142	0.1031
1.5811	0.0674
1.7321	0.0452
2.0000	0.0219
2.2361	0.0116
2.4495	0.0066
2.6458	0.0040
2.8284	0.0026
3.0000	0.0017
3.1623	0.0012
5.0000	0.0000

Table D1. Values of radiation damping coefficient for various non-dimensional frequencies [46].

APPENDIX – E

ADDED MASS COEFFICIENT AS A FUNCTION OF NON-DIMENSIONALIZED WAVE FREQUENCY

Non-dimensional wave frequency	Added mass coefficient
0.0000	0.8310
0.2236	0.8764
0.3162	0.8627
0.4472	0.7938
0.5477	0.7157
0.6325	0.6452
0.7071	0.5861
0.7746	0.5381
0.8367	0.4999
0.8944	0.4698
0.9487	0.4464
1.0000	0.4284
1.0955	0.4047
1.1832	0.3924
1.2649	0.3871
1.3416	0.3864
1.4142	0.3884
1.5811	0.3988
1.7321	0.4111
2.0000	0.4322
2.2361	0.4471
2.4495	0.4574
2.6458	0.4647
2.8284	0.4700
3.0000	0.4740
3.1623	0.4771
5.0000	0.5000

Table E1. Values of added mass coefficients for various non-dimensional frequencies [46].

APPENDIX – F

PARAMETER VALUES FOR DIFFERENT SEA STATES

Sea state	Significant wave height (m)	Most probable modal wave period (s)	Percentage probability of sea state (%)
1	0.05	-	0.70
2	0.30	7.5	6.80
3	0.88	7.5	23.70
4	1.88	8.8	27.80
5	3.25	9.7	20.64
6	5.00	12.4	13.15
7	7.50	15	6.05

Table F1. Values of characteristic parameters of various sea states in the North Atlantic [58].

APPENDIX – G

AVAILABLE POWER IN IRREGULAR SEAS

The expression for the modified P-M spectrum of the angular frequency, ω, is as follows [55],

$$S(\omega) = \left(\frac{(0.3125) * {\omega_m}^4 * \left(H_{1/3}\right)^2}{\omega^5}\right) * \exp\left(-1.25 * \left(\frac{\omega_m}{\omega}\right)^4\right) \quad \text{(G1)}$$

where $S(\omega)$ is the spectral density for the given sea state, ω is a frequency value from a given frequency range, ω_m is the modal or peak frequency for a given sea state and $H_{1/3}$ is the significant wave height which is the mean of one-third highest waves.

The transformation of the frequency spectrum to a period spectrum is as follows [75].

$$S(T) = \frac{2\pi}{T^2} S(\omega) \quad \text{(G2)}$$

where T is the wave period.

Therefore, the expression for the modified PM spectrum of the wave period, T is as follows.

$$S(T) = \frac{0.3125 * \left(H_{1/3}\right)^2}{T_m^4} * T^3 * e^{-\left(\frac{1.25}{T_m^4} T^4\right)} \quad \text{(G3)}$$

where $H_{1/3}$ is the significant wave height or mean of one-third highest waves for the chosen sea state, T_m is the modal wave period for the chosen sea state and T is the wave period from a given wave period range.

The wave power per meter of the incident wave crest for a deep-water irregular wave, i, is as follows [35],

$$P_{i/m} = \frac{\rho g^2 T_i}{4\pi} * \frac{H_i^2}{8} \quad \text{(G4)}$$

where ρ is the density of sea water, g is the acceleration due to gravity, T_i is the wave period of the i^{th} wave, H_i is the wave height of the i^{th} wave. The wave height is twice the absolute value of the wave amplitude (A_i) of the i^{th} wave.

The available power for a point absorber of known diameter, D, interacting with only the irregular deep water wave, i, is as follows.

$$P_i = \frac{D\rho g^2 T_i}{4\pi} * \frac{H_i^2}{8} \tag{G5}$$

The total energy, E, for deep-water wave component, i, is as follows [2],

$$E = \frac{H_i^2}{8} = S(T_i)dt \tag{G6}$$

Equation (G5) can be written as follows,

$$P_i = \frac{D\rho g^2 T_i}{4\pi} * S(T_i)dt \tag{G7}$$

or

$$P_i = \frac{D\rho g^2 T_i}{4\pi} * \frac{0.3125 * \left(H_{\frac{1}{3}}\right)^2}{T_{\mathrm{m}}^4} * T_i^3 * e^{-\left(\frac{1.25}{T_{\mathrm{m}}^4} T_i^4\right)} dt \tag{G8}$$

Therefore, the available power in a sea state for fully developed irregular seas can be computed as:

$$P_{av} = \frac{\rho g^2 r}{2\pi} * \frac{0.3125 * \left(H_{\frac{1}{3}}\right)^2}{T_{\mathrm{m}}^4} * \int_0^\infty T^4 * e^{-\left(\frac{1.25}{T_{\mathrm{m}}^4} T^4\right)} dt \tag{G9}$$

where ρ is the density of sea water, g is the acceleration due to gravity, r is the radius of the point absorber, $H_{1/3}$ is the significant wave height or mean of one-third highest waves for the chosen sea state, T_m is the modal wave period for the chosen sea state and T is the wave period from a given wave period range.

APPENDIX – H

CODE FOR RL/PI CONTROLLER FOR HEATING COIL

```
% initialize
clear;
clc;

nep = 1000; % number of episodes

spt = [45 40 45 40 45]; % setpoint values

nstp = 100; % number of steps per setpoint change interval

nsp = size(spt,2)*nstp; % total number of steps per episode

nfi = 6; % number of intervals for each discretized variable

% heating coil data
kp = 0.185; % proportional gains coefficient
ki = 0.0178; % integral gains coefficient

% inlet air temperature
Tai_min = 4; Tai_max = 10;
dTai = (Tai_max - Tai_min)/nfi; sTai = Tai_min:dTai:Tai_max;
%Tai = Tai_min + rand(nsp,1)*(Tai_max - Tai_min);

% inlet water temperature
Twi_min = 73; Twi_max = 81;
dTwi = (Twi_max - Twi_min)/nfi; sTwi = Twi_min:dTwi:Twi_max;
%Twi = Twi_min + rand(nsp,1)*(Twi_max - Twi_min);

% air flow rate
fa_min = 0.7; fa_max = 0.9;
dfa = (fa_max - fa_min)/nfi; sfa = fa_min:dfa:fa_max;
%fa = fa_min + rand(nsp,1)*(fa_max - fa_min);

% outlet air temperature
Tao_min = 36; Tao_max = 52; Tao = zeros(nsp,1);
dTao = (Tao_max - Tao_min)/nfi; sTao = Tao_min:dTao:Tao_max;

% outlet water temperature
Two_min = 40; Two_max = 60; Two = zeros(nsp,1);
dTwo = (Two_max - Two_min)/nfi; sTwo = Two_min:dTwo:Two_max;

% water flow rate
fw_min = 0.10317; fw_max = 0.34546; fw = zeros(nsp,1);
dfw = (fw_max-fw_min)/nfi; sfw = fw_min:dfw:fw_max;

% PI controller signal
c_min = 670; c_max = 1400; c = zeros(nsp,1); cp = zeros(nsp,1);
dc = (c_max - c_min)/nfi; sc  = c_min:dc:c_max;
```

```
% reinforcement learning
A =  [-100 -50 -20 -10 0 10 20 50 100]; % actions
Q = zeros(nfi,nfi,nfi,nfi,nfi,nfi,nfi,size(A,2)); % Q values storage
matrix
beta_int = 0.1; alpha = 0.1; gamma = 0.95; lambda = 0.995; prb(1) = 1;
%Q learning parameters
st_vst = zeros(nfi,nfi,nfi); % counter of number of visits per state
rmse = zeros(nep,1);
rwd = zeros(nsp,1); % reward
actn = zeros(nsp,1); % index of actions
sum_int = 0;
Tai(1:nsp,1) = Tai_min + rand(1)*(Tai_max - Tai_min); % initialize
external variables for 1st setpoint
Twi(1:nsp,1) = Twi_min + rand(1)*(Twi_max - Twi_min);
fa(1:nsp,1) = fa_min + rand(1)*(fa_max - fa_min);

for j = 1:nep,j
     Tsp = spt(1); % initial setpoint temperature

   pr_ind = 1; % initialize random action probability index
   prb(1) = lambda*prb(1);

   for i = 2:nsp,
       prb(i) = lambda*prb(i-1);
   end

   Tao(1) = 45.1; %Tao_min;
   Two(1) = 48;
   fw(1) = fw_max;
   act_temp =  randperm(size(A,2));
   actn(1) = act_temp(1); % take random initial action
   err(1) = Tsp-Tao(1);
   %sum_int = 0;
   sum_int = sum_int + err(1);
   %c = zeros(nsp,1); cp = zeros(nsp,1);
   cp(1) = kp*err(1)+ki*sum_int;
   normcp = 1;
   c(1) = c_max - (c_max-c_min)*normcp + A(actn(1));
   rwd(1) = -(err(1)^2 + beta_int*actn(1)^2);

   if c(1)> c_max,
      c(1) = c_max;
   end

   if c(1) < c_min,
      c(1) = c_min;
   end

   % determine current state
   idTai = max(ceil((Tai(1)-Tai_min)/dTai),1);
   idTwi = max(ceil((Twi(1)-Twi_min)/dTwi),1);
   idTao = max(ceil((Tao(1)-Tao_min)/dTao),1);
   idTwo = max(ceil((Two(1)-Two_min)/dTwo),1);
   idfa = max(ceil((fa(1)-fa_min)/dfa),1);
```

```
   idfw = max(ceil((fw(1)-fw_min)/dfw),1);
   idc = max(ceil((c(1)-c_min)/dc),1);
   st_vst(idTai,idTwi,idfa) = st_vst(idTai,idTwi,idfa) + 1;
   rms(1) = err(1)^2; % initialize RMS error
   spc = 1; % counter for setpoint adjustment

   for t = 2:nsp; % loop
      spc = spc + 1;
      if rem(spc-1,nstp)==0,
          Tsp = spt((spc-1)/nstp+1);
      end % adjust setpoint temperature

      % store current state data
      idTai_c = idTai; idTwi_c = idTwi; idTao_c = idTao;
      idTwo_c = idTwo; idfa_c = idfa; idfw_c = idfw; idc_c = idc;

      % determine next state
      fw(t) = 0.008+0.00703*(-41.29+0.30932*c(t-1)-3.2681*10^-4*c(t-
1)^2+9.56*10^-8*c(t-1)^3);
      Two(t)= Two(t-1)+0.64908*fw(t-1)*(Twi(t-1)-Two(t-
1))+(0.02319+0.10357*fw(t-1)+0.02806*fa(t-1))*(Tai(t-1)-(Twi(t-
1)+Two(t-1))/2);
      Tao(t)= Tao(t-1)+0.19739*fa(t-1)*(Tai(t-1)-Tao(t-
1))+(0.03184+0.15440*fw(t-1)+0.04468*fa(t-1))*(-Tai(t-1)+(Twi(t-
1)+Two(t-1))/2)+0.20569*(Tai(t)-Tai(t-1));

      idTai = max(ceil((Tai(t)-Tai_min)/dTai),1);
      idTwi = max(ceil((Twi(t)-Twi_min)/dTwi),1);
      idTao = max(ceil((Tao(t)-Tao_min)/dTao),1);
      idTwo = max(ceil((Two(t)-Two_min)/dTwo),1);
      idfa  = max(ceil((fa(t)-fa_min)/dfa),1);
      idfw  = max(ceil((fw(t)-fw_min)/dfw),1);
      err(t) = Tsp-Tao(t);
      sum_int = sum_int + 0.5*(err(t)+err(t-1));
      rms = rms + err(t)^2;
      cp(t) = kp*err(t)+ki*sum_int;
      normcp = (cp(t)- min(cp))/(max(cp)- min(cp));
      c(t) = c_max - (c_max-c_min)*normcp;
      idc = max(ceil((c(t)-c_min)/dc),1);

      if t > 2, % compute reward
         rwd(t-1) = -(err(t-1)^2 + beta_int*(actn(t-1)-actn(t-2))^2);
      end

      % Update Q value of current state
      for i = 1:size(A,2)
          Q_temp = max(Q(idTai,idTwi,idTao,idTwo,idfa,idfw,idc,:));
      end
         Q(idTai_c,idTwi_c,idTao_c,idTwo_c,idfa_c,idfw_c,idc_c,actn(t-
1)) = alpha*rwd(t-1) + alpha*gamma*Q_temp +(1-
alpha)*Q(idTai_c,idTwi_c,idTao_c,idTwo_c,idfa_c,idfw_c,idc_c,actn(t-
1));

      if rand(1) <= prb(pr_ind)
         act_temp =  randperm(size(A,2));
```

```
         actn(t) = act_temp(1);
      else
         [dummy,actn(t)] =
max(Q(idTai,idTwi,idTao,idTwo,idfa,idfw,idc,:));
      end

      c(t) = c(t) + A(actn(t));

      if c(t) > c_max, c(t) = c_max; end
      if c(t) < c_min, c(t) = c_min; end
      pr_ind = pr_ind + 1;
   end
   rmse(j) = sqrt(rms/j);
   refresh

end
figure (1); plot(Tao,'color','r')

figure (2); plot(rmse);
```

APPENDIX – I

FORTRAN CODE FOR RBF NETWORK ENSEMBLE

```
Program ELMRBF

Implicit none

Integer (KIND = 4) :: i, j, ij, ji, jj, clk1, clk2, clk3, npmax,
nvtmax, enscount, xi, xiter
Integer (KIND = 4) :: swsz, innit, nfeat, nhl, ntr, nvd, nts, idum,
gbest, gbdummy(1), frnsl, indf
Real (KIND = 8) :: rnd1, rnd2, startn, sigmamin, sigmamax, omegamin,
omegamax, xmin, xmax, phi1, phi2, phi, chi
Real (KIND = 8) :: rmsegb, pvgbs, pvgbom, wmin, wmax, eps, pfeat, pmut,
mae, rmsef, maef, tcrit, tmpytens
Real (KIND = 4) :: ran4
Real (KIND = 8), allocatable :: pv(:,:), vpv(:,:), xv(:,:,:),
vxv(:,:,:), trn(:,:), vld(:,:), tst(:,:), yt(:,:), ytens(:)
Real (KIND = 8), allocatable :: minv(:), maxv(:), rmse(:), rmsepb(:),
krn(:,:,:), pvpb(:,:), xvgb(:,:), xvpb(:,:,:), pbrslt(:,:)
Real (KIND = 8), allocatable :: v(:,:), outw(:), nrmtrn(:,:),
nrmvld(:,:), nrmtst(:,:), yout(:), rslt(:,:), rsltgb(:), stdev(:)
Integer (KIND = 4), allocatable :: feat(:,:), fgb(:)

Open(1,File='TrainD.txt')
Open(2,File='ValD.txt')
Open(3,File='TestD.txt')
Open(4,File='ResultsD.txt')

Call system_clock(count=clk1)

! Set parameter values
swsz = 20 !number of particles in swarm
innit = 50 !number of iterations
startn = 1.d+8
eps = 1.d0
pfeat = 0.d0
pmut = 0.2d0
xiter = 50
nhl = 20 !number of hidden nodes
nfeat = 5 !number of features
ntr = 227 !number of points in training set
nvd = 56 !number of points in validation set
nts = 284 !number of points in testing set
npmax = max(ntr,nvd,nts)
nvtmax = max(nvd,nts)

!Kernel properties
sigmamin = 1.d0 !sigma
sigmamax = 100.d0
xmin = -1.d0 !coordinates of centers
xmax = 1.d0

phi1 = 2.05d0
phi2 = 2.05d0
```

```
phi = phi1 + phi2
chi = 2.d0/(phi-2.d0+sqrt(phi**2-4.d0*phi))

Allocate(pv(swsz,2),vpv(swsz,2),xv(swsz,nhl,nfeat),vxv(swsz,nhl,nfeat),
pvpb(swsz,2),xvpb(swsz,nhl,nfeat),xvgb(nhl,nfeat))
Allocate(krn(swsz,npmax,nhl+1),feat(swsz,nfeat),fgb(nfeat),pbrslt(swsz,
nhl+1),yt(swsz,nvtmax),ytens(nvtmax),stdev(nvtmax))
Allocate(trn(ntr,nfeat+1),vld(nvd,nfeat+1),tst(nts,nfeat+1),nrmtrn(ntr,
nfeat+1),nrmvld(nvd,nfeat+1),nrmtst(nts,nfeat+1))
Allocate(minv(nfeat+1),maxv(nfeat+1),rmse(swsz),rmsepb(swsz),yout(nvtma
x),outw(nhl+1),v(nhl+1,nhl+1),rslt(swsz,nhl+1),rsltgb(nhl+1))

!Read training data set
Do i = 1,ntr
    Read(1,*) (trn(i,j), j = 1,nfeat+1)
End do

!Read validation data set
Do i = 1,nvd
    Read(2,*) (vld(i,j), j = 1,nfeat+1)
End do

!Read testing data set
Do i = 1,nts
    Read(3,*) (tst(i,j), j = 1,nfeat+1)
End do

!Normalize input and output data between -1 and 1
Do j = 1,nfeat+1
    minv(j) = min(minval(trn(:,j)),minval(vld(:,j)),minval(tst(:,j)))
    maxv(j) = max(maxval(trn(:,j)),maxval(vld(:,j)),maxval(tst(:,j)))
End do

Do i = 1,ntr
    Do j = 1,nfeat+1
        nrmtrn(i,j) = (2.d0*trn(i,j) - maxv(j) - minv(j))/(maxv(j) -
minv(j))
    End do
End do

Do i = 1,nvd
    Do j = 1,nfeat+1
        nrmvld(i,j) = (2.d0*vld(i,j) - maxv(j) - minv(j))/(maxv(j) -
minv(j))
    End do
End do

Do i = 1,nts
    Do j = 1,nfeat+1
        nrmtst(i,j) = (2.d0*tst(i,j) - maxv(j) - minv(j))/(maxv(j) -
minv(j))
    End do
End do

Call Random_Seed
Call Random_Number(rnd1)
```

```
idum = -max(nint(rnd1*startn),1)
Do xi = 1,xiter
print*, xi
!Initialize kernel centers and PUF parameters for each particle
Do i = 1,swsz
    indf = 0
    Do ji = 1,nfeat   !Design swarm architecture
        rnd1 = ran4(idum)
        If (rnd1 <= pfeat) then !Prune input layer
            feat(i,ji) = 0
        Else
            feat(i,ji) = 1
            indf = indf + 1
        End if
    End do
    If (indf == 0) then !If no feature has been selected then,
        rnd1 = ran4(idum)
        frnsl = ceiling(rnd1*real(nfeat)) !select one randomly
        feat(i,frnsl) = 1
    End If
    rnd1 = ran4(idum)
    pv(i,1) = sigmamin + rnd1*(sigmamax-sigmamin) !Initialize sigma
    Do j = 1,nhl
        Do ij = 1,nfeat
            rnd1 = ran4(idum)
            xv(i,j,ij) = xmin + rnd1*(xmax-xmin) !Initialize center
coordinates
        End do
    End do
End do
vpv = 0.d0 !Initialize particle velocities for parameters (set equal to
zero).
vxv = 0.d0 !Initialize particle velocities for center coordinates (set
equal to zero).
rmsepb = 0.d0; rmsegb = 0.d0
Do jj = 1,innit
    rmse = 0.d0;
    !Find H-O layer weights using SVD
    Do i = 1,swsz
        krn(i,:,:) = 0.d0
        Do j = 1,ntr
            Do ij = 1,nhl
                Do ji = 1,nfeat
                    If (feat(i,ji) == 1) krn(i,j,ij) = krn(i,j,ij) +
(xv(i,ij,ji)-nrmtrn(j,ji))**2
                End do
                krn(i,j,ij)=1.d0/sqrt(krn(i,j,ij)+pv(i,1)**2)
            End do
            krn(i,j,nhl+1) = 1.d0
        End do
        outw = 0.d0; v = 0.d0; rslt(i,:) = 0.d0
        Call svdcmp(krn(i,1:ntr,:),ntr,nhl+1,outw,v)
        wmax = maxval(outw)
        wmin = wmax*real(max(nhl+1,ntr))*epsilon(eps)
        where (outw < wmin) outw = 0.d0
```

```
        Call
svdksb(krn(i,1:ntr,:),outw,v,ntr,nhl+1,nrmtrn(:,nfeat+1),rslt(i,:))
        !Evaluate particles on the validation set
        krn(i,:,:) = 0.d0
        yout = 0.d0
        Do j = 1,nvd
            Do ij = 1,nhl
                Do ji = 1,nfeat
                    If (feat(i,ji) == 1) krn(i,j,ij) = krn(i,j,ij) +
(xv(i,ij,ji)-nrmvld(j,ji))**2
                End do
                krn(i,j,ij)=1.d0/sqrt(krn(i,j,ij)+pv(i,1)**2)
                yout(j) = yout(j) + rslt(i,ij)*krn(i,j,ij)
            End do
            yout(j) = yout(j) + rslt(i,nhl+1)
            rmse(i) = rmse(i) + (yout(j)-nrmvld(j,nfeat+1))**2
        End Do
        rmse(i) = sqrt(rmse(i)/real(nvd))
    End do
    gbdummy(1) = minloc(rmse,1) !Find global best solution
    gbest = gbdummy(1)
    If (rmse(gbest) < rmsegb .or. jj == 1) then
        xvgb = xv(gbest,:,:)
        pvgbs = pv(gbest,1)
        pvgbom = pv(gbest,2)
        rmsegb = rmse(gbest)
        rsltgb = rslt(gbest,:)
        fgb = feat(gbest,:)
    End If
    Do i = 1,swsz !Find personal best solution for each particle
        If (rmse(i) < rmsepb(i) .or. jj == 1) then
            xvpb(i,:,:) = xv(i,:,:)
            pvpb(i,1) = pv(i,1)
            pvpb(i,2) = pv(i,2)
            rmsepb(i) = rmse(i)
            pbrslt(i,:) = rslt(i,:)
        End If
    End do
    If (jj == innit) exit
    !Optimize kernel centers and parameters for each particle
    idum = idum - 1
    Do i = 1,swsz
        rnd1 = ran4(idum)
        If (rnd1 > pmut) then
            rnd1 = ran4(idum)
            rnd2 = ran4(idum)
            vpv(i,1) = chi*(vpv(i,1)+phi1*rnd1*(pvpb(i,1)-
pv(i,1))+phi2*rnd2*(pvgbs-pv(i,1)))
            pv(i,1) = pv(i,1) + vpv(i,1)
            If (pv(i,1) > sigmamax) then
                pv(i,1) = sigmamax; vpv(i,1) = 0.d0
            End If
            If (pv(i,1) < sigmamin) then
                pv(i,1) = sigmamin; vpv(i,1) = 0.d0
            End If
            Do j = 1,nhl
```

```
                rndl = ran4(idum)
                rnd2 = ran4(idum)
                Do ji = 1,nfeat
                    vxv(i,j,ji) =
chi*(vxv(i,j,ji)+phi1*rnd1*(xvpb(i,j,ji)-
xv(i,j,ji))+phi2*rnd2*(xvgb(j,ji)-xv(i,j,ji)))
                    xv(i,j,ji) = xv(i,j,ji) + vxv(i,j,ji)
                    If (xv(i,j,ji) > xmax) then
                        xv(i,j,ji) = xmax; vxv(i,j,ji) = 0.d0
                    End If
                    If (xv(i,j,ji) < xmin) then
                        xv(i,j,ji) = xmin; vxv(i,j,ji) = 0.d0
                    End If
                End do
            End do
        Else
            rndl = ran4(idum)
            pv(i,1) = sigmamin + rnd1*(sigmamax-sigmamin)
            Do j = 1,nhl
                Do ij = 1,nfeat
                    rndl = ran4(idum)
                    xv(i,j,ij) = xmin + rnd1*(xmax-xmin)
                End do
            End do
        End If
    End do
    print*, jj, rmsegb
End do

Call system_clock(count=clk2)
clk3 = clk2 - clk1
print*, clk3
! Compute output of ensemble on testing set
yt= 0.d0; ytens = 0.d0; krn = 0.d0
do j = 1,swsz
    do jj = 1,nts
        do ij = 1,nhl
            do ji = 1,nfeat
                if (feat(j,ji) == 1) krn(j,jj,ij) = krn(j,jj,ij) +
(xvpb(j,ij,ji)-nrmtst(jj,ji))**2
            end do
            krn(j,jj,ij)=1.d0/sqrt(krn(j,jj,ij)+pvpb(j,1)**2)
            yt(j,jj) = yt(j,jj) + pbrslt(j,ij)*krn(j,jj,ij)
        end do
        yt(j,jj) = yt(j,jj) + pbrslt(j,nhl+1)
    end do
end do
rmsef = 0.d0; maef = 0.d0; tcrit = 2.24
do jj = 1,nts
    ytens(jj) = sum(yt(1:swsz,jj))/real(swsz)
    stdev(jj) = 0.d0
    do j = 1,swsz
        stdev(jj) = stdev(jj) + (yt(j,jj)-ytens(jj))**2
    end do
    stdev(jj) = sqrt(stdev(jj)/real(swsz-1))
    tmpytens = 0.d0; enscount = 0
```

```
    ! Use Chauvenet's criterion for outlier detection
    do i = 1,swsz
        if(abs((yt(i,jj)-ytens(jj))/stdev(jj))<=tcrit) then
            tmpytens = tmpytens + yt(i,jj)
            enscount = enscount + 1
        end if
    end do
    ytens(jj) = tmpytens/real(enscount)
    ytens(jj) = (ytens(jj)*(maxv(nfeat+1) - minv(nfeat+1)) +
minv(nfeat+1) + maxv(nfeat+1))/2.d0
    rmsef = rmsef + (ytens(jj)-tst(jj,nfeat+1))**2
    maef = maef + abs(ytens(jj)-tst(jj,nfeat+1))
end do
rmsef = sqrt(rmsef/real(nts))
maef =  maef/real(nts)
print*, rmsef, maef
!Evaluate global best particle on the testing set
krn(1,:,:) = 0.d0
yout = 0.d0
rmse(1) = 0.d0
mae = 0.d0
Do j = 1,nts
    Do ij = 1,nhl
        Do ji = 1,nfeat
            If (fgb(ji) == 1) krn(1,j,ij) = krn(1,j,ij) + (xvgb(ij,ji)-
nrmtst(j,ji))**2
        End do
        krn(1,j,ij)=1.d0/sqrt(krn(1,j,ij)+pvgbs**2)
        yout(j) = yout(j) + rsltgb(ij)*krn(1,j,ij)
    End do
    yout(j) = yout(j) + rsltgb(nhl+1)
    yout(j) = (yout(j)*(maxv(nfeat+1) - minv(nfeat+1)) + minv(nfeat+1)
+ maxv(nfeat+1))/2.d0
    rmse(1) = rmse(1) + (yout(j)-tst(j,nfeat+1))**2
    mae = mae + abs(yout(j)-tst(j,nfeat+1))
End Do
rmse(1) = sqrt(rmse(1)/real(nts))
mae =  mae/real(nts)
print*, ' '
print*, rmse(1), mae
write(4,5) rmse(1), rmsef, mae, maef
5 format (4F9.5)
End do
Do j = 1,nts
    print*, yout(j),tst(j,nfeat+1)
End do
Close(4)
Close(3)
Close(2)
Close(1)

End Program ELMRBF
```

APPENDIX – J

RUNGE-KUTTA (R-K4) SOLVER FOR ODE COMBINED WITH ADAPTATION OF Q-LEARNING ALGORITHM

```
function Y = ode4_RL(odefun,tspan,y0,varargin)
%ODE4  The solver implements the classical Runge-Kutta method of order
% 4 combined with the adaptation of the Q-learning algorithm
%
global inx; global sol_tmp; global f_peak; global t_latch; global gpw;
global control_coef_1; global k_rad_0; global conv; global control_m;
global omega_d; global tm_c; global dt; global gen_speed; global fpto;
global w_exc; global k_hs; global q_m; global f_pto; global mdf;
global hydro_f; global torqm; global torqg; global omega_m;
global p_hp; global p_lp; global pca1; global pca2;
global v_lp; global v_hp; global vca1; global vca2;
global ppc1; global ppc2; global vpc1; global vpc2;

global Q_f; global A1; global A2; global prbt; global opt_pol;

h = diff(tspan);
y0 = y0(:);   % Make a column vector
neq = length(y0); N = length(tspan); Y = zeros(neq,N); F =
zeros(neq,4);
Y(:,1) = y0;
p_lp = zeros(N,1); p_hp = zeros(N,1); v_lp = zeros(N,1); v_hp =
zeros(N,1);
pca1 = zeros(N,1); pca2 = zeros(N,1); vca1 = zeros(N,1); vca2 =
zeros(N,1);
ppc1 = zeros(N,1); ppc2 = zeros(N,1); vpc1 = zeros(N,1); vpc2 =
zeros(N,1);
f_pto = zeros(N,1); hydro_f = zeros(N,1); gpw = zeros(N,1);
torqm = zeros(N,1); torqg = 30*ones(N,1); omega_m = zeros(N,1);
q_m = zeros(N,1);

% RL settings
m_disp_min = 0.8; % minimum motor displacement value
m_disp_max = 1.0; % maximum motor displacement value
m_disp_d = 6; % number of discrete action values - action #1
m_disp = linspace(m_disp_min,m_disp_max,m_disp_d)'; % discrete action
values - action #1
cf_fr = [6; 8; 10; 12; 14]; % discrete action values - action #2
wave_p_min = 0.; % minimum wave excitation peak value to define range
(MN)
wave_p_max = 1.2; % maximum wave excitation peak value to define range
(MN)
wave_p_d = 5; % number of discretized wave excitation peak states
wave_p = linspace(wave_p_min,wave_p_max,wave_p_d)';
d_wave = (wave_p_max-wave_p_min)/(wave_p_d-1); % discretization
interval
A1 = m_disp; % action #1: adjust motor displacement value
A2 = cf_fr; % action #2: adjust valve opening instant
```

```
Q_f = zeros(length(wave_p),length(A1),length(A2)); % Q values storage
matrix
prbt = ones(wave_p_d,1);
opt_pol = zeros(wave_p_d,2);
beta_d = 0.01; % RL discount factor parameter;
eta_d = 0.05; sigma_rl = 0.99;
gpw_ind = 0; rwd_ind = 0; rwd_ind_c = 0; state_ind = 0;
Y_flag1 = 0; Y_flag2 = 0;
act1 =  randperm(length(A1)); act2 =  randperm(length(A2));
actn_1 = act1(1); actn_2 = act2(1);
mdf = A1(actn_1,1);
control_coef_1 = A2(actn_2,1);
gamma_rl = 0;
Y_crit = 2.40; % motion amplitude constraint in m

gamma = 1.4; % isentropic process, value for nitrogen
rho_o = 850; % density of oil in kg/m^3
ul = 1;
% initial values
vca1(1) = 0.05; % in m^3
vca2(1) = 0.05; % in m^3
vpc1(1) = 0.5; % in m^3
vpc2(1) = 0.5; % in m^3
v_lp(1) = 1; % in m^3
v_hp(1) = 2; % in m^3
p_lp(1) = 10*10^6; % pressure in LP accumulator in N/m^2
p_hp(1) = 10*10^6; % pressure in HP accumulator in N/m^2
pca1(1) = 10*10^6; % pressure in compressibility accumulator #1 in
N/m^2
pca2(1) = 10*10^6; % pressure in compressibility accumulator #2 in
N/m^2
ppc1(1) = 10*10^6; % pressure in phase control accumulator #1 in N/m^2
ppc2(1) = 10*10^6; % pressure in phase control accumulator #2 in N/m^2

% constants
sp = 0.05; % piston surface area in m^2
% hydraulic motor data
speed_max = 3000; % maximum continuous speed in rev/min
max_dhm = 165*10^-6; % in m^3 per rev
torqm_max = 659; % continuous output torque in N*m
omega_m(1) = 2*pi*(speed_max/2)/60; % angular velocity in radians per
second
omega_max = 2*pi*speed_max/60; % maximum angular velocity in radians
per second
% Control parameters
cv = 0.95;
cc = 0.95;
av = 0.002; % m^2
ac = 0.002; % m^2
Jr = 7.5; % kg*s^2, combined rotational inertia of motor, generator,
and shaft
openv = 1;
for i = 2:N
  ti = tspan(i-1);
  hi = h(i-1);
  yi = Y(:,i-1);
```

```
  F(:,1) = feval(odefun,ti,yi); inx = inx+1;
  F(:,2) = feval(odefun,ti+0.5*hi,yi+0.5*hi*F(:,1),varargin{:});
  sol_tmp(inx,:) = F(:,2)';
  F(:,3) = feval(odefun,ti+0.5*hi,yi+0.5*hi*F(:,2),varargin{:});
  sol_tmp(inx,:) = F(:,3)'; inx = inx+1;
  F(:,4) = feval(odefun,tspan(i),yi+hi*F(:,3),varargin{:});
  Y(:,i) = yi + (hi/6)*(F(:,1) + 2*F(:,2) + 2*F(:,3) + F(:,4));
  sol_tmp(inx,:) = Y(:,i)';
  hydro_f(i) = -k_hs*Y(1,i)-(0.5*(tm_c(1,inx)-tm_c(1,inx-
1))*k_rad_0+conv)*Y(2,i)+w_exc(inx,1); % hydrodynamic force

  vca1(i) = vca1(i-1)+dt*(-
sp*Y(2,i)+ul*cv*av*sqrt((2/rho_o)*max((pca1(i-1)-p_hp(i-1)),0)) -
ul*cv*av*sqrt((2/rho_o)*max((p_lp(i-1)-pca1(i-1)),0)) - (ul-
1)*cc*ac*sqrt((2/rho_o)*abs(pca1(i-1)-ppc1(i-1)))*sign(pca1(i-1)-
ppc1(i-1)));
  vca2(i) = vca2(i-
1)+dt*(sp*Y(2,i)+ul*cv*av*sqrt((2/rho_o)*max((pca2(i-1)-p_hp(i-1)),0))
- ul*cv*av*sqrt((2/rho_o)*max((p_lp(i-1)-pca2(i-1)),0)) - (ul-
1)*cc*ac*sqrt((2/rho_o)*abs(pca2(i-1)-ppc2(i-1)))*sign(pca2(i-1)-
ppc2(i-1)));
  v_lp(i) = v_lp(i-1)+dt*(ul*cv*av*sqrt((2/rho_o)*max((p_lp(i-1)-
pca1(i-1)),0)) + ul*cv*av*sqrt((2/rho_o)*max((p_lp(i-1)-pca2(i-1)),0))
- q_m(i-1));
  v_hp(i) = v_hp(i-1)+dt*(-ul*cv*av*sqrt((2/rho_o)*max((pca1(i-1)-
p_hp(i-1)),0)) - ul*cv*av*sqrt((2/rho_o)*max((pca2(i-1)-p_hp(i-1)),0))
+ q_m(i-1));
  vpc1(i) = vpc1(i-1)+dt*((ul-1)*cc*ac*sqrt((2/rho_o)*abs(pca1(i-1)-
ppc1(i-1)))*sign(pca1(i-1)-ppc1(i-1)));
  vpc2(i) = vpc2(i-1)+dt*((ul-1)*cc*ac*sqrt((2/rho_o)*abs(pca2(i-1)-
ppc2(i-1)))*sign(pca2(i-1)-ppc2(i-1)));

  pca1(i) = pca1(1)*(vca1(1)/vca1(i))^gamma;
  pca2(i) = pca2(1)*(vca2(1)/vca2(i))^gamma;
  p_lp(i) = p_lp(1)*(v_lp(1)/v_lp(i))^gamma;
  p_hp(i) = p_hp(1)*(v_hp(1)/v_hp(i))^gamma;
  ppc1(i) = ppc1(1)*(vpc1(1)/vpc1(i))^gamma;
  ppc2(i) = ppc2(1)*(vpc2(1)/vpc2(i))^gamma;

  f_pto(i) = -sp*(pca1(i)-pca2(i));
  fpto = f_pto(i);
  torqm(i) = mdf*max_dhm*(p_hp(i)-p_lp(i))/(2*pi);
  if torqm(i) > torqm_max, torqm(i) = torqm_max; end

  % angular velocity in radians per second
  if gen_speed == 0 % for fixed rotational speed of the generator
    omega_m(i) = 2*pi*speed_max/60; % the generator torque matches the
motor torque
  else % for variable rotational speed of the generator
    omega_m(i) = omega_m(i-1)+dt*(torqm(i)-torqg(i))/Jr; % the
generator speed matches the motor speed
    if omega_m(i) > omega_max, omega_m(i) = omega_max; end
  end
```

```
  q_m(i) = mdf*max_dhm*omega_m(i)/(2*pi); % fluid flow rate from the
high pressure accumulator into the hydraulic motor

  if (v_hp(1)-v_hp(i))/dt < q_m(i)
    q_m(i) = (v_hp(1)-v_hp(i))/dt;
    omega_m(i) = 2*pi*q_m(i)/(mdf*max_dhm);
    if omega_m(i) > omega_max, omega_m(i) = omega_max; end
  end

  if gen_speed == 0 % fixed rotational speed of the generator
    gpw(i) = torqm(i)*omega_m(i);
  else % variable rotational speed of the generator
    gpw(i) = torqg(i)*omega_m(i);
  end

  if gpw_ind == 1
    if (abs(Y(1,i)) > Y_crit || i < floor(N/4))  % if true, do not
calculate reward
      Y_flag1 = 1;
    else
      Y_flag1 = 0;
    end
    rwd(rwd_ind) = exp(-beta_d*(rwd_ind-1)*dt)*gpw(i);
    rwd_ind = rwd_ind + 1;
  end

  if i < floor(N/4)
    Y_flag2 = 1;
  else
    Y_flag2 = 0;
  end

  if control_m == 1
    if sign(Y(2,i)) ~= sign(Y(2,i-1)) && i > openv
      gpw_ind = 0; rwd_ind_c = rwd_ind;
      if state_ind > 0
        if Y_flag1 == 1
          rwd_d = 0;
        else
          rwd_d = dt*trapz(rwd(1:rwd_ind_c-1)); % calculate reward
        end
        t2_rl = tm_c(1,inx);
        gamma_rl = exp(-beta_d*(t2_rl-t1_rl)); % calculate discount
factor
      end
      [f_indx] = find(tm_c(f_peak)>tm_c(1,inx));
      if isempty(f_indx) == 0
        if state_ind > 0
          id_wave_p_c = id_wave_p;
        end
        wave_p = w_exc(f_peak(f_indx(1)));
        id_wave_p = min(ceil((abs(wave_p/10^6)-
wave_p_min)/d_wave),wave_p_d); % identify the next state based on the
next wave excitation peak
        state_ind = state_ind + 1;
```

```
        if state_ind > 1
          Q_f(id_wave_p_c,actn_1,actn_2) =
Q_f(id_wave_p_c,actn_1,actn_2) + eta_d*(rwd_d +
gamma_rl*max(max(Q_f(id_wave_p,:,:))) -
Q_f(id_wave_p_c,actn_1,actn_2)); % update Q function value
        end
        if Y_flag2 == 0
          prbt(id_wave_p,1) = sigma_rl*prbt(id_wave_p,1);
          if rand <= prbt(id_wave_p) % take random actions
            act1 =  randperm(length(A1)); act2 =  randperm(length(A2));
            actn_1 = act1(1); actn_2 = act2(1);
            mdf = A1(actn_1,1);
            control_coef_1 = A2(actn_2,1);
          else
            dmy1 = max(max(Q_f(id_wave_p,:,:)));
            dmy2 = find(Q_f==dmy1,1);
            [~, dmy3, dmy4] = ind2sub(size(Q_f),dmy2);
            mdf = A1(dmy3,1);
            control_coef_1 = A2(dmy4,1);
            actn_1 = dmy3;
            actn_2 = dmy4;
          end
        end
        if (tm_c(1,f_peak(f_indx(1)))-tm_c(1,inx)) >
(2*pi/(control_coef_1*omega_d))
          t_latch = tm_c(1,f_peak(f_indx(1))) -
2*pi/(control_coef_1*omega_d);
          if state_ind > 0
            t1_rl = t_latch;
          end
          openv = fix(t_latch/dt); % open valve at this time step
          if i < openv
            ul = 1;
          end
        end
      end
    else
      if i == openv
        ul = 0;
        gpw_ind = 1; rwd_ind = 1; % open valve and start measuring
reward;
      end
    end
  end
end
dmy1 = max(max(Q_f(id_wave_p,:,:)));
dmy2 = find(Q_f==dmy1,1);
[~, dmy3, dmy4] = ind2sub(size(Q_f),dmy2);
vol_f = A1(dmy3,1)
con_coef = A2(dmy4,1)
```

VITA

PRAVEEN D. MALALI
7426 North Shore Road, Norfolk, Virginia 23505|(908) 902-7993|pmala002@odu.edu

EDUCATION

- **M.S.** in **Mechanical Engineering**, Old Dominion University, Norfolk, Virginia, USA, December 2010.
  - Thesis title: "**Prediction of shock diamonds and Mach disk in an under-expanded air jet**".
- **B.E.** in **Industrial Engineering and Management**, Visvesvaraya Technological University, Bangalore, Karnataka, India, June 2006.

SELECTED PUBLICATIONS

- Malali, P., Kotinis, M., (2015) **"PSO-based Training, Pruning, and Ensembling of Extreme Learning Machine Networks"**, International Journal of Computational Engineering Research (IJCER), pp 2254-2266, Vol. 5, No. 6, June 2015.

- Malali, P., Bais, P., Choate, E., Chaturvedi, S., Yoon, J., (2012) "**Uncertainty Analysis and Instrument Selection Using a Web-based Virtual Experiment**", Computers in Education Journal, pp 81-91, Vol. 3, No. 3, July-September 2012.

- Malali, P., Bais, P., Chaturvedi, S., Chaote, E., (2010) "**Uncertainty Analysis and Instrument Selection Using a Web-based Virtual Experiment**", ASEE Annual Conference and Exposition, June 20-23, 2010, Louisville, Kentucky, USA.

- Malali, P., Luettel, C., Bharadwaj, A., Ram, A., Hegde, A., Prakash, K., (2008) "**Experimental Study of Small Scale DC Direct MHD Thrusters**", 39th AIAA Plasma Dynamics and Lasers Conference, June 23-26, 2008, Seattle, Washington, USA.

- Sharma C L, Praveen Malali, D (2006) "**Comprehensive Study of Draft tube Oscillations**", Dam Engineering, pp157-174, Vol. XVIII, Issue-3, November 2006.

- Praveen Malali, D (2006) "**MHD Submarine-Design and Construction**". Proceedings of Emerging Trends in Mechanical Engineering, ETIME-2006, Feb 10-11, Bangalore, India.

AWARDS & HONORS

- Nominated for the **Outstanding Graduate Teaching Assistant** (GTA) award from the Batten College of Engineering (BCET), Old Dominion University, Norfolk, USA.